

**FIRST OBSERVATION OF THE
GREISEN-ZATSEPIN-KUZMIN CUTOFF.**

BY GARETH HUGHES

A dissertation submitted to the
Graduate School—New Brunswick
Rutgers, The State University of New Jersey
in partial fulfillment of the requirements
for the degree of
Doctor of Philosophy
Graduate Program in Physics and Astronomy

Written under the direction of

Professor Gordon B. Thomson

and approved by

New Brunswick, New Jersey

May, 2009

ABSTRACT OF THE DISSERTATION

First Observation of the Greisen-Zatsepin-Kuzmin Cutoff.

by Gareth Hughes

Dissertation Director: Professor Gordon B. Thomson

The High Resolution Fly's Eye Detector has observed the Greisen-Zatsepin-Kuzmin cutoff at the level of 5σ . The flux of Ultra High Energy Cosmic Rays from $10^{17.2}\text{eV}$ to $10^{20.2}\text{eV}$ has been measured. From the features seen in the spectrum it is found to be consistent with extragalactic Cosmic Rays of a light composition (mostly protons). A detector simulation is used to calculate the aperture of the experiment. Data-Monte Carlo comparisons are shown as a check of the accuracy of the simulation. Systematic effects of the detector and analysis are described and the effect on energy scale are presented.

We have carried out a study of the cosmic ray shower development. The results are compared to Monte Carlo simulations and theoretical predictions. This is the first time data has been analyzed in this way at such high energies. Events are found to agree with the Gaisser-Hillas profile which is used as input to the Monte Carlo and to calculate the primary particle energy.

Finally the Telescope Array (TA) experiment is described and its proposed Low Energy Extension (TALE). The effect of using a faster FADC system on the geometrical reconstruction is investigated. The results from this study will be used in the design of TALE electronics.

Preface

Since their discovery in 1912 cosmic rays have been studied extensively. They cover many orders of magnitude in energy and thus may have several sources. At the highest energies cosmic rays are believed to be made up of two components, galactic and extra-galactic. The galactic cosmic rays are thought to be produced by supernova remnants. From $10^{17.0}\text{eV}$ to $10^{20.0}\text{eV}$ extra-galactic cosmic rays are dominant, their sources are yet to be identified. Cosmic ray flux falls approximately with E^{-3} and at Ultra High Energies is as low as 1 particle per km^2 per steradian per year. Such low fluxes require huge detector volumes and long experiment running times. Despite these challenges cosmic rays allow us to test particle physics over cosmological distances and at the highest energies.

In 1966 Grisen, Zatsepin and Kuzmin predicted that if the spectrum reached up to $10^{20.0}\text{eV}$ the particles would interact with the Cosmic Microwave Background. This would appear as a cutoff or end to the spectrum. HiRes is the first experiment to observe this spectral feature. Following the same argument another feature, the Ankle, is predicted to appear at $10^{18.5}\text{eV}$. HiRes along with several other experiments has observed this. If the cutoff had not been observed new physics would be required to explain why.

A new generation of cosmic ray detectors, with even larger volumes, have come online over recent years. With the expected increase in statistics it may be possible to look back along the arrival directions and discover the source. Also by reaching back down in energy it will be possible to measure the extra-galactic flux across its whole energy range in a consistent manner.

This thesis is organized into the following sections.

I will first describe the history of Cosmic Rays and the state of our current knowledge. Past experiments and their results for the Ultra High Energy Spectrum and composition are shown.

Chapter 2 contains a description of the HiRes experiment, including the layout, electronic, calibration and triggering.

The HiRes-II detector Monte Carlo simulation will be described in chapter 3. A program outline and the shower library are discussed as well as the simulation of the readout electronics and trigger.

A description of the event reconstruction analysis chain is outlined in the 4th chapter. It shows how the raw data is used to form the event geometry, profile and primary particle energy.

Following this in chapter 5, is a discription of the aperture and energy spectrum calculation. I will outline the unfolding method and quality cuts. Data Monte Carlo comparisons are shown to demonstrate our understanding of the instrument. The spectrum is then presented and compared to other experiments. A check of the aperture and spectrum features is then presented. Finally a fit to the spectrum identifies two breaks which are the Ankle and GZK Cutoff.

In Chapter 6 the systematics of the experiment are investigated. New and improved inputs to the analysis and how they effect the energy scale are described.

Chapter 7 gives a method for calculating an average longitudinal profile of a Cosmic Ray shower from the data and Monte Carlo. These average showers are compared to predicted shower shapes and parametrized as a function of energy.

Telescope Array (TA) and it's Low Energy Extension (TALE) experiments are introduced in chapter 8. An investigation of the proposed FADC electronics for TALE is presented and the results shown.

Acknowledgements

Firstly to my advisor Gordon for his support, guidance, knowledge and introducing me to the world of cosmic rays.

To my family for their love and encouragement.

To the HiRes/TA group at Rutgers. Many thanks to Doug for all his invaluable help with my work. To Andreas for taking me under his wing and getting me started. And to Lauren for his help, the laughs and all those lifts.

For the inspiration to look beyond the UK, I would like to thank Nichelle.

Ron, Shirely and Nancy for making Rutgers work.

To everyone at Utah. Including John Matthews, Charlie Jui and Pierre Sokolsky for their help and insight. To Stan and Jeremy for taking all those late night phone calls. And Tareq for analysis tips.

Many thanks to my committee for their support.

To the National Science Foundation for financially supporting this work.

Finally thanks to the Army and Staff of Dugway Proving Ground.

Dedication

for my brother, Glyn.

*In the beginning the Universe was created. This has made a lot of people very angry
and has been widely regarded as a bad move.*

Douglas Adams

Table of Contents

Abstract	ii
Preface	iii
Acknowledgements	v
Dedication	vi
List of Tables	xi
List of Figures	xii
1. Introduction	1
1.1. History of Cosmic Ray Research	1
1.2. Cosmic Rays Energy Spectrum	2
1.3. Ultra High Energy Cosmic Rays Experiments	2
1.4. Extensive Air Showers	7
1.5. Cosmic Ray Acceleration	10
1.6. Sources	12
1.7. Propagation of Cosmic Rays	14
1.8. Composition	16
1.9. Anisotropy	18
2. The HiRes Experiment	20
2.1. The High Resolution Fly’s Eye Detector	20
2.2. HiRes-II FADC Detector	25
2.3. Calibration	28

2.4. Atmospheric Monitoring	30
3. HiRes Monte Carlo Detector Simulation	34
3.1. Program Outline	34
3.2. Database	35
3.3. CORSIKA Shower library	35
3.4. Detector Response	36
3.5. Electronic Simulation	38
3.6. Triggering Changes	38
3.7. Simulation Output	39
4. Event Reconstuction	40
4.1. DST Data Structure	40
4.2. Shower Detector Plane	40
4.3. Event Geometry	42
4.4. Longitudinal Profile	43
4.5. Event Filtering	44
4.6. Inverse Monte Carlo	44
4.7. Energy Calculation	45
4.8. Missing Energy	46
5. Aperture and Energy Spectrum	48
5.1. Unfolding the Spectrum	48
5.2. Quality Cuts	49
5.3. Data Monte Carlo Comparisons	50
5.4. Aperture and Exposure	58
5.5. Spectrum	59
5.6. Constant Aperture Check	67

5.7. Fits to the Spectrum	67
6. Systematics of the HiRes-II Spectrum	72
6.1. Introduction	72
6.2. Atmospheric Database	72
6.3. Fluorescence Yield	73
6.4. YAG calibration	82
6.5. Radiosonde Database	82
6.6. Mirror Reflectivity	86
6.7. Shower Energy Loss	88
6.8. Input Spectrum and the G.Z.K. Cutoff	94
6.9. Total Systematic Shift	97
7. Average Longitudinal Shower Profile	101
7.1. Gaisser-Hillas Profile	101
7.2. Normalization of Air Shower Profiles	102
7.3. Experiment and Data Set	104
7.4. Average Showers	104
7.5. Data - Monte Carlo Comparisons	113
7.6. A Reality Check	113
7.7. Conclusion	115
8. Telescope Array	116
8.1. Introduction	116
8.2. Ground Array	116
8.3. Fluorescence Detectors	118
8.4. Telescope Array Low Energy Extension (TALE)	118
8.5. Physics of TA and TALE	119

8.6. Simulating the TALE Detector Electronics.	121
9. Conclusion	126
9.1. Average Profile	126
9.2. Telescope Array and the Low Energy Extension	126
9.3. HiRes, G.Z.K. Cutoff and Systematics	127
Bibliography	128
Curriculum Vita	134

List of Tables

1.1. Summary of UHECR experiments [1]	5
2.1. Channel assignment HiRes-II FADC.	26
2.2. HiRes-II Trigger Summary	28
5.1. On times for all Data Sets.	49
5.2. List of Quality Cuts.	50
5.3. Summary of Spectrum Fit Information.	70
5.4. Summary of HiRes-II Events and Spectrum	71
6.1. Nitrogen Fluorescence Yield Transitions and Wavelengths.	76
6.2. Normalized Spectra and Total FLY for ground level	81
6.3. Spectra after attenuation from Figure 6.6	81
6.4. CORSIKA Input card for this analysis	96
7.1. Cuts Used in this analysis.	105

List of Figures

1.1.	All Particle Cosmic Ray Energy Spectrum [2]	3
1.2.	Exposures of UHECR experiments as a function of energy, [3, 4, 5, 6].	4
1.3.	Cross Section of a Cosmic Ray Air Shower Simulation using CORSIKA, Electrons are shown in red, hadrons in blue, muons in green and neutrons in grey.	8
1.4.	Cartoon of Extended Air Shower, EAS	9
1.5.	Heitler model of cosmic ray air shower	9
1.6.	Diagram showing Fermi Acceleration model	11
1.7.	Hillas Plot of Prospective Cosmic Rays Sources. Proton and Iron lines for 10^{20} eV particles. Proton lines for β of 1 and $1/300$. $E_{max} \sim \beta$ ZeBL	13
1.8.	Elongation rate for HiRes Stereo detector and HiRes/MIA prototype	17
1.9.	HiRes Galactic sky map. Black dots: AGN. Green circle and triangle are the locations of Centaurus A and M87. Red circles: Correlated cosmic ray events and blue circles uncorrelated. Each event has a 3.1° circle.	19
2.1.	HiRes-II FADC Detector, Dugway Proving Ground, Utah.	20
2.2.	Cartoon showing experimental setup.	22
2.3.	Filter Transmission (black) and Photo-tube Quantum Efficiency (red).	23
2.4.	HiRes-II mirror arrangement. Mirrors 2 and 4 point toward HiRes-I.	24
2.5.	HiRes-II Mirror Building. Showing Ring 1 (right) and Ring 2 (left), cluster boxes and electronics rack.	25
2.6.	HiRes-II Electronics Layout.	27
2.7.	Comparison of Human Weather Codes and Infrared Sensor Data. Fraction of time Human Codes agree with Infrared Camera.	32

3.1. Number of Photo-electrons per degree for all events in data sets 1, 3 and 5. . . .	39
4.1. Standard Shower Geometry and Parameters.	41
4.2. Event Recorded on May 10 th 2002 Mirror View.	42
4.3. Time vs Angle Plot. Red tubes are “Good”. Black tubes are “Bad”. Line are fits described in text.	43
4.4. Reconstruction Chain for the May 10 th 2002 Event.	44
4.5. Photo-electron Flux as a function of Slant Depth.	45
4.6. Functional form of missing energy.	47
5.1. Track length of Showers seen in mirrors (degrees).	51
5.2. R_P (km), Closest distance of approach to detector.	52
5.3. ψ (degrees) as defined in figure 4.1.	52
5.4. Zenith angle of air shower with respect to the ground (degrees).	53
5.5. Number of mirrors in each event.	53
5.6. Mirror participation.	54
5.7. Number of photo-electrons per degree of shower track.	55
5.8. Number of good tubes per degree of shower track.	55
5.9. Depth of shower maximum, X_{max} (g/cm^{-2}).	56
5.10. Primary Energy of cosmic ray.	56
5.11. X_{max} Difference, Reconstructed - Thrown (g/cm^{-2}).	57
5.12. Energy Resolution of Primary Cosmic Ray.	57
5.13. HiRes-II Aperture.	58
5.14. HiRes-II Exposure	59
5.15. Cosmic Rays Spectra for HiRes-I and HiRes-II.	60
5.16. Cosmic Rays Spectra for HiRes-I, HiRes-II and AGASA.	61
5.17. Cosmic Rays Spectra for HiRes-II for data sets 1-3 and 1-5.	62
5.18. Cosmic Rays Spectra for HiRes-II and the HiRes Prototype-MIA experiment. . .	63

5.19. Cosmic Rays Spectra for HiRes-II and Fly's Eye Experiment.	64
5.20. Cosmic Rays Spectra for HiRes-I, II and Auger Ground Array.	65
5.21. Cosmic Rays Spectra for HiRes-I, II and Auger Hybrid Result.	66
5.22. Exposure for Datasets 1 to 5 with R_P cuts.	67
5.23. Primary Energy Distribution of Cosmic rays $\times Energy^2$	68
5.24. HiRes-I and II Spectrum with single γ fit.	69
5.25. HiRes-I and II Spectrum with 1 break point fit.	69
5.26. HiRes-I and II Spectrum with 2 break point fit.	70
6.1. Ratio of apertures with the Atmospherics database to the Standards HiRes-II aperture	73
6.2. Shift in Energy by applying Atmospheric Database.	74
6.3. Electronic bands of the Nitrogen Molecule [7].	75
6.4. Measurements of Fluorescence Yield as a function of energy as compared to $\frac{dE}{dX}$. Sold line is $\frac{dE}{dX}$ of air. Dashed line $\frac{dE}{dX}$ for a thin air target with no knock on electrons - as used in the experiments.	78
6.5. Normalized Fluorescence Yield Spectra	79
6.6. Wavelength dependent Transmission Factors.	80
6.7. Amount of light compared to Standard HiRes.	82
6.8. Shift in Energy by applying FLASH spectra	83
6.9. Shift in Energy by applying FLASH spectra and mirror wavelength dependence.	84
6.10. Shift in Energy by applying YAG database	85
6.11. Shift in X_{max} by applying Radiosonde Database.	86
6.12. Shift in Energy by applying Radiosonde Database.	87
6.13. Average reflectivity of the HiRes-II Mirrors	88
6.14. Wavelength dependence of a HiRes-II mirror	89
6.15. Shift in Energy by applying Mirror Database and Wavelength Dependence.	90

6.16. $\frac{dE}{dx}(s)$ for a given age, s. Points are calculated using f_e from Nerling et al. The line comes from Song et al.	92
6.17. Comparison of Nerling's α and Song et al.	93
6.18. α_{eff} <i>black</i> : Individual showers. <i>Red</i> : Average. <i>Blue</i> : Fit using Nerling parametrization	95
6.19. Shows the original shower(<i>red</i>) thrown with (300,700) and the calculated shower(<i>black</i>) using equation 6.15	97
6.20. Shift in Energy by applying Nerling $\frac{dE}{dX}$	98
6.21. Effect of adding cutoff to the Input Spectrum.	99
6.22. Shift in Energy by Applying All Effects.	100
7.1. Typical Air Shower as measured by HiRes-II. Fit to equation 7.1	102
7.2. Typical Normalized Air Shower as measured by HiRes-II. Fit to equation 7.4 - <i>solid line</i> and equation 7.5 - <i>Dashed line</i>	104
7.3. Comparison of the same Monte Carlo set analyzed using reconstructed and true values of ψ . Black reconstructed ψ and blue thrown ψ	106
7.4. Average Shower from the data in the energy range $10^{19.0}$ to $10^{19.5}$ eV. Blue marks are the original showers. Black marks the average. The line is a fit to equation 7.4. Lower panel shows the residuals.	107
7.5. Average Shower from the data in the energy range $10^{19.0}$ to $10^{19.5}$ eV. Blue marks are the original showers. Black marks the average. The line is a fit to equation 7.5. Lower panel shows the residuals.	108
7.6. Average Shower width as a function of energy. Red: Standard Monte Carlo, Blue: Pure Iron Monte Carlo and Green: Pure Proton Monte Carlo.	109
7.7. Average Shower width as a function of energy. Red: Standard Monte Carlo and Black: Data.	110
7.8. Average Shower width as a function of energy using the atmospheric database.	111

7.9. Average Shower width as a function of energy. Red: Standard Monte Carlo and Purple: Monte Carlo using reconstructed using thrown ψ	112
7.13. Average Shower width as a function. Black: Data, Green: Gaisser-Hillas shaped showers and Red: Gaussian shaped showers.	115
8.1. Map showing layout of Telescope Array.	117
8.2. Spectrum of Cosmic Rays $\times E^3$ as a function of Energy for the Experiments Shown. [8]	117
8.3. Elongation Rate, Mean X_{max} for the Experiments Shown and Pure Composition Simulations Proton and Iron for various Hadronic Interactions.	120
8.4. Cosmic Ray Flux for several experiments near $10^{17.5}\text{eV}$ [4]	120
8.5. ψ resolution (degrees) for the HiRes-II detector. Labels denote $\log_{10}(\text{Energy})$. .	121
8.6. Event display for one event using 25ns FADC integration time. See text for details.	123
8.7. ψ and R_P resolution for 100ns and 25ns FADC times.	124
8.8. Upper panels: Acceptance of events and ratio of 100ns acceptance to 25ns. Lower panels: Resolution of ψ and R_P as a function of energy. Red corresponds to 25ns. Black to 100ns.	125
8.9. A single FADC trace for various τ_s	125

Chapter 1

Introduction

1.1 History of Cosmic Ray Research

Cosmic rays are ionized nuclei arriving at the Earth's atmosphere at a rate of 1000 per square meter per second. Most are relativistic and some are ultra-relativistic. This work will be concerned with the most energetic of these particles with energies up to 10^{20} eV. At this energy a proton has 16 Joules of energy, equivalent to a well thrown baseball. Where they come from and how they are accelerated are the fundamental questions of cosmic ray research.

The name cosmic ray is an accident of their discovery. In 1912 Victor Hess [9] was studying radiation as a function of altitude using a hot air balloon. Using a gold leaf electroscope he found that the radiation increased the higher he went. Leading him to the idea of radiation coming from space. Hess received the 1936 Nobel prize for his discovery.

Cosmic rays were soon used in the study of particle physics, yielding the discovery of the muon and positron as well as some hyperons and mesons. Given the difficulties of these experiments in the 1950's particle physicists moved over to accelerators. However the Large Hadron Collider will operate at a center of mass energy 1000th of the interactions caused by Ultra High Energy Cosmic Rays (UHECR).

In 1936 Pierre Auger setup detectors in the Alps spaced by a few meters [10]. They showed coincidences of secondary particles from primary cosmic rays interacting in the atmosphere at large distances. Calculating he had reached energies of 10^{15} eV.

1.2 Cosmic Rays Energy Spectrum

Figure 1.1 [2] shows the full cosmic ray differential energy spectrum. The flux falls with an approximate E^{-3} over 32 orders of magnitude in flux and 10 orders of magnitude in energy. However the spectrum contains some of structure. At $10^{15.5}\text{eV}$ there is a break in the spectrum called the knee. (All the features are named after parts of a leg). The ankle, another break, this time a hardening of the spectrum, is found at $10^{18.6}\text{eV}$ and cutoff the cutoff is observed at $10^{19.8}\text{eV}$. There are also hints of a second knee at $10^{17.5}\text{eV}$. The ankle and cutoff are likely caused by interactions with the Cosmic Microwave Background and are discussed in section 1.7. At the knee experiments such as KASCADE-GRANDE have attempted to measure the mass composition of the primary cosmic rays [11]. The steepening of the spectrum is associated with an increase in the mass and has been interpreted as the end of the galactic component of the cosmic ray spectrum. If acceleration is proportional to the charge of the cosmic ray, heavier particles can be accelerated to higher energies for a given source, and thus may have higher fluxes at higher energies.

As the flux falls rapidly with energy the detection techniques used to measure the spectrum change for one energy range to another. Low energy cosmic rays can be detected directly by balloon based experiments. Above 10^{14}eV ground based techniques are required. These will be described in the following section.

1.3 Ultra High Energy Cosmic Rays Experiments

In the following section I will give a description of the previous and current UHECR experiments. The location and method of detection are described. These are important factors to consider when looking at their respective results. The location determines where on the sky the experiment can view and which potential sources they see. Ground arrays, comprised of scintillation or water tanks have the benefit of being able to run continually whilst air fluorescence technique can only be done on moonless nights, which is approximately 10% of the total.

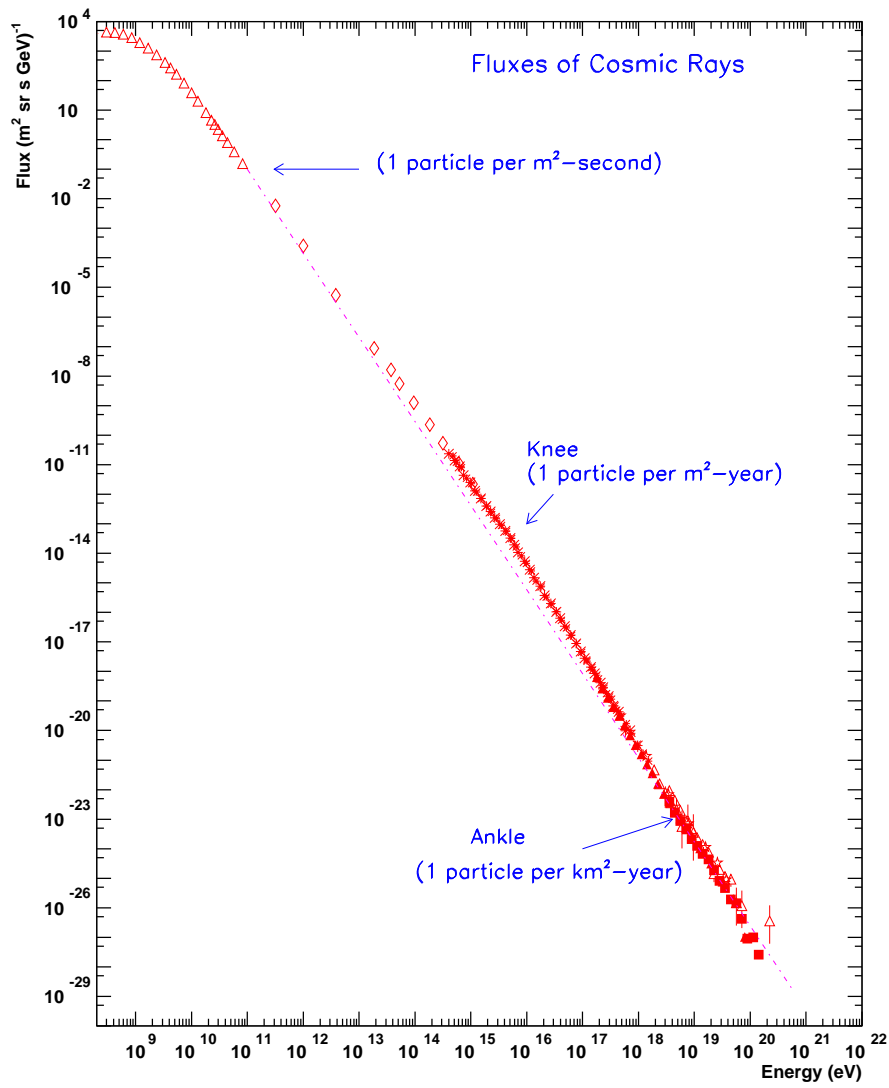


Figure 1.1: All Particle Cosmic Ray Energy Spectrum [2]

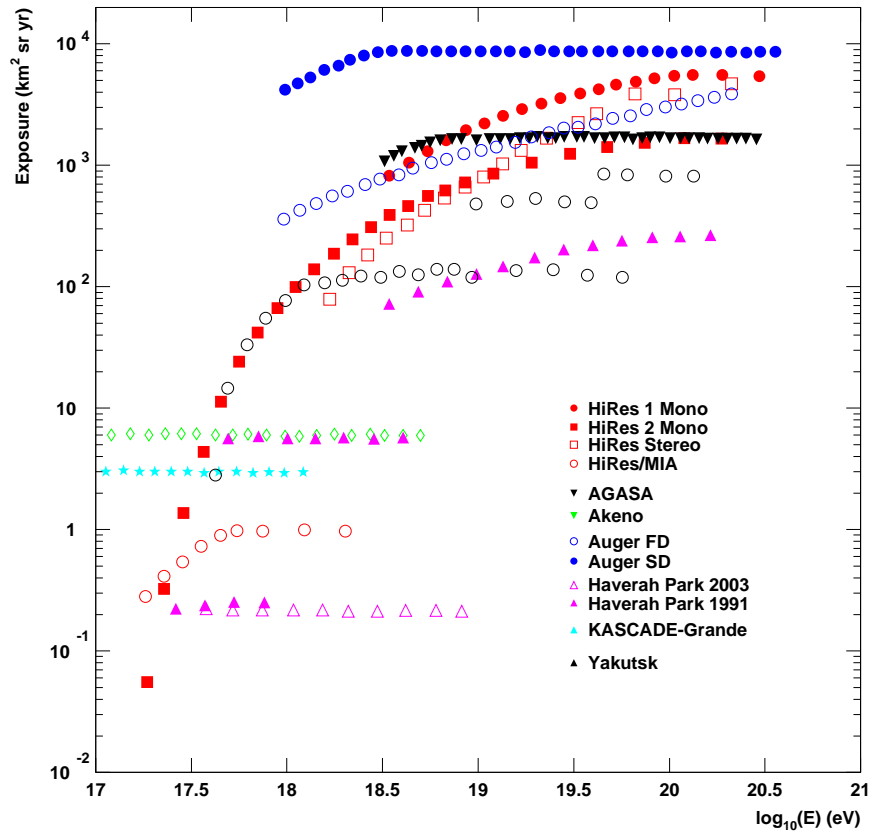


Figure 1.2: Exposures of UHECR experiments as a function of energy, [3, 4, 5, 6]

However air fluorescence detector see the development of the shower profile as it comes down through the atmosphere. Ground arrays are only able to sample to the shower at one level and rely heavily on simulation to extract an energy measurement

Figure 1.2 shows the exposures of a number of experiments as a function of energy [4]. Table 1.1 summaries some of the most important experiments and gives the number of events seen above 50EeV . Emphasizing how difficult it is to collect data at such low fluxes.

Experiment	Status	Exposure ($km^2.sr.yr$ @ 50EeV)	Events > 50EeV
Haverah Park	1962-1987	~ 245	10
Yakutsk	1974-present	~ 900	6
Fly's Eye	1986-1993	105	141
AGASA	1993-2005	1620	46
HiRes 1 Mono	1997-2006	~ 4500	31
HiRes 2 Mono	1999-2006	~ 1500	12
HiRes Stereo	1999-2006	~ 2400	11
Auger	2004-present	$\sim 7000(2007)$	38
TA	2007-present	860(2007)	-

Table 1.1: Summary of UHECR experiments [1]

1.3.1 Haverah Park

Haverah Park was the first experiment to use water Cerenkov tanks, [12]. It was located in the North West of England near Leeds University ($54^{\circ}N$ $1.6^{\circ}W$), operating from 1962 until 1987 at an atmospheric depth of $1016g/cm^2$. Each tank was 1.2m deep with an area of 2.29 meters and contained a 5 inch photomultiplier tube. The array consisted of clusters of tanks grouped at different spacings, enabling triggering on greater range of primary energy cosmic rays.

1.3.2 Fly's Eye

Fly's Eye was the first successful fluorescence detector, [13]. It was a stereo detector located on the Dugway Proving ground ($112^{\circ}50'9''W, 40^{\circ}11'43''N$) in Utah with the two sites separated by 3.3km. Fly's Eye I had full sky coverage, while Fly's Eye II only covered part of the sky for stereo observations. There were a total of 67 mirrors between the two sites. Each mirror had an area of $1.95m^2$ and a camera with 12 or 16 photo-tubes, with each covering $5^{\circ} \times 5^{\circ}$. Fly's Eye was sensitive to cosmic ray energies from $10^{17}eV$ to above $10^{19}eV$.

1.3.3 HiRes Prototype/MIA

HiRes/MIA was the first hybrid detector where both the fluorescence and ground array technique was used, [14]. It ran from 1993 to 1995 on Dugway Proving ground in Utah at an atmospheric depth of $860g/cm^2$. The Michigan Interred Array (MIA) array consists of 16 groups of 64

scintillators. Each scintillator was $1.9 \times 1.3 m^2$ and buried under 3m of earth. Burying the detector removes the electromagnetic component of the shower leaving it sensitive to only the muonic component. The HiRes prototype was comprised of 14 mirrors with a $16^\circ \times 14^\circ$ field of view. Each cluster box or camera was made up of 256 photo-tubes, each with a 1° viewing angle. Mirrors were arranged in a tower configuration had and $\sim 60^\circ$ opening azimuthal angle and seeing up to 70° in elevation.

1.3.4 Yakutsk

Yakutsk ground array has been in operation since 1970 until the present day and is located in Russia at $61.7^\circ N$ $129.4^\circ E$, [15]. It is a ground array experiment using scintillator counters, comprised of a graded array, where the detector spacing varies from 62m to 500m and 1km. There are also Cerenkov detectors and buried muon detectors.

1.3.5 SUGAR

SUGAR stands for the Sydney University Giant Air shower Recorder, [16], located in Australia at $30.5^\circ S$ $149.6^\circ E$ and operated from 1968 to 1979. They used buried liquid scintillators separated by 50m covering a mile square grid. Each scintillator had an effective area of $6 m^2$.

1.3.6 Akeno and AGASA

Akeno was a $1 km^2$ array located in Japan, $35.8^\circ N$ $138.5^\circ E$, [17]. 156 scintillator counters with $1 m^2$ and $2 m^2$ areas deployed at an atmospheric depth of $920 g/cm^2$. They had 120m and 30m spacings. It operated from 1970 to 1980.

The Akeno Giant Air Shower Array [18] consisted of 111 plastic scintillators each with an area of $2.2 m^2$ at a spacing of 1km. Located in Japan at a height of 900m above sea level and a latitude of $35^\circ N$ and $138^\circ E$. Operating from 1990 until 2004 it sampled the shower front as it reached the ground. An extra 27 counters were also deployed with shielding enabling them to measure the muonic component of the shower. Information from each counter was transmitted

to a central computer via fiber optic cable.

1.3.7 Pierre Auger Observatory

Auger is located in Argentina at a latitude of $35^{\circ}S$ and $70^{\circ}W$ at an altitude of 1600m above sea level, [19, 20]. This hybrid detector consists of 1400 water tanks (Surface Detector, SD) and 4 fluorescence detectors (FD). Water tanks are separated by 1.5km covering a total area of $3000km^2$ and detect the Cerenkov light generated by muons (and to a lesser extent by electrons and photons) as they transverse the detector. Each FD station has 6 spherical mirrors with an area of $12m^2$ and radius of curvature of 3.4m. Each mirror has a camera contained 440 photomultiplier tubes giving a $30^{\circ} \times 30^{\circ}$ field of view. Large UV filters are placed in the field of view of the telescope. The 4 stations are placed on the edge of the array looking inward. Data collection started in 2004 and the array was fully deployed in 2008.

1.4 Extensive Air Showers

An extensive air shower is created when a cosmic ray interacts with molecules in the atmosphere resulting in a number of secondary particles being created. This process continues until the particles fall below the thresholds for secondaries to be produced and the shower decays away. At any point in time the shower looks like a thin disc of particles in a plane orthogonal to the direction of shower propagation as shown in figure 1.3.

For a primary charged nucleus or proton there are 3 components to each shower, hadronic, muonic and electromagnetic. The hadronic core is created by the strong interactions of the primary and its hadronic descendants, it fuels the tow components. At each interaction roughly a third of the primary energy goes into the electromagnetic part due to neutral pions decaying into photons. Charged pions and kaons decay creating muons and neutrinos which are are lost as missing energy. By the time the shower reaches shower maximum 90% of the particles in the shower are electrons and positrons. Each photon from neutral pion decay acts as the primary is the primary for an electromagnetic sub-shower that grows by bremsstrahlung and

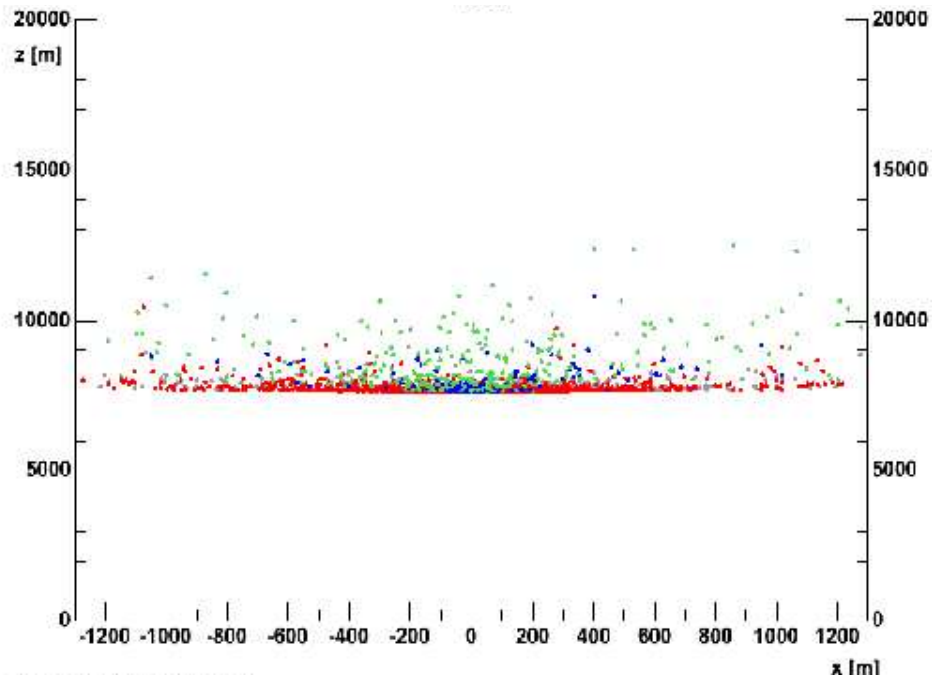


Figure 1.3: Cross Section of a Cosmic Ray Air Shower Simulation using CORSIKA, Electrons are shown in red, hadrons in blue, muons in green and neutrons in grey.

pair production until the energy falls below a critical level of 80MeV. At this point where ionization energy loss becomes more important than energy loss by radiation. Figure 1.4 shows a cartoon of this process.

A simple model of a shower that exhibits some of the most important features seen in more complex models is that of Heitler, see figure 1.5. Each particle interacts after a distance λ resulting in two daughter particles each with equal energy. At a depth X the number of particles is given by

$$N(X) = 2^{X/\lambda} \quad (1.1)$$

Each particle at a depth of X has an energy

$$E(X) = \frac{E_0}{N(X)} \quad (1.2)$$

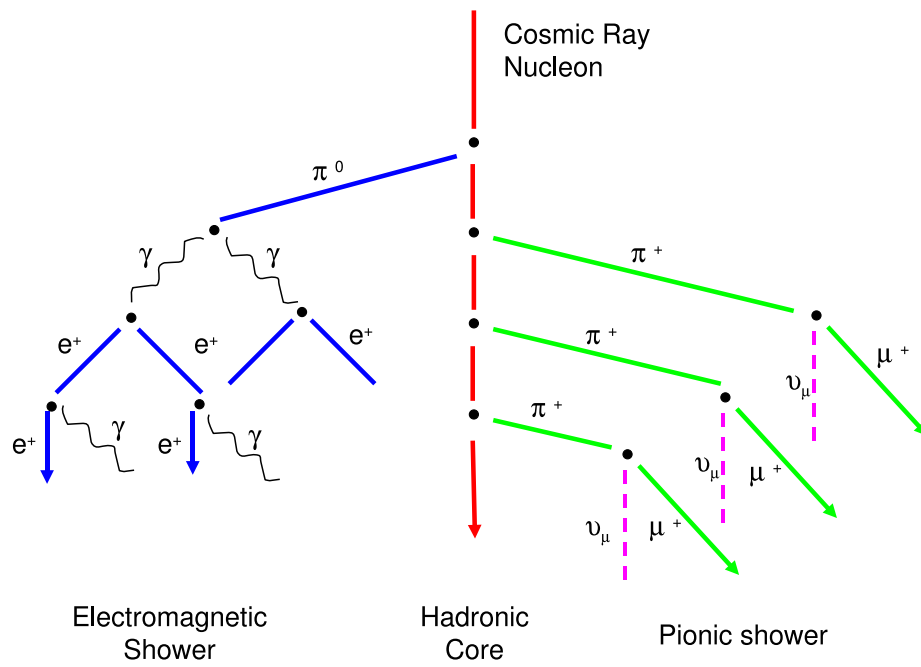


Figure 1.4: Cartoon of Extended Air Shower, EAS

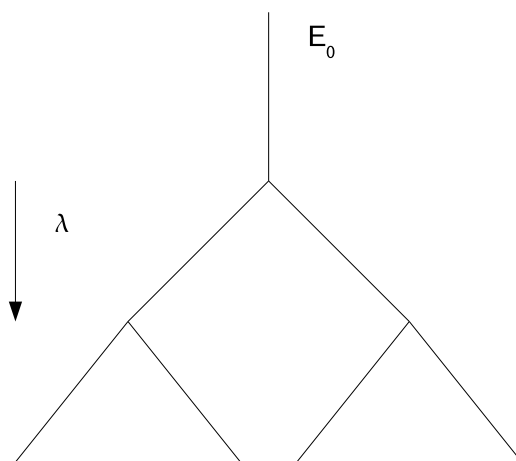


Figure 1.5: Heitler model of cosmic ray air shower

and the critical energy the shower reaches its maximum size defined by N_{max} occurring at the depth X_{max}

$$N_{max} = N(X_{max}) = \frac{E_0}{E_C} \propto E_0 \quad (1.3)$$

$$X_{max} = \lambda \frac{\log(E_0/E_C)}{\log 2} \propto \log(E_0) \quad (1.4)$$

In more complex models these relations still hold true. For hadronic induced showers it is found that

$$N_{max} = (1.1 - 1.6) \left[\frac{E_0}{GeV} \right] \quad (1.5)$$

If a cosmic ray has a mass A then it can be treated as A cosmic rays each having an energy E_0/A , this is called the principle of superposition. Therefore for the same primary energy X_{max} will be reduced by the $\log(A)$ for nuclei heavier than protons.

1.5 Cosmic Ray Acceleration

There are two types of acceleration models for cosmic rays. The first type of model is direct acceleration which used a strong magnetic field such as those surrounding a pulsar. These models are provide relatively fast acceleration but have problems with energy loss in dense regions and do not produce the observed power law spectrum. The second type of model is called Fermi Acceleration [21, 22], which does produce a power loss spectrum. A statistical, relatively slow acceleration, the particle gains energy as it crosses a shock front as shown in figure 1.6. The amount of energy gained by a particle is proportional to it's energy after n crossings the particle will have energy.

$$\Delta E = \epsilon E \quad (1.6)$$

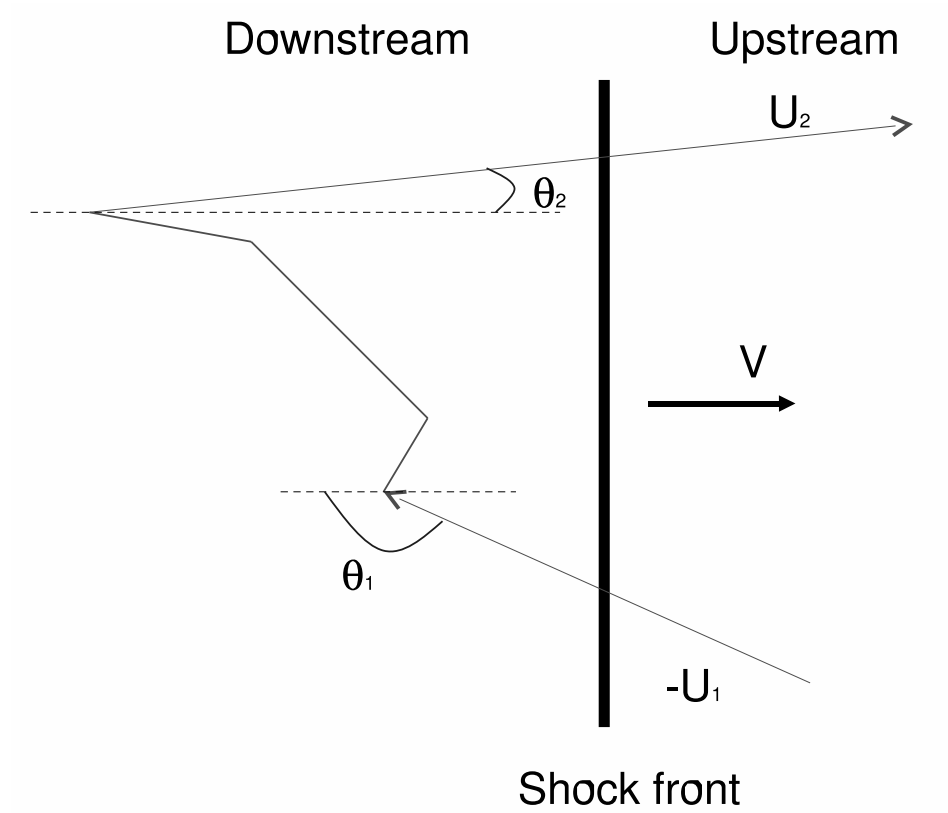


Figure 1.6: Diagram showing Fermi Acceleration model

$$E_n = E_0(1 + \epsilon)^n \quad (1.7)$$

Therefore n transitions are needed to reach an energy E from E_0 .

$$n = \ln\left(\frac{E}{E_0}\right) / \ln(1 + \epsilon) \quad (1.8)$$

If the probability of escape is at each crossing is P_{esc} then the probability a particle is still being accelerated after n crossings is $(1 - P_{esc})^n$ and the proportion of particles remaining are substituting equation 1.8 into 1.9 we find that

$$N(\geq E) = \sum_{m=n}^{\infty} (1 - P_{esc})^m = \frac{(1 - P_{esc})^n}{P_{esc}} \quad (1.9)$$

$$N(\geq E) \propto \frac{1}{P_{esc}} \left(\frac{E}{E_0} \right)^{-\gamma} \quad (1.10)$$

giving the observed power law energy spectrum where the index is given by γ

$$\gamma = \ln \left(\frac{1}{1 - P_{esc}} \right) / \ln(1 + \epsilon) \quad (1.11)$$

1.6 Sources

Figure 1.7 [23] shows candidate sources for UHECRs as a function of their size and average magnetic field strength. The area below the diagonal lines exclude sources from being able to accelerate protons (or iron - dashed line) above 10^{20} eV. These sites either require a large magnetic field or a huge acceleration volume. In smaller sites the process is statistical. As described in section 1.5 the particles gain energy slowly over many encounters with regions of moving magnetic fields. Large acceleration regions can act directly and therefore faster. Our Galaxy has a radius of 10kpc and a thickness of 100pc. It is a member of the local cluster which is 2Mpc in scale and the Virgo super cluster 30-50Mpc. The Virgo cluster center is 20Mpc away. The size of the Universe itself is defined to be the distance at which light would not reach us due to expansion. For $H_0 = 60 \text{ km s}^{-1} \text{ Mpc}^{-1}$ this is 5000Mpc. Figure 1.7 suggests that most galactic based sources are unable to accelerate protons or iron up to 10^{20} eV.

Other possible explanations are the so called Top Down Models [24]. In these models cosmic rays are the product of decays from large exotic particles, cosmic strings, magnetic monopoles or domain walls. These models would give no anisotropy in arrival direction but if they occur within the GZK radius we would not see the cutoff. For detailed description of sources see reference [25].

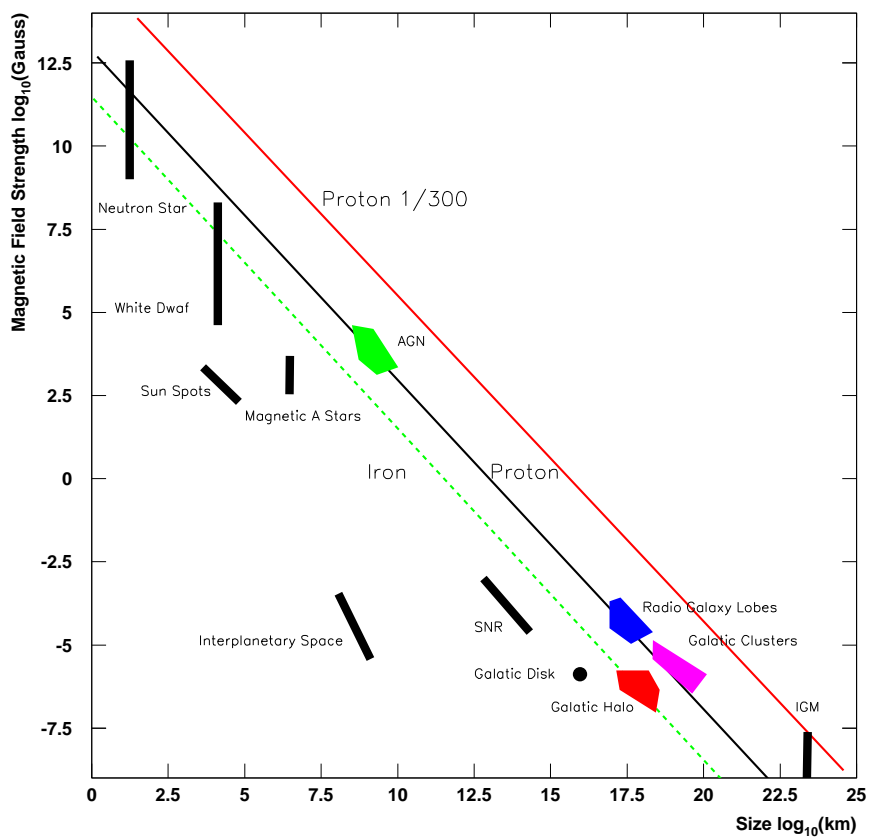


Figure 1.7: Hillas Plot of Prospective Cosmic Rays Sources. Proton and Iron lines for 10^{20} eV particles. Proton lines for β of 1 and 1/300. $E_{max} \sim \beta ZeBL$

1.7 Propagation of Cosmic Rays

The Larmor radius of a 10^{20}eV proton in a $3\mu\text{G}$ magnetic field is 30kpc which is on order of the galactic diameter. From this argument it is been believed that Ultra High Energy Cosmic Rays are extragalactic in origin. It therefore makes sense that the flux of cosmic rays at these energies should reflect their propagation.

The most dramatic of these effects was predicted in 1966 by Griesen [26] and independently by Zatsepin and Kuzmin [27]. The GZK cutoff is the end of the cosmic ray spectrum and is due to interaction with the Cosmic Microwave Background(CMB). This isotropic electromagnetic radiation follows a black body spectrum at a temperature of 2.725K . If a proton of sufficient energy meets one of these photons it can undergo pion production through the Δ^+ resonance.

$$p + \gamma_{CMB} \rightarrow \Delta^+ \rightarrow N + \pi^{0,+} \quad (1.12)$$

The final state N, can either be a proton or a neutron with a proton being twice as likely to be produced. For the above interaction to happen the center of mass energy must be greater than sum of the proton mass, m_p and pion mass, m_π .

$$s = m_p^2 + 2E_p\epsilon(1 - \cos\theta) \quad (1.13)$$

where ϵ is the photon energy ($6.3 \times 10^{-4}\text{eV}$) and θ the angle between the proton and photon. Therefore the minimum proton energy required to create a pion is

$$E_p = \frac{m_\pi}{4\epsilon}(2m_p + m_\pi) \simeq 10^{20}\text{eV} \quad (1.14)$$

When the full spectrum of the CMB photon energies are taken into account the threshold is found to be $3 \times 10^{19}\text{eV}$. The cross section of the $\Delta^+(1232\text{MeV})$ resonance is well known from accelerators to be $500\mu\text{b}$ at the threshold energy. Given that the density of CMB photons is

400cm^{-3} , the interaction length is calculated to be 8.3Mpc. On average the proton loses a fifth of its energy in each interaction.

There is an overall energy loss due the expansion of the universe. Which is simply the ratio of c/H_0 giving 4000Mpc for $H_0 = 75\text{kms}^{-1}\text{Mpc}^{-1}$.

The final source of energy loss is e^+e^- production with the CMB. Due to the electron mass the threshold energy for pair-production is much smaller ($2 \times 10^{19}\text{eV}$). The energy lost due to the interaction is on the order m_e/m_p .

$$p + \gamma_{CMB} \rightarrow p + e^+ + e^- \quad (1.15)$$

When considering more heavy nuclei we also have to take into account spallation where a photon removes a nucleon from the nucleus. The photo-production cross section is proportional to the square of charge, Z, while the threshold increases by a factor of $\log(A)$.

On their journey to Earth cosmic rays will be scattered by magnetic fields. In a constant magnetic field of 1nG a cosmic ray of energy 10^{20}eV has a gyro radius of 100Mpc. In a random field with correlation length l the deviation after propagating a distance D(100Mpc) in a nG magnetic field is

$$\langle \theta \rangle = 2.5^0 \left[\frac{B}{nG} \right] \left[\frac{D}{100Mpc} \right]^{0.5} \left[\frac{l}{Mpc} \right]^{0.5} \left[\frac{E}{10^{20}\text{eV}} \right]^{-1} \quad (1.16)$$

Another interesting effect of magnetic fields is a time delay of arrival at the Earth from the source compared to light. For small angle scattering the following can be shown.

$$\delta\tau = 3 \times 10^5 \left[\frac{B}{nG} \right]^2 \left[\frac{D}{100Mpc} \right]^2 \left[\frac{l}{Mpc} \right] \left[\frac{E}{10^{20}\text{eV}} \right]^{-2} \text{ years} \quad (1.17)$$

For example protons of energy $5.5 \times 10^{17}\text{eV}$ accelerated 100Mpc away would not reach the Earth in a 1nG random magnetic field, the $\delta\tau$ in this case is on the order of the age of Universe.

1.8 Composition

After decades of research it was determined that cosmic rays were extraterrestrial in origin and positively charged. At lower energies where direct detection is possible the composition is measured directly. Relative abundances of the various isotopes can be resolved and show that cosmic rays in the energy range 10^9 to 10^{14} eV are extra solar in origin.

Around the knee, 10^{15} eV, where direct detection is not possible, experiments such as KASCADE [11] measure the footprint of EAS on the ground. KASCADE used scintillation detectors some shielded from electrons by lead, so that they detect only the muonic component. The ratio of muon to electron density at a given radii from the shower core can be used to determine the mass of the primary cosmic ray. Results from KASCADE and KASCADE GRANDE suggest that the composition is lighter below the break in the spectrum at the knee and heavier above. These results are however very model dependent.

At the UHECR energy scale, measurement becomes even more difficult as the flux has now dropped to 1 particle per km^2 per century at 10^{20} eV. Future experiments such as TALE hope to measure the muon-electron ratio at these energies. Previous composition studies using fluorescence detectors use the depth of shower maximum, X_{max} . From equation 1.4 we see cosmic rays of the same energy but different mass have a different X_{max} . The elongation rate is defined as

$$\alpha = \frac{d \langle X_{max} \rangle}{d \log(E_0)} \quad (1.18)$$

In figure 1.8 the results of simulations are shown next to the HiRes Stereo composition result. The simulations are of purely proton and iron initiated showers for 2 different hadronic interaction models, QGSJET [28] and SIBYLL [29]. We see the data looks more proton like and has a constant composition above 10^{18} eV.

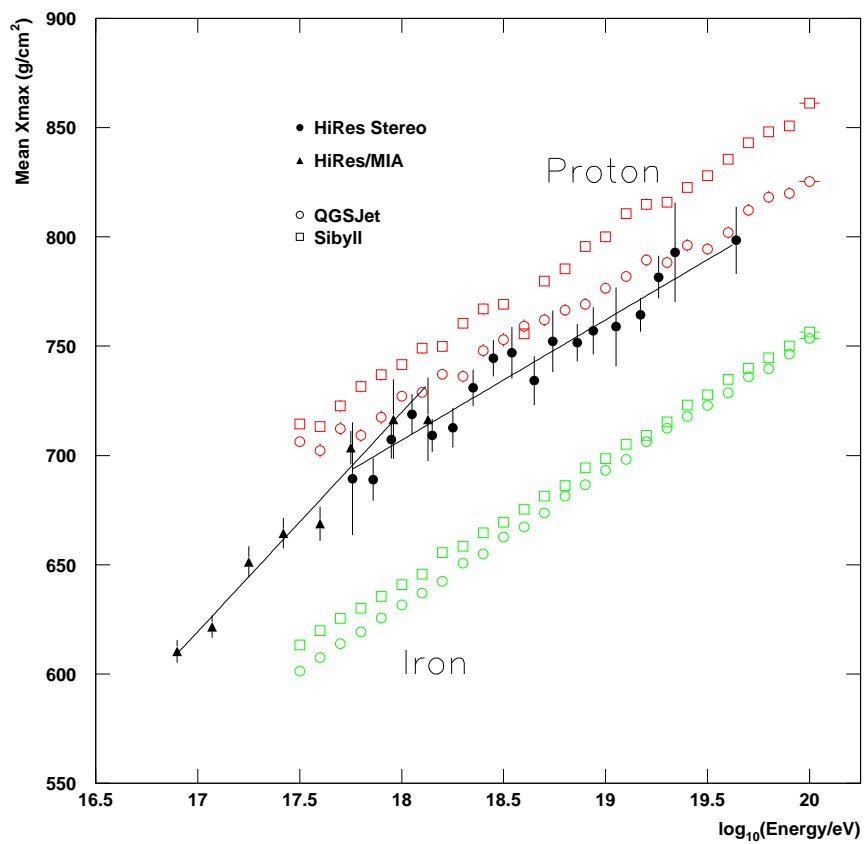


Figure 1.8: Elongation rate for HiRes Stereo detector and HiRes/MIA prototype

1.9 Anisotropy

The most obvious method to determine the origin of cosmic rays is to simply look back along their arrival direction. However as they are charged particles, magnetic fields are able to erode this information. This is of course not true for high energy gamma rays. Several excellent experiments have been taking measurements of galactic and extragalactic gamma ray sources for many years see [30, 31]

Around 10^{18} eV there have been several suggestions of a shortage of events in the direction of the galactic anti-center, including the HiRes-II experiment analysis by Gordon Thomson and Dimtri Ivanov, [32]. The data was used to calculate the isotropic background that correctly models the exposure of the detector. Comparing this to the data they found deficit of 3.2σ near the galactic anti-center.

Above 10^{19} eV the energies are high enough that the pointing direction does contain information. In 2007 Auger reported a 3σ correlation with Active Galactic Nuclei (AGN), [33]. The HiRes experiment using a similar analysis technique found our data did not agree with this conclusion. The data was also analyzed using several other methods and the most significant chance probability was found to be 24%, [34]. Care was taken to avoid statistical penalties in scanning. The variables scanned across were the minimum energy of cosmic rays, opening angle around the pointing direction and redshift of the candidate sources, $(E_{min}, \theta, Z_{max})$. By simply applying the parameters of the Auger experiment a chance probability can be found with incurring a penalty. Another method involves splitting the data into two equal parts, scanning across the first set to give the largest number of correlations and then applying those parameters to the second half a significant can be found. However this method reduces the statistical power available. A procedure that avoids this is the Finely-Westerhoff method. Scanning over the same parameter this time using the whole data set, the chance probability is then calculated by finding the number of simulated data sets that have at least the same number of correlations as the data. The exposures of the Auger and HiRes were approximately the same at the time of analysis. The only major difference that HiRes is in the Northern hemisphere and Auger in the

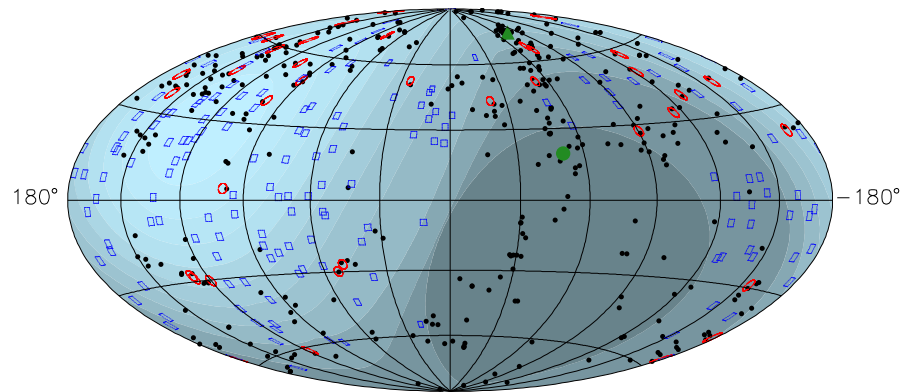


Figure 1.9: HiRes Galactic sky map. Black dots: AGN. Green circle and triangle are the locations of Centaurus A and M87. Red circles: Correlated cosmic ray events and blue circles uncorrelated. Each event has a 3.1° circle.

Southern. Studies are currently underway to see if the data agrees in general with large scale structure.

Chapter 2

The HiRes Experiment



Figure 2.1: HiRes-II FADC Detector, Dugway Proving Ground, Utah.

2.1 The High Resolution Fly's Eye Detector

The High Resolution Fly's Eye consisted of two air fluorescence detectors (HiRes-I and HiRes-II) located on Dugway Proving Ground, Utah, separated by 12.6km, HiRes-I sits on Five Mile Hill at $(112^{\circ}50'9''W, 40^{\circ}11'43''N)$ and HiRes-II occupies Camels Back Ridge $(112^{\circ}57'32''W, 40^{\circ}7'55''N)$. Both are at an atmospheric depth of $860g/cm^2$. HiRes-I incorporates 21 mirrors in a single ring

covering 3° to 17° in elevation. HiRes-II has 2 rings with 42 mirrors giving a 3° to 31° view in elevation. Both have a 360° azimuthal field of view. Each mirror had an area of $5.08m^2$ with an effective area of $3.92m^2$ and a camera placed at approximately the focal plane. The camera is made up of 256 hexagonally packed photomultiplier tubes (PMTs) in a 16×16 array, each tube covering $\sim 1^\circ$ of the sky. A UV pass filter in the range 300nm to 400nm covers the face of the camera. Figure 2.2 shows a diagram of the setup for one of the mirrors. The transmission for the HiRes filter and quantum efficiency for the photomultiplier tubes can be seen in figure 2.3. HiRes-II mirror arrangement can be seen in figure 2.4 . At each site a pair of mirrors, cameras and electronics racks are housed in a protective building with automatic garage doors, as seen in figure 2.5.

Both detectors were operated on clear nights and only when the moon is below the horizon for more than 3 hours. This is to reduce background light that would make it impossible to see showers. HiRes-I could be run remotely from either Utah, Columbia or Rutgers University. HiRes-II was run by at least 2 runners on site enabling repairs to take place at either location.

Every mirror had it's own set of high and low voltage supplies. Each PMT had a diagnostic pulse programmable generator and pre-amp. Timing information was provided by a GPS unit at each site. The timing resolution between sites was determined to be 50ns. HiRes-I mirrors communicated with the central DAQ computer via Ethernet cable and HiRes-II used a fiber optic ring.

2.1.1 The HiRes-I Detector

At each site there is a central control building containing the data acquisition computer (DAQ - 386 PC running Linux), GPS receiver and communication equipment. Each electronics rack is connect to the computer via Ethernet cable.

The HiRes-I electronic racks contains a VERSAmodule Eurocard (VME) crate, low and high voltage supplies, high voltage distribution (zener) boards and cooling fans. The high voltage supply is typically 1000V and is distributed to the tubes via the zener board. These boards are

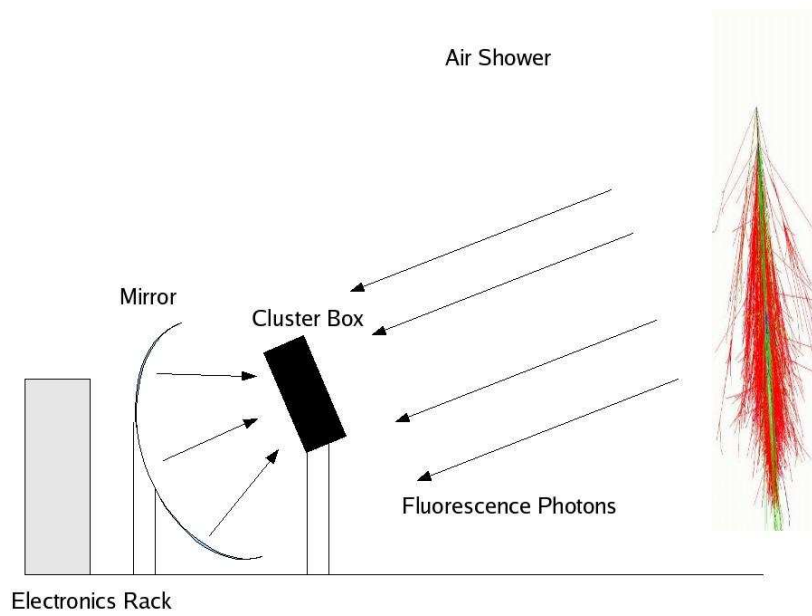


Figure 2.2: Cartoon showing experimental setup.

set (pegged) in order to gain match the individual tubes. Two low voltage supplies provide -12, +12 and +5V. The VME crate contains a CPU board, pulse programmable generator board (PPG), 16 ommatidial boards (OMB) and a “garbage” board. The CPU is responsible for communication with the DAQ computer while the garbage board controls garage doors and temperature sensors. The PPG generates a low voltage calibration signal to test each tube. Each OMB board is responsible for a sub-cluster of 16 tubes (4×4) receiving the amplified signal from each tube. If the tube is above threshold it is triggered and the signal shaped using two separate time constants, giving the ability to trigger in two different modes. Channels A and B had a $1.2\mu\text{s}$ and $5.6\mu\text{s}$ integration period, respectively. Tube thresholds are dynamically set in order to obtain a constant 200Hz individual tube trigger rate. A time offset ensures none of the event information is lost and then the signal is then digitized. A sub-cluster is triggered when three or more tubes are above threshold, two of which must be adjacent. The mirror triggers when 3 or more sub-clusters are triggered, once more two of which have to be adjacent.

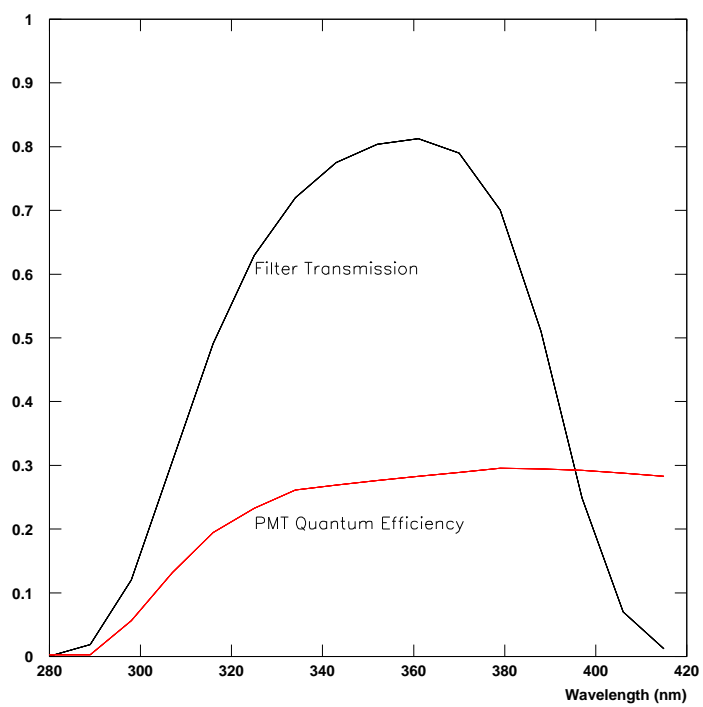


Figure 2.3: Filter Transmission (black) and Photo-tube Quantum Efficiency (red).

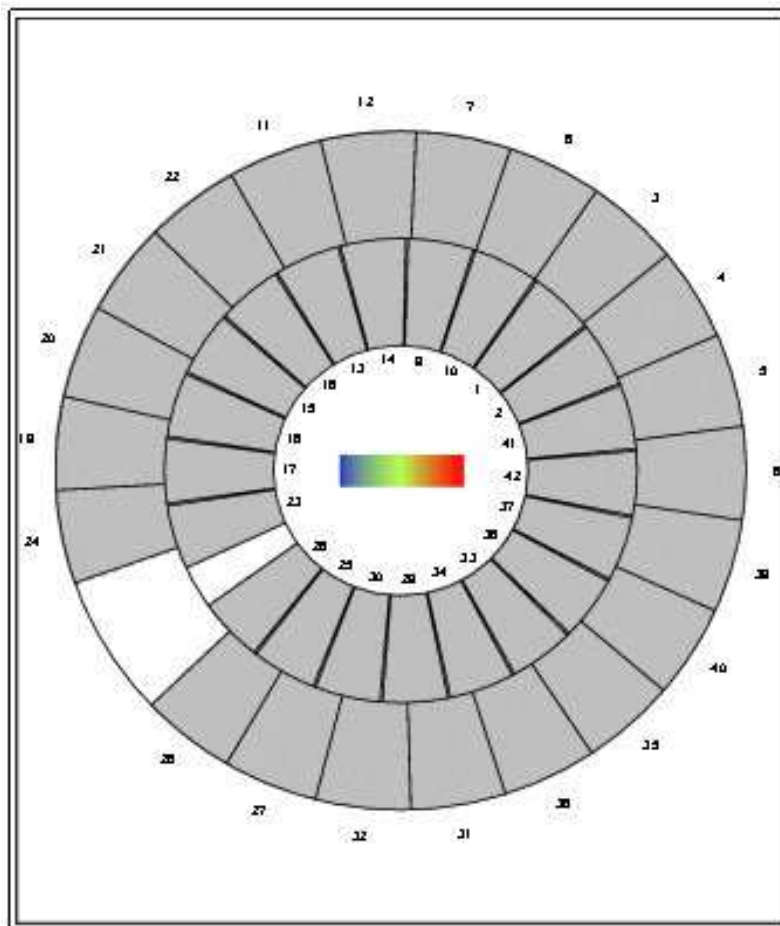


Figure 2.4: HiRes-II mirror arrangement. Mirrors 2 and 4 point toward HiRes-I.



Figure 2.5: HiRes-II Mirror Building. Showing Ring 1 (right) and Ring 2 (left), cluster boxes and electronics rack.

After a trigger the mirror holds off for $25\mu\text{s}$ (stops taking data). For this reason this type of system is called “sample and hold”. A 8ms period of dead time follows the event as the mirrors electronic thresholds are reset.

2.2 HiRes-II FADC Detector

The HiRes-II central control building contained a VME CPU crate responsible for communications and data storage, two GPS signal receivers and a communication VLink model. The final component controls 2 fiber optic rings which talked to the mirror crates and transmitted a 10MHz clock pulse.

Each mirror building had an electronics rack along with two mirrors and cameras, see figure 2.5. The rack housed two low voltage and one high voltage power supplies, two Fast Analog to Digital Converter (FADC) racks, a PPG board and a communication board.

The FADCs are responsible for digitizing the signals from the PMTs and triggering the mirror. Reference [35] gives a full description of the system. Table 2.1 shows the 320 channel assignments. The output is an 8 bit 100ns signal where 1 FADC count was calibrated via a

Channels	
1-256	High Gain for PMTs
257-272	Column 1-16 Trigger
273-288	Column 1-16 Low Gain
289-304	Row 1-16 Trigger
305-320	Row 1-16 Low Gain

Table 2.1: Channel assignment HiRes-II FADC.

Roving Xenon Flasher (RXF) to be 1 photo electron, [36, 37]. A Digital Signal Processor (DSP) was responsible for scanning the PMT column and row sums, which was the sum of the 16 tubes in each column or row. Both were scanned with low and high gains to increase the dynamic range. The DSP scanned the high gain channels too, to read out the active tubes.

In its 6 years of operation the HiRes-II trigger underwent many changes. There are 6 distinct trigger versions. The trigger is split into two distinct parts, primary and secondary. Both of which were realized in hardware. From trigger version 2 onward an adjacent mirror trigger was enabled, forcing the mirrors adjacent to the primary to be automatically read out. This had the benefit of giving longer tracks and a more accurate reconstruction. As the tails of some events are not bright enough to trigger a mirror on their own, information can still be retrieved from that part of the event.

The primary trigger is based on the row and column sums seen in table 2.1. If there are 2 or more threefold coincidences in the rows or column sums during a $5\mu\text{s}$ window a primary trigger is generated. All the channels are AC-coupled so that the pedestal is kept at a constant value. For the trigger channels this is 20 counts requiring 32 counts. Were required a primary trigger. In a 100ns time period the average sky noise is 6 photo-electrons per photo-tube. This corresponds to a variance of $\sqrt{6}$ counts in each FADC bin. Therefore 32 counts corresponds to almost 5σ .

The secondary trigger was implemented in order to remove “in-time” events. These are sometimes called Cerenkov blasts, where the shower axis comes very close to the detector beaming Cerenkov light causing many tubes to trigger at the same time. If the number of

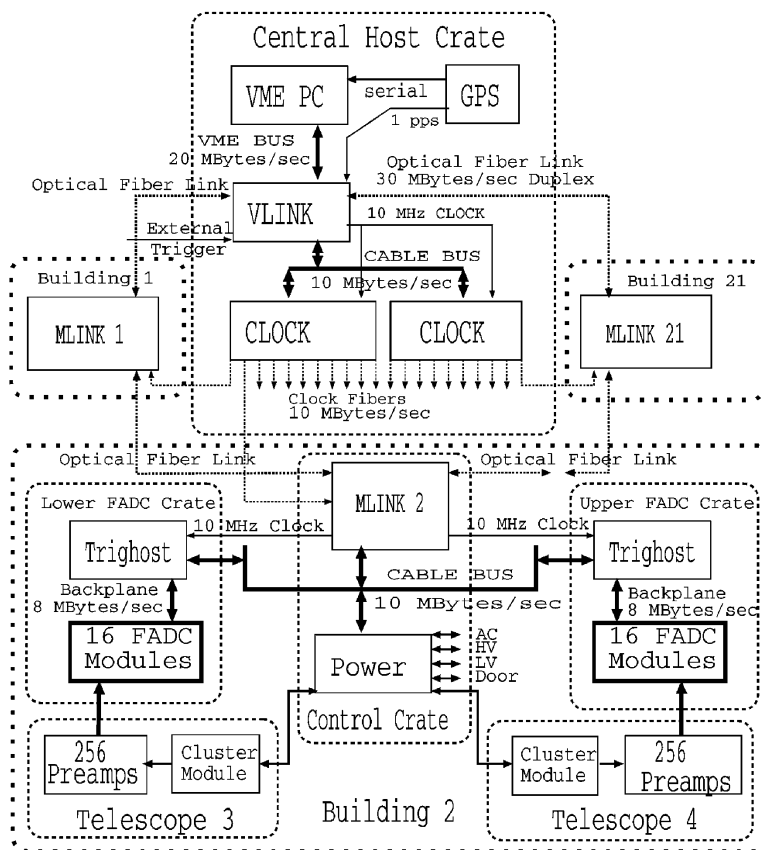


Figure 2.6: HiRes-II Electronics Layout.

Version	Date Operational	Description
1	4 Jan 2000	$n_{hit} > 5$
2	31 Aug 2000	$n_{hit} > 4$ in any 6x6 square of tubes
3	11 Sept 2001	$n_{hit} > 3$ in a cluster. no small equal time clusters allowed.
4	27 May 2003	$n_{hit} > 3$ in a cluster. no equal time clusters allowed of any size.
5	31 Jan 2004	confirm thresholds lowered, but servo'd according to average trigger DAC in mirror
6	06 April 2006	$n_{hit} > 2$ in a cluster, confirm thresholds midway between 5 and ver 4 and servo'd according to individual channel variance. Readout threshold also a bit lower and servo'd as above.

Table 2.2: HiRes-II Trigger Summary

sub-clusters hit is less than n_{hit} (see table 2.2) the variance in tube times must be large enough to exclude this type of event. See table 2.2 which summarizes the trigger changes.

2.3 Calibration

Calibration enables us to take the number of FADC counts or QDC value back to the number of photons incident on the mirror. This requires knowledge of the mirror reflectivity and filter transmission. Knowledge of the positional Quantum Efficiency (QE) and gain of the PMTs is also required.

Each tube was tested before being deployed. It was mounted on a translation table and illuminated along with a NIST calibrated photo-tube. This was done using a He-Cd laser on each photo-tube through a standard HiRes filter. Each tube face was scanned at 7 points across it's face. Another diode was also used to measure a small fraction of the beam split off in order to monitor it's intensity. The QE was found to not vary much from tube to tube and to be consistent with the manufacturers specifications.

2.3.1 Roving Xenon Flasher

The Roving Xenon Flasher (RXF) was used to calibrate the relative PMT sensitivity [36, 37]. The RXF is a Xenon flash bulb mounted in a portable housing attached to a Teflon diffuser. Placed in the center of the mirror in order to illuminate the cluster directly, it emits light in the 300-400nm range. Measurements have found it to be stable within 1-3% flash-to-flash and within 2% over the night. 12,000 photons per tube per flash are produced at the HiRes photo-tubes given the position of the flasher. The same RXF is used every time in order to consistently calibrate the mirrors relative to one another. Therefore the calibration is time consuming and only performed at the beginning and end of each run period.

2.3.2 NdYAG Calibration LASER

A fiber optic calibration system was designed to perform a relative calibration of the HiRes-II detector over its 6 year lifetime, enabling us to monitor changes in PMT gain, electronics response and reflectivity of each mirror. The system delivered light from a frequency tripled 355nm YAG laser to each of the 10,752 photo-tubes. It included several stability features, for instance, there was a single light source located in a clean, temperature controlled room. The relative intensity of each light pulse was measured and recorded by a system in the same location. The source wavelength lies within the 300-400nm band, corresponding to the N_2 scintillation. Calibration readings were taken nightly. For a full description see [38, 39].

Each of the 42 mirrors had 4 fiber cables, two "mirror cables" and two "cluster cables". The later pair shine light onto the mirror that is then reflected back onto the PMTs. A Teflon diffuser is used at the end of each fiber to create a diffuse source. The light source generates an 8mJ pulses with a 6ns duration with a final wavelength of 355nm. The most efficient N_2 scintillation line is at 337nm. A splitter takes 1% of the beam which is delivered two photo-diode probes monitoring the amount of light at the detector. The variations in the signal are used to normalize the measured signal in the detector. Laser output was found to vary with an RMS of 5% shot to shot. Average measurements compared with a lab-based piezo-electric

probe using 65,000 shots (comparable with several weeks of operation) found it to be stable to the 1% level. Differences in the amount of light delivered between detectors are within 10%. Relative shot-to-shot variation in the amount of light delivered to the monitor is better than 1%.

Two important parts of this work involve this calibration technique. First, the database resulting from the YAG readings was added to the analysis chain. This is described in section 6.4. Second, mirror reflectivity database was also calculated from this information by Professor Thomson and applied to the data as seen section 6.6.

2.4 Atmospheric Monitoring

In air fluorescence experiments the atmosphere is our calorimeter and also the medium through which we look. A detailed knowledge of the atmospheric conditions is required to calculate the number of photons at the shower from the number incident on the camera. Light is scattered not only by the molecular part of the atmosphere but also by aerosols. The molecular atmospheric scattering is well understood and we use the U.S. Standard atmosphere of 1976 [40]. Several tools were used during the lifetime of the experiment to characterize other aspects of the atmosphere [41]. These include operator observations, a 180° cloud camera, infrared sky temperature measurements, xenon flashers and a set of steerable YAG lasers. Thanks to these methods it is possible to know the condition of the atmosphere on an hourly basis for the most of entire operational lifetime of the experiment.

2.4.1 Operator Observations

To characterize the weather during operation, a system of weather codes were developed. Operators would identify clouds and haze (a sign of aerosols) by looking for stars and viewing distant man made light sources. The codes would then be entered into the logs and data stream at least once every hour. Although subject to human error and inconsistencies between operators these codes have proved invaluable in the analysis of data. The data was split into good and

bad weather nights and parts. A consistent method of allowing or removing data using these codes was applied to the whole data taking period.

2.4.2 Infrared Cameras

On each cluster at HiRes-I an infrared camera was mounted. With a field of view of $30^0 \times 30^0$ they measured the instantaneous sky temperature. As clouds appear hotter than the background sky. Using these cameras a 360^0 picture of the aperture can be built for every hour of operation.

Yulia Fedrova used the information collected to characterize the running conditions throughout the lifetime of the experiment. I compared this to the weather cuts used by looking at the human operators codes. Figure 2.7 shows that when the weathers code suggested it was a good weather night we agreed with the infrared 80% of the time. When the weather code suggested it was bad weather we agreed 60% of the time. This implies that the human weather codess were conservative.

2.4.3 Cloud Camera

At HiRes-I there was a 2π steradian infrared camera that scanned the sky every 15 minutes. This enabled the remote runners to assess the level of cloud cover whilst running the experiment. HiRes-II was always run by operators at the site and therefor had no need for such a device. They could also inform the remote site operators of sudden changes in weather.

2.4.4 Xenon Flashers

Ten Xenon flashers were placed between HiRes-I and II. They fired at preset intervals on the command of radio signals sent from HiRes-II. The time of firing was set to be a certain fraction of a second from the GPS signal enabling them to be removed from data easily. Several flashers were visible from both sites. This gives us the ability to do consistency checks with atmospheric information and the GPS timing at both detectors.

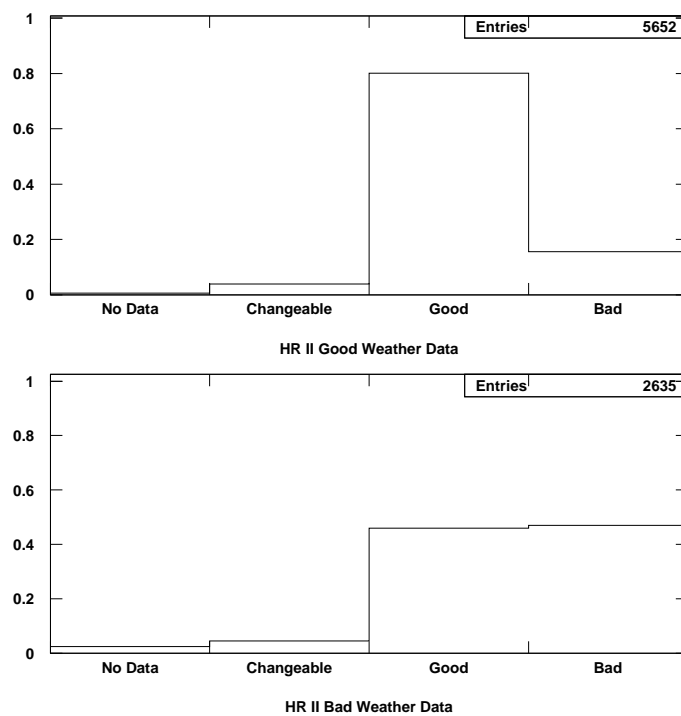


Figure 2.7: Comparison of Human Weather Codes and Infrared Sensor Data. Fraction of time Human Codes agree with Infrared Camera.

2.4.5 Steerable YAG Lasers

A set of steerable lasers, one each at HiRes-I and II, fire in a pattern of preset directions sweeping the experimental volume throughout the night. The shots from the laser at one site can then be studied by the other site. Andreas Zech used the relative intensities from the forward and back scattered light to determine the amount of aerosols in the atmosphere on a hourly basis, [38]. Another database was also calculated by the group at NEVIS. Section 6.2 shows the result of applying this database to the data and Monte Carlo compared to average conditions.

Chapter 3

HiRes Monte Carlo Detector Simulation

The HiRes-II monocular Monte Carlo program is used to accurately simulate the detector in order to calculate an aperture. It was initially developed by Andreas Zech [42] from a version of the NEVIS HiRes Stereo Monte Carlo. The program is called **Monte Carlo Rutgers University** (MCRU).

3.1 Program Outline

One event is simulated at a time. A read-in card file sets up the type of events we want to simulate for given energy and geometrical ranges.

3.1.1 Initial Inputs

Taking the ranges allowed by the read-in card file the Monte Carlo randomly chooses a geometry for the event. Choosing a random zenith angle and arrival direction all the other geometrical parameters are calculated. The standard set is thrown in the range 0.05km to 35km. The zenith angle is allowed to vary from 0° to 70° . An energy- R_p cut was implemented by Andreas Zech to save computer time when generating. Events at low energies and large distances, for example $10^{17.0}$ eV and 10km, will not be followed all the way through program. It is a loose but very effective cut.

There are many options for throwing energy in MCRU, including mono-energetic events and various input spectra. For the most accurate aperture possible the Monte Carlo uses a combination the Fly's Eye stereo and initial Hires Stereo spectra. For the standard Monte

Carlo set the low energy limit is set to $10^{16.5}\text{eV}$. In order to get better statistics at higher energies a second set is run with a lower energy limit of $10^{18.5}\text{eV}$.

MCRU can either throw proton or iron primary cosmic rays as pure samples of either or as a mixture of the two. The standard input is derived from the elongation rate from the HiRes Stereo and HiRes/MIA composition, [43]. Figure 1.8 shows the elongation plot including the fits used. Above $10^{18.0}\text{eV}$ the mixture is a constant 80% proton 20% iron mixtures.

3.2 Database

Using the data taken in the given trigger epochs it is possible to model the thresholds and sky noise seen by the detector. This information is processed off line after the data has been taken and is added to the Monte Carlo. As the experiment is simulated on a data set by data set basis this must be done for every period. The sky noise is taken from the variances of each tube over the given period. As the electronics are AC-coupled the pedestals are constant but the variance will increase with increased sky noise.

3.3 CORSIKA Shower library

The **CO**smic **R**ay **SI**mulation for **KA**scade (CORSIKA) [44] program, written by the Karlsruhe Cosmic Ray group in Germany, simulates a single EAS for a given primary particle and energy. The shower is propagated through the atmosphere taking into account interactions and decays. The user can select from a range of hadronic interaction models including QGSJET and SIBYLL. The output of the program is either the longitudinal profile of the shower or the distribution of particles at a given observation level. A longitudinal profile is most applicable for fluorescence detectors, while the later option is more applicable for ground arrays the later output. The program was used by Andreas Zech to create a Shower library to be used as an input for MCRU. A mono energetic set of 200 showers are thrown at a discrete set of zenith angles. From this the Gaisser-Hillas fit parameters are stored, see section . The behavior of the showers is then found as a function of energy and angle. This enables us to throw any energy and the shower

is scaled to the correct shape.

3.4 Detector Response

Once the geometry has been selected and a shower from the shower library chosen and scaled appropriately it is broken up into segments. The number of charged particles in each segment is calculated from the Gaisser-Hillas parameters.

Fluorescence Yield

The flux of fluorescence and Cerenkov photons is calculated for each segment of the shower. The fluorescence yield has been measured by many experiments over the years [7, 45, 46, 47]. These experiments have measured the relative line strengths as a function of wavelength, the spectra, and the overall yield for a given wavelength range. The Monte Carlo is able to implement any of the spectra or their yields. For the standard input we use the Bunner spectra normalized to the Kakimoto result. For a systematic study of the fluorescence yield see section 6.3. All wavelengths in MCRU are split into sixteen 9nm bins, starting at 280nm. Only a fraction of the charged particles, those above threshold, will create Cerenkov light [48]. This fraction is known from simulations as a function of altitude and is correctly modeled.

Atmosphere

Once the light is generated it is attenuated by several atmospheric and experimental processes. The atmospheric component can be broken up into 2 parts, molecular and aerosol. The molecular atmosphere (nitrogen and oxygen) absorption properties are well understood. We are interested in the UV wavelengths (300-400nm) which are much larger than the molecules and the electric field can be thought to be constant across them. Therefore Rayleigh scattering theory can be used. This component changes little with variation in temperature and pressure. A purely molecular atmosphere is the best possible for viewing and therefore a baseline in the experiment. In the Monte Carlo the molecular transmission is modeled as in equation 3.1.

X_S is the observation level and x_R the Rayleigh attenuation length which are $860g/cm^2$ and $2969g/cm^2$ respectively. The heights of the upper and lower edges of the segment being viewed are denoted by h_1 and h_2 while h_R is the Rayleigh scale height which is 7.5km. Finally λ is the wavelength and θ the zenith angle for the viewed segment.

$$T_R = \exp \left[-\frac{X_S(e^{-h_2/h_R} - e^{-h_1/h_R})}{x_R \cos \theta} \left(\frac{400nm}{\lambda} \right)^4 \right] \quad (3.1)$$

An analytic description of aerosol scattering is not possible. Aerosols range from water vapor to dust particles, changing the dielectric constants, and size $10^{-6}cm$ to $10^{-3}cm$. Also due to their nature the aerosol component of the atmosphere can change rapidly. However most of the aerosols exist below 1km which is the lowest altitude viewed by HiRes at a distance of 19km. The aerosol transmission is modeled as in equation 3.2. The aerosol scale height is h_A and the horizontal attenuation length x_A . $f(\lambda)$ is the wavelength dependence of x_A .

$$T_A = \exp \left[-\frac{h_A(e^{-(h_2)/h_A} - e^{-(h_1)/h_A})}{x_A f(\lambda) \cos \theta} \right] \quad (3.2)$$

Experimental attenuations include the HiRes filter and photo tube response. These are all wavelength dependent and have been measured in the laboratory, see figure 2.3.

For each night run the Monte Carlo reads in the total run time and a list of the dead mirrors. Dead mirrors were found by histogramming the number of hits by mirror and night. Some mirrors were dead for several nights before they were repaired. Due to army activity 2 mirrors were off for the whole of data set 4. The mirror run time is required to correctly sample the detector conditions.

Another important effect is the width of the shower. As the shower develops its width increases due to Rayleigh scattering of the constituent particles. The functional form was described by Nishimura-Kamata-Greisen (NKG) in [49]. The light is now ray traced from the shower to the detector. This takes into account the shadow of the cluster box and cracks between photo tubes.

Many people have been responsible for creating and updating the simulation. Zhen Cao worked on the NKG function and PMT acceptance. Stan Thomas wrote the ray tracing routines and Stefan Westerhoff the secondary trigger. Andreas Zech added the atmospheric and trigger database, CORSIKA shower library, Cerenkov light lateral distribution function and corrections for the first 3 trigger epochs. My work involved adding the YAG and Radiosonde database, Mirror reflectivity database, a new form for the particle energy loss, updating the fluorescence yield and updates for trigger epochs 4, 5 and 6.

3.5 Electronic Simulation

Noise is added to the signal and random tube hits are used to simulate background sky noise. Once the amount of light in each tube is known the electronic response must be correctly simulated. The gain of the photo tubes is set so that one photoelectron corresponds to one FADC count. The signal is then shaped by a four-pole filter and the output is a voltage as a function of the 100ns time slice. For a description of the electronic see section 2.2.

3.6 Triggering Changes

As described in chapter 2 the HiRes-II detector trigger has undergone several revisions. Table 2.2 summaries the changes. In order to correctly calculate the aperture these were implemented in the code. The effect of the changes in trigger can be seen in figure 3.1. It shows the number of photo-electrons per degree for the 3 of the trigger epochs.

The primary trigger requires 2 or more threefold coincidences in the rows or column sums during a $5\mu\text{s}$ window. This has remained constant throughout the lifetime of the experiment. One of the most important changes was the adjacent mirror trigger, enabled from data set 2 onward. Data set 4 was a minor change from data set 3. The secondary trigger was altered to tighten the cut on in time clusters. Data set 5 was the most dramatic change to the trigger. The confirming (DSP) scan thresholds were adjusted dynamically based on the variance of the tubes from the data already taken. This meant the inclusion of another database describing

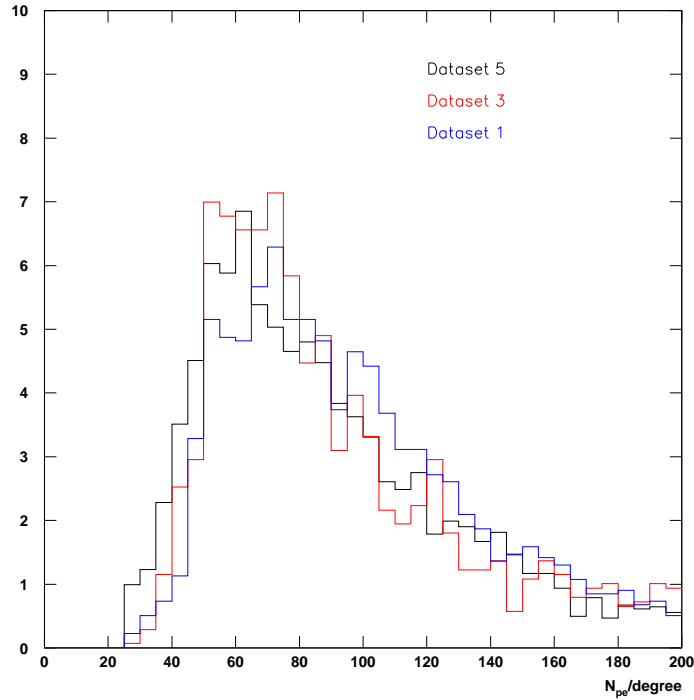


Figure 3.1: Number of Photo-electrons per degree for all events in data sets 1, 3 and 5.

the tube variances on an hourly bases. For each thrown event a day is selected and an hour sampled from this day. The tube thresholds are then calculated and applied to the electronic part of the simulation. Data set 6 raised the minimum threshold to between that of data set 4 and 5. The number of hits required in the secondary trigger was lowered from 3 to 2.

3.7 Simulation Output

The output is written in the exact format as the detector itself with the added FMC1 bank containing the exact thrown values, which are used to assess the resolution of the reconstruction. A histogram file is generated saving the thrown distributions of geometry and energy. The thrown energies are required for the aperture calculation.

Chapter 4

Event Reconstuction

4.1 DST Data Structure

After the event is triggered the data is recorded to disk and stored in a binary format. It is then sent to NEVIS laboratories. There it is processed and turned into “DST files”. Data Summary Tapes (DST) is a way of storing information and provides an interface that allows a user to access information about an event. The DSTs are organized in Banks which are grouped properties of an event. In programming terms they are Structures (C/C++) or Common blocks (FORTRAN). The DST libraries contain the functions for retrieving and writing the information to disk. This enables it to be platform independent.

The analysis of the HiRes-II data takes place in stages. We call this the analysis chain. Each link in the chain takes the current information about an event and calculates an new set of information. This is then stored with the previous information in a new DST file. The HiRes-II reconstruction programs were written by Douglas Bergman.

4.2 Shower Detector Plane

The first stage in the analysis is to find the Shower Detector Plane (SDP), seen in figure 4.1 which is defined as the plane including the shower core, detector and impact point. Using the raw FADC data, a program called RUFPLN finds the tubes in the event, their average time and number of photo-electrons. This final parameter is the number of FADC counts above pedestal. Starting with brightest tube, in the largest cluster of tubes, pattern recognition software finds the SDP by looking for a line in space in and time. A line is fit to the tubes and more tubes

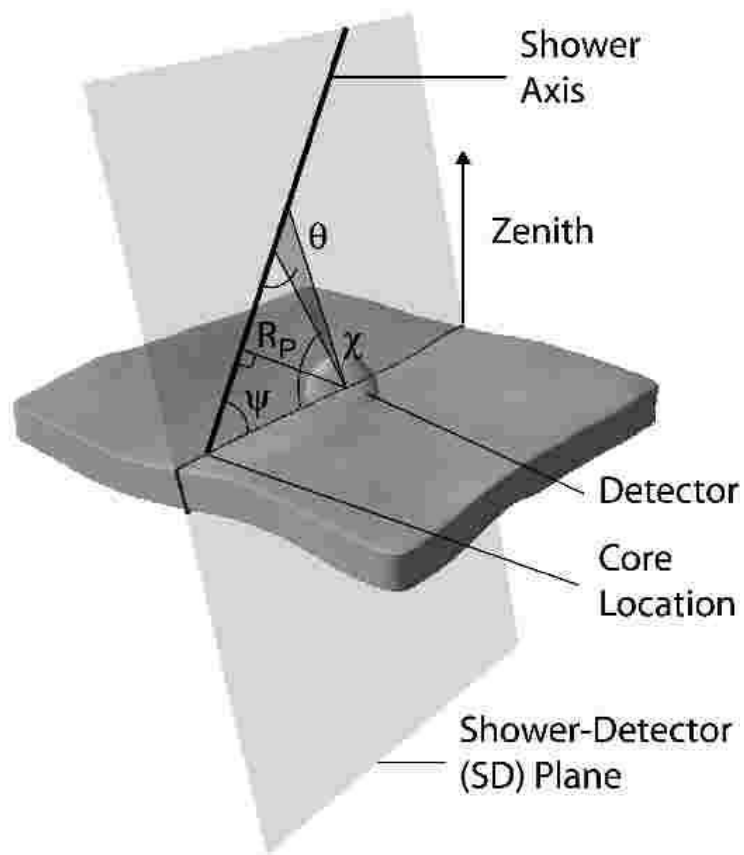


Figure 4.1: Standard Shower Geometry and Parameters.

are added and removed based on these fits. Cuts include any tube that is more than 5° from the line. Finally tubes included in the fit are designated “good tubes”. Those that remain are “bad tubes” which are out of time with the event and are caused by background sky noise and scattered light.

Figure 4.2 shows the mirror view for an event which triggered on the 10th May 2002. It shows the air shower passing down through both rings including mirrors 10, 9 and 7. Small points show the positions of the PMTs and large points show the position of the PMTs that include hits. Along the edge of the mirrors the red represents the vertical and horizontal sums that makeup the trigger. The size of the marks are proportional to $\log(\text{signal})$.

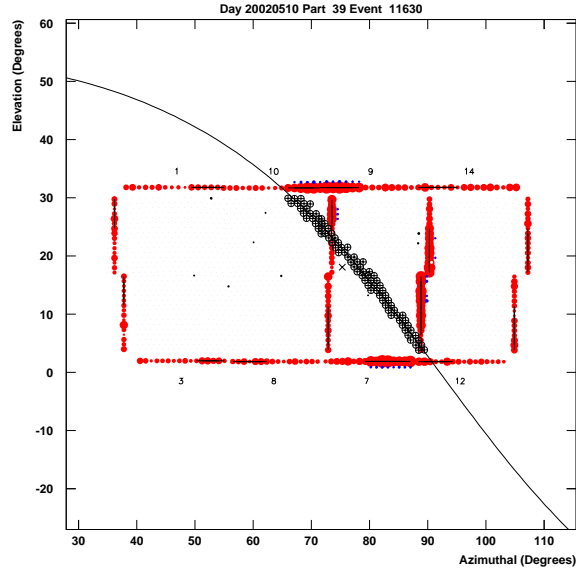


Figure 4.2: Event Recorded on May 10th 2002 Mirror View.

4.3 Event Geometry

Figure 4.1 shows the standard picture for defining the air-shower geometry variables. The shower axis and the detector form the SDP. ψ is defined to be the angle between the shower axis and the detector-core axis. A final parameter is needed to define the shower. The impact parameter. R_p is the closest distance of approach of the shower axis to the detector.

In monocular mode using the position of the tubes along the SDP and the time the signal arrives in the tube, R_p and ψ can be found by fitting the data to equation 4.1.

$$t_i = t_0 + \frac{R_p}{c} \tan \left(\frac{\pi - \psi - \chi_i}{2} \right) \quad (4.1)$$

Here t_i and χ_i are the times and position along the SPD of the i^{th} tube. To aid the fitting process 3 fits are done. The first is a linear fit to the Time vs Angle plot seen in figure 4.3. Next is the pseudo-tangent fit. This is the same as equation 4.1 where ψ has been fixed at 90° . The results from each iteration are used as starting parameters to the next fit.

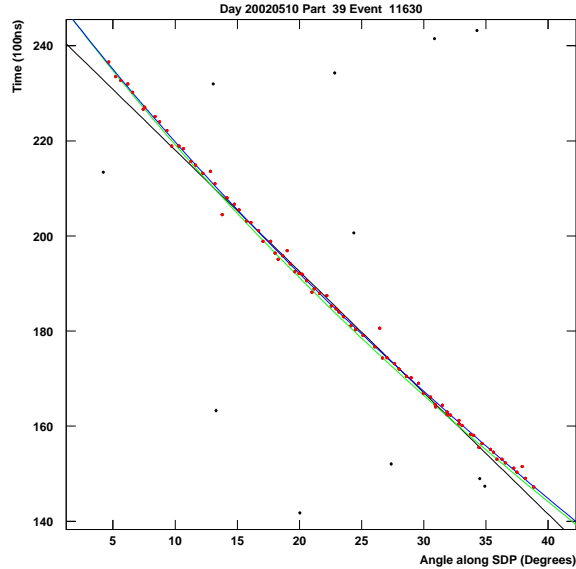
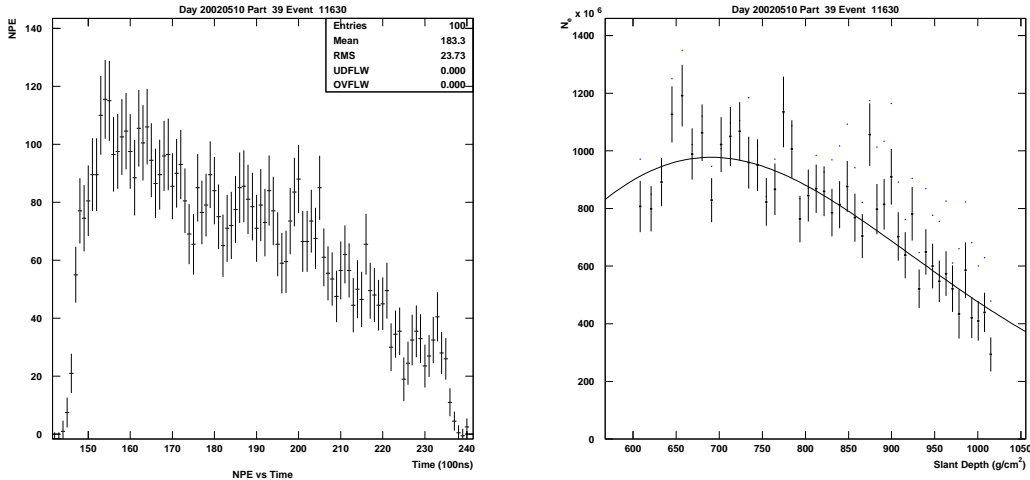


Figure 4.3: Time vs Angle Plot. Red tubes are “Good”. Black tubes are “Bad”. Line are fits described in text.

Figure 4.3 shows the results of these fits. Good tubes are shown in red and bad tubes in black. The bad tubes can be clearly seen to be out of time with the event. Three fits are also included in the figure, where the black line corresponds to the linear fit, the green to the pseudo fit and the blue to the full tangent fit.

4.4 Longitudinal Profile

The next link in the chain is performed by the RUSPGF program. It initially recalculates the shower geometry by scanning over values of ψ and re-deriving the R_p and t_0 . For each value of ψ a shower profile is calculated. The signal in each photo-tube is binned in time (see figure 4.4a) and light is propagated back to the shower. Using the Monte Carlo routines the correct amount of scintillation and Cerenkov light is generated along the shower track and the atmospheric transmission is applied to the light propagated to the detector. Figure 4.4b shows the result of this calculation.



(a) Number of photons as a function of time.

(b) Reconstructed Number of Charged Particles as a function of Slant Depth. Line is a fit to the data using equation 4.2.

Figure 4.4: Reconstruction Chain for the May 10th 2002 Event.

4.5 Event Filtering

In order for the next stage of the analysis to run correctly the events need to be filtered. The iterative nature of the program means that some events do not reconstruct at all while taking up valuable computer time. `FILT_SPGF` opens each event and applies a loose set of cuts to remove these entries.

4.6 Inverse Monte Carlo

Another more accurate method of obtaining the shower profile is the Inverse Monte Carlo Method. Using the same routines as the Monte Carlo the shower track is simulated. Light is generated along the track and propagated to the detector. There are 2 types of light produced at the shower. The scintillation light from the nitrogen fluorescence and the Cerenkov light generated as the charged particles move faster than the speed of light through the atmosphere. As well as direct Cerenkov light we also see the scattered Cerenkov light from aerosols and Rayleigh scattering.

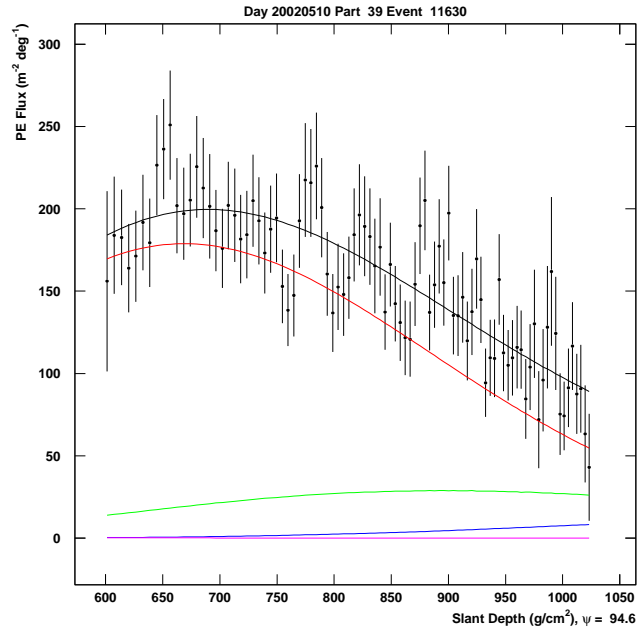


Figure 4.5: Photo-electron Flux as a function of Slant Depth.

After calculating the transmission through the atmosphere mirror reflectivity, filter transmission and photo-tube quantum efficiency are applied and an expected number of number of photo-electrons is calculated. This is then compared to the actual number seen. The shower parameters are varied until they match the data. The depth of shower maximum (X_{max}) is first varied then a simultaneous fit to (X_{max}) and the number of particles at maximum, N_{max} is performed. Figure 4.5 shows the result for the same event. Red corresponds to the fluorescence light, blue the Mie/aerosol scattered, green the Rayleigh scattered and pink the direct Cerenkov light. Black is the sum of all four. The points are the measured flux of photo-electrons.

4.7 Energy Calculation

The final profile is fit to a reduced form of the Gaisser-Hillas function seen in equation 4.2. See section 7 for a full description.

$$N(X) = N_{max} \left(\frac{X - X_0}{X_{max} - X_0} \right)^{\frac{(X_{max} - X_0)}{\lambda}} e^{-\frac{(X_{max} - X)}{\lambda}} \quad (4.2)$$

It describes the number of charged particles as a function of slant depth $X(g/cm^2)$ with four free parameters. N_{max} the number of charged particles at X_{max} which is the depth at which the shower reaches it's maximum. λ is the shower width parameter and is set to $70g/cm^2$, while X_0 is given the value $-60g/cm^2$ which is the mean from 4 parameter fits to Monte Carlo generated showers.

The energy is then simply defined by equation 4.3 where $\langle \frac{dE}{dX} \rangle$ is the average energy loss per g/cm^2 , which has a value of $2.19MeV/g/cm^{-2}$ for this analysis.

$$E_{cal} = \left\langle \frac{dE}{dX} \right\rangle \int_0^{1400g/cm^2} N(X) dX \quad (4.3)$$

4.8 Missing Energy

However this is not the energy of the primary cosmic ray, E_0 . Neutrinos and muons produced in the shower do not contribute to the fluorescence light. This missing energy is a function of the primary energy and was determined for our analysis by Andreas Zech [42], who compared Monte Carlo thrown at discrete energies to the reconstruct E_{cal} . His measurement compares well with other similar calculations [50]. Figure 4.6 shows the fraction of energy added to the shower as a function of its calorimetric energy, $\log_{10}(E_{cal})$. The parametrization of missing energy shown in figure 4.6 is described by equation 4.4.

$$\frac{E_{cal}}{E_0} = A + B \log_{10}(E_{cal}) + C (\log_{10}(E_{cal}))^2 \quad (4.4)$$

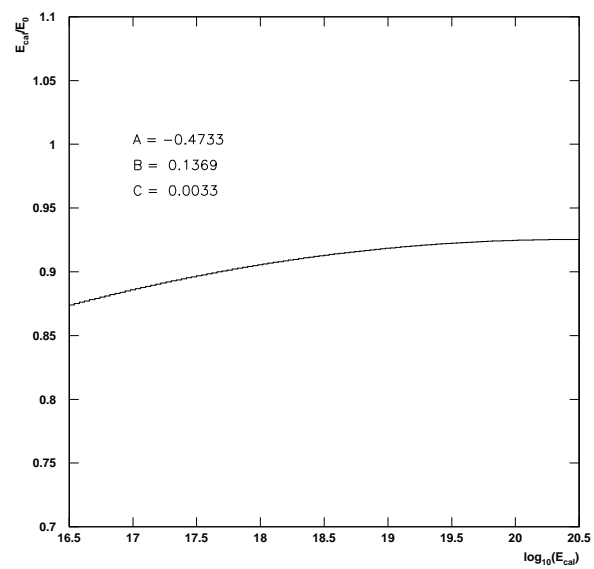


Figure 4.6: Functional form of missing energy.

Chapter 5

Aperture and Energy Spectrum

5.1 Unfolding the Spectrum

In order to calculate the correct cosmic ray spectrum a realistic aperture must be established. This is done using the unfolding method. Unfolding takes into account the detector resolution, which is especially important when measuring such a steeply falling spectrum over 3 decades in energy containing structure. Without unfolding the results cannot be accurately compared to other experiments. This technique is commonly used in optical image reconstruction, radio astronomy and medical imaging. For a complete description see the book by Cowan [51].

In this method Monte Carlo is used to determine a response function, or acceptance, which is the probability the measured value is in bin i , when it should be in bin j . For the spectrum calculation the measured value is the primary cosmic ray energy, E_0 . Using the Monte Carlo the systematic uncertainties due to bias can be estimated by simply comparing two sets of simulations containing different inputs. Equation 5.1 shows how the differential spectrum is calculated.

$$J_{[E_i]} = N_{[E_i]} \frac{1}{\Delta E} \frac{1}{\frac{\nu_i^{MC}}{\mu_i^{MC}} T A \Omega} \quad (5.1)$$

where $N_{[E_i]}$ is the distribution of reconstructed data events which passed all the quality cuts, ν_i^{MC} is the corresponding Monte Carlo distribution which has been reconstructed and cut in exactly the same way. μ_i^{MC} is the distribution of thrown events, i.e. the true values. T is the lifetime of the experiment over the period the data was taken and $A\Omega$ corresponds the geometrical aperture defined in equation 5.2 where θ is the zenith angle, where θ_{max} is 70° .

Data Set	On time (hrs)
1	193.71
2	181.20
3	161.17
4	355.81
5	527.01
6	573.07

Table 5.1: On times for all Data Sets.

ΔE is the width of the energy bins. The total experiment life time (on time) for each data set is described in table 5.1.

$$A\Omega = \int_0^{2\pi} \int_{R_{Pmin}}^{R_{Pmax}} \int_{\theta_{min}}^{\theta_{max}} 2\pi r \sin\theta d\phi dr d\theta = 15910.30 km^2 ster \quad (5.2)$$

The ratio $\frac{\nu_i^{MC}}{\mu_i^{MC}}$ corresponds to the correction factor, C_i . Contributing to C_i are the resolution and detector acceptance. As the simulation of the experiment becomes more accurate the ratio C_i becomes more like the real ratio $\frac{\nu_i}{\mu_i}$ and the bias in the unfolding goes to zero, as shown in equation 5.3.

$$b_i = \left(\frac{\nu_i^{MC}}{\mu_i^{MC}} - \frac{\nu_i}{\mu_i} \right) \mu_i \quad (5.3)$$

5.2 Quality Cuts

Table 5.2 shows a list of the quality cuts used in the analysis. Using these cuts we are able to remove laser and flasher shots and badly reconstructed cosmic rays showers. Poor reconstruction happens when not enough information is contained in the event, e.g. due to short track lengths and low number of good tubes. The amount of Cerenkov light in an event is controlled by removing events with a ψ angle greater than 130° , as Cerenkov light is beamed along the track. Cerenkov light is also controlled by calculating the fraction of light from Cerenkov processes and limiting its contributions to be less than a given fraction. Cuts are also made on the quality of fits to the time vs angle plot and the profile. In order to get a good energy resolution we need

to see the depth of shower maximum X_{max} , which we call bracketing, as the observed depth of maximum is bracketed by our minimum and maximum depths.

Cut	Description	Value
Laser Cut	Second Fraction	0, 0.25, 0.50, 0.75
PseudoDistance	-(Slope of linear TvsA fit)/0.00582	> 1.5km
Angular Extent 1	Track length along shower	> 7 ⁰
Angular Extent 2	Track length if only have 1 ring 2 Mirror	> 10 ⁰
Number of Good Tubes		> 6
Light	Number of NPE/degree	> 25
Shower Detector Plane Angle	abs(SDP)	< 60 ⁰
Linear χ^2 Cut	χ^2 /DOF linear fit	< 10
TVSA χ^2 Cut	χ^2 /DOF 3 parameter fit	< 10
Error ψ		< 36 ⁰
ψ Cut		< 130 ⁰
Cerenkov Cut	Fraction of the light from Cerenkov	< 0.7
Gaisser-Hillas χ^2/DOF		< 10
Bracketing Cut	Xmax is Observed	Xfirst < Xmax < Xlast
Track depth cuts		Xfirst > 150g/cm ² and < 1200g/cm ²
Track Length Cuts		(Xlast - Xfirst) > 150g/cm ²

Table 5.2: List of Quality Cuts.

5.3 Data Monte Carlo Comparisons

The data and Monte Carlo are reconstructed and cut in exactly the same way, using the same programs. We are then able to compare the simulation of the experiment to what is seen in nature. In the following section I will show a series of data-Monte Carlo comparison plots. In these diagrams the top panel black marks represent the data and the red histogram represents the Monte Carlo. The lower panel is the ratio of the data divided by the Monte Carlo, fit to a line. Enough Monte Carlo is thrown to have 5 times the number of events as the data set it simulates. In each case I show the comparisons for data set 4 and 5 on the left and right respectively.

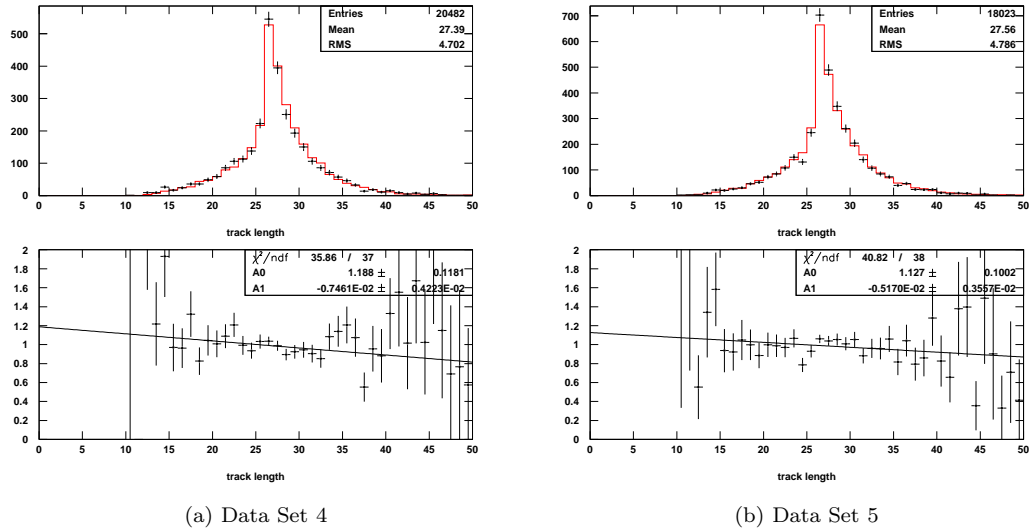


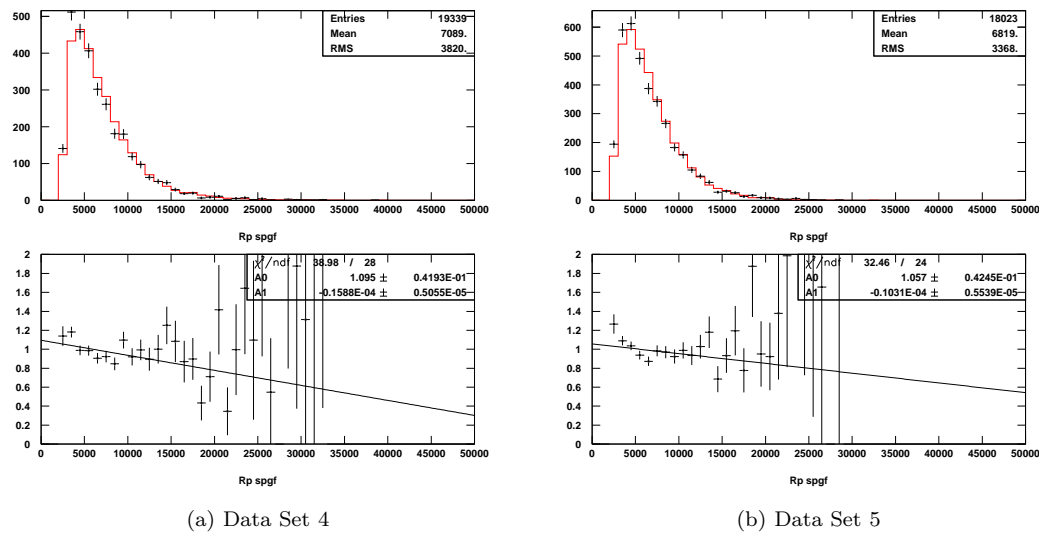
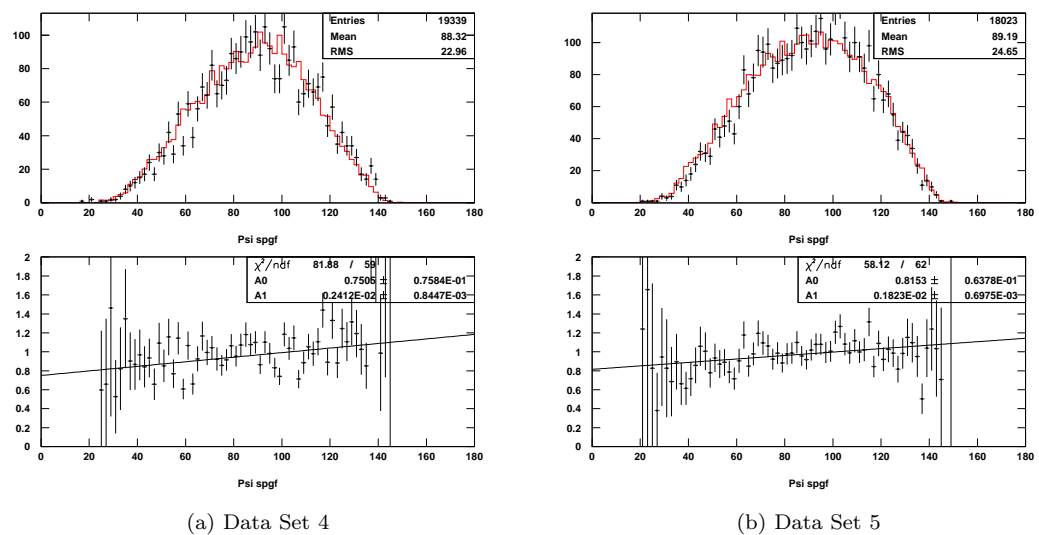
Figure 5.1: Track length of Showers seen in mirrors (degrees).

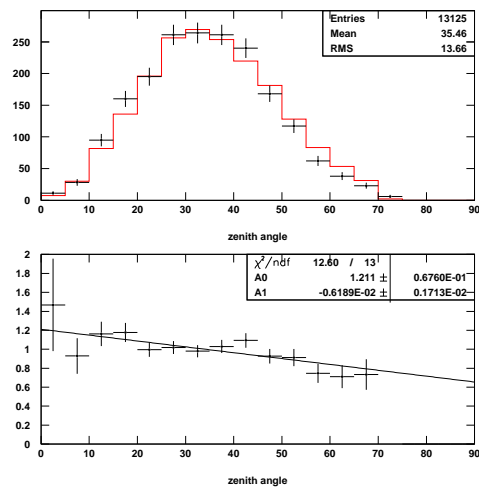
5.3.1 Geometry Comparisons

The first comparisons to look at are those concerning geometry. These are used to check the initial input are correctly thrown. Figure 5.1 shows the track length comparison. The distribution shows a peak at 26° coming from a vertical track passing through both rings. During the first trigger version, which did not include the adjacent mirror trigger, there is a corresponding peak at 12° . The next two comparisons, figures 5.2 and 5.3, show the reconstructed values of R_P and ψ . These comparisons show the Monte Carlo represents the data well. Figure 5.4 contains the zenith angle comparison which shows some discrepancy especially in data set 5. In figure 5.6 we see the distribution of mirrors taking part in events, telling us how well we have taken into account dead mirrors. During data set 4 mirrors 21 and 22 were turned off and this is shown in the plots for both data and Monte Carlo.

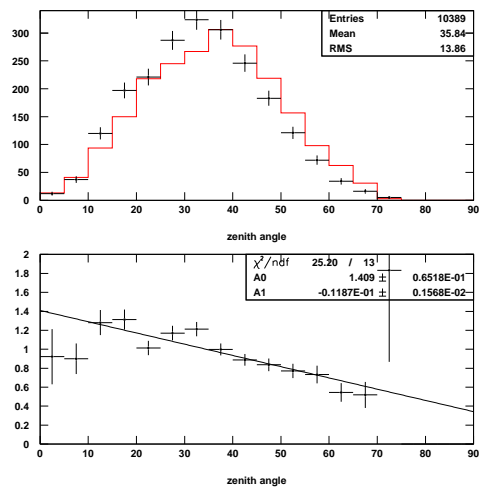
5.3.2 Triggering Comparisons

Quantities that can be used to assess how well the trigger is simulated are the number of photoelectrons and good tubes per degree of track length, shown in figures 5.7 and 5.8 respectively.

Figure 5.2: R_P (km), Closest distance of approach to detector.Figure 5.3: ψ (degrees) as defined in figure 4.1.

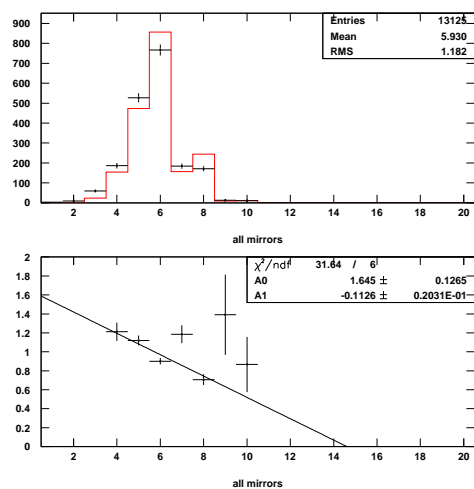


(a) Data Set 4

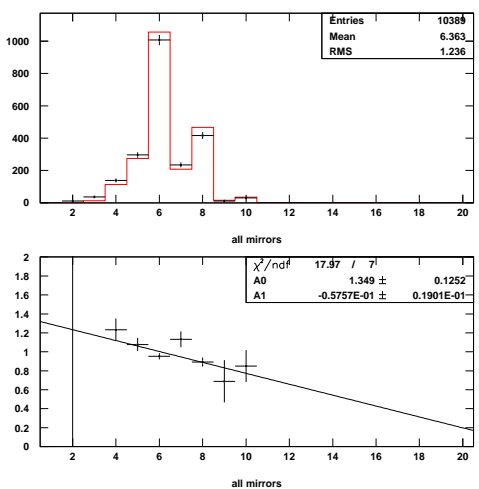


(b) Data Set 5

Figure 5.4: Zenith angle of air shower with respect to the ground (degrees).



(a) Data Set 4



(b) Data Set 5

Figure 5.5: Number of mirrors in each event.

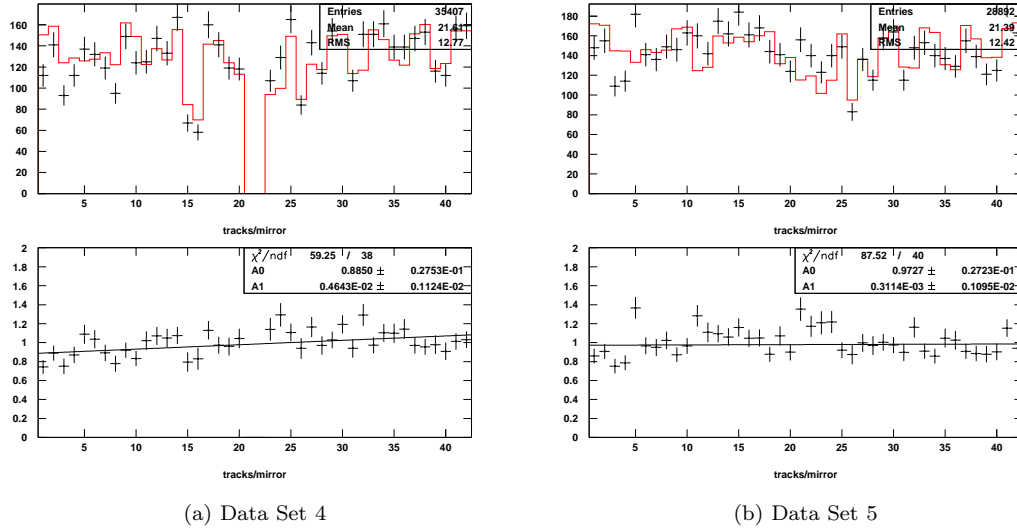


Figure 5.6: Mirror participation.

Also folded into these are the amount of light generated by the Monte Carlo, including the Cerenkov and fluorescence mirror light. If the thresholds in the Monte Carlo do not accurately represent those in the detector these plots would not show good agreement.

5.3.3 X_{max} and Energy Comparisons and Resolution

Figures 5.9 and 5.10 show the comparisons for X_{max} and Energy. The X_{max} distribution displays a small $-20g/cm^{-2}$ shift in Monte Carlo. This suggests the thrown composition, 80% proton to 20% iron, is too heavy. However, we should not tune the MC to match the data and we use the best measurement available, which is the HiRes MIA/Stereo measurement. [43].

The energy comparisons are the final distributions to be looked at and show good agreement between thrown and reconstructed values. In the energy resolution figure 5.12 shows excellent agreement with a $\sim 15\%$ width. Figure 5.11 is the difference between the data and Monte Carlo X_{max} . Both data sets have a width of $\sim 50g/cm^{-2}$ and a mean of less than $10g/cm^{-2}$. For a monocular reconstruction this is very good agreement and is realised through the Inverse Monte Carlo reconstruction method.

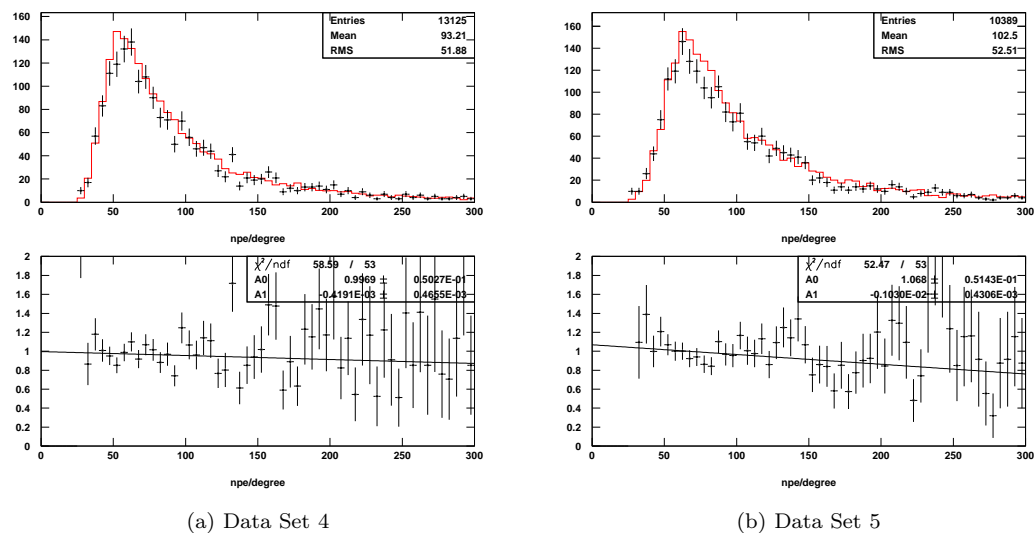


Figure 5.7: Number of photo-electrons per degree of shower track.

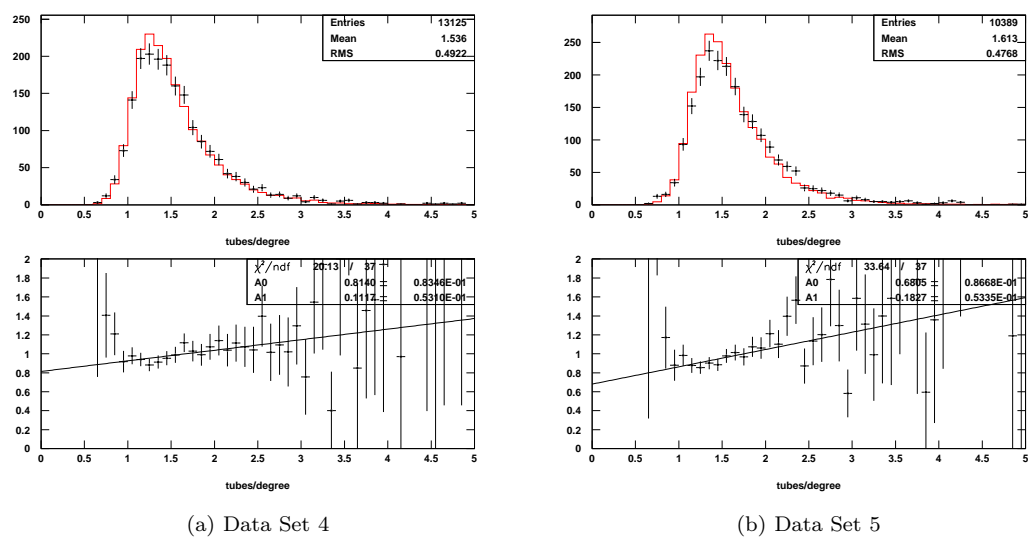


Figure 5.8: Number of good tubes per degree of shower track.

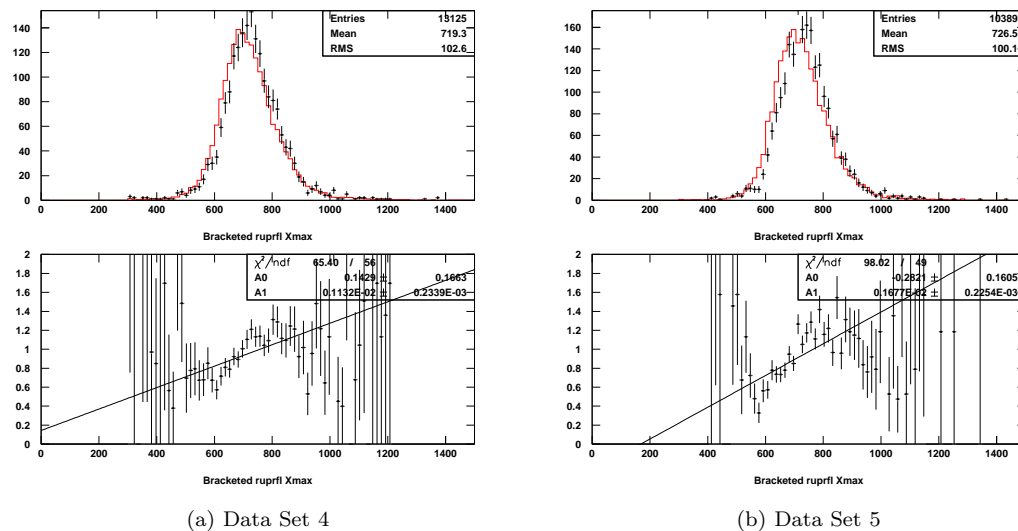
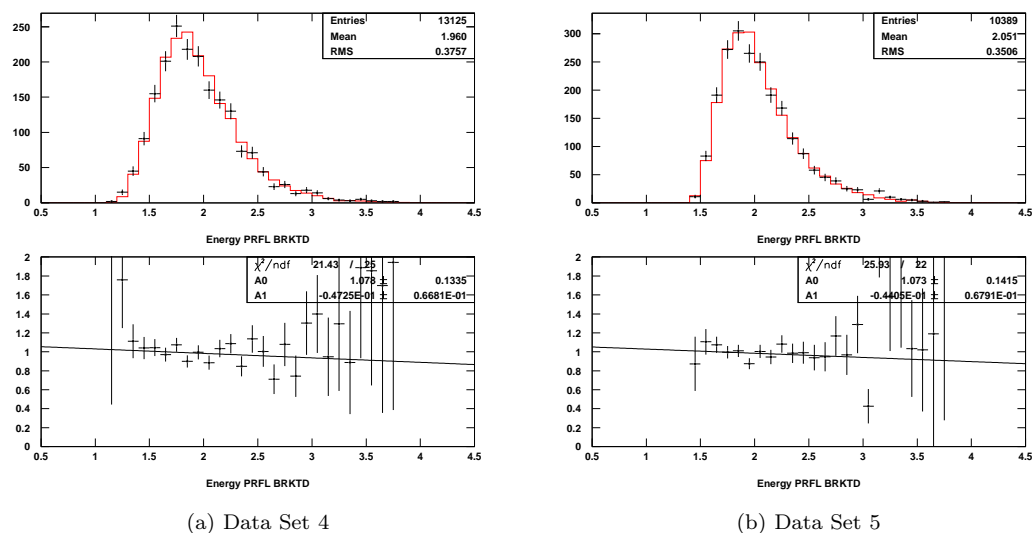
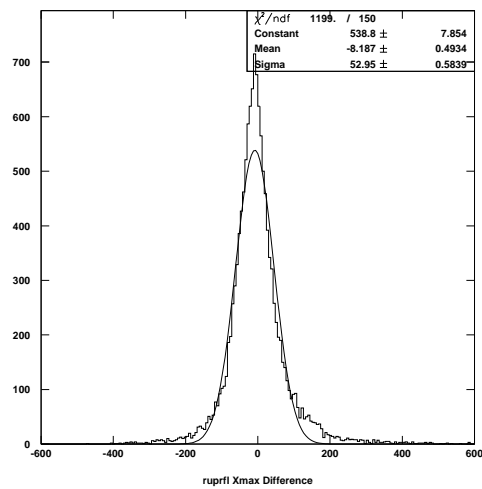
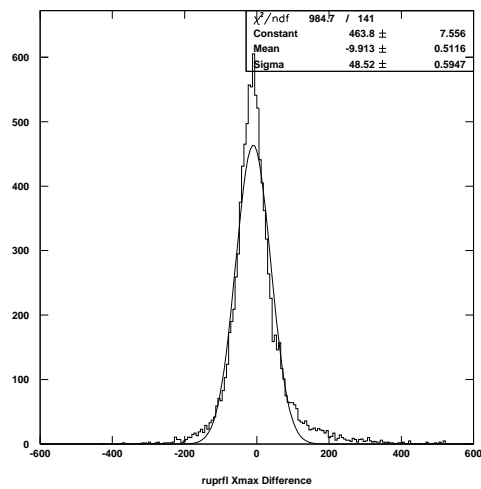
Figure 5.9: Depth of shower maximum, X_{max} (g/cm^{-2})

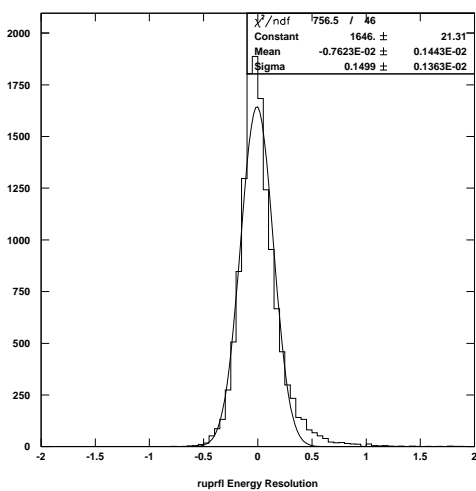
Figure 5.10: Primary Energy of cosmic ray.



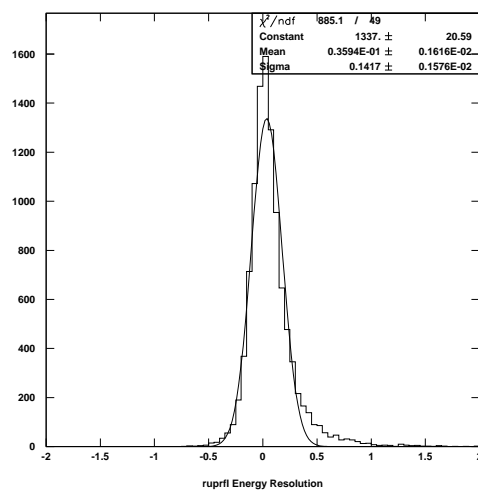
(a) Data Set 4



(b) Data Set 5

Figure 5.11: X_{max} Difference, Reconstructed - Thrown (g/cm^2).

(a) Data Set 4



(b) Data Set 5

Figure 5.12: Energy Resolution of Primary Cosmic Ray.

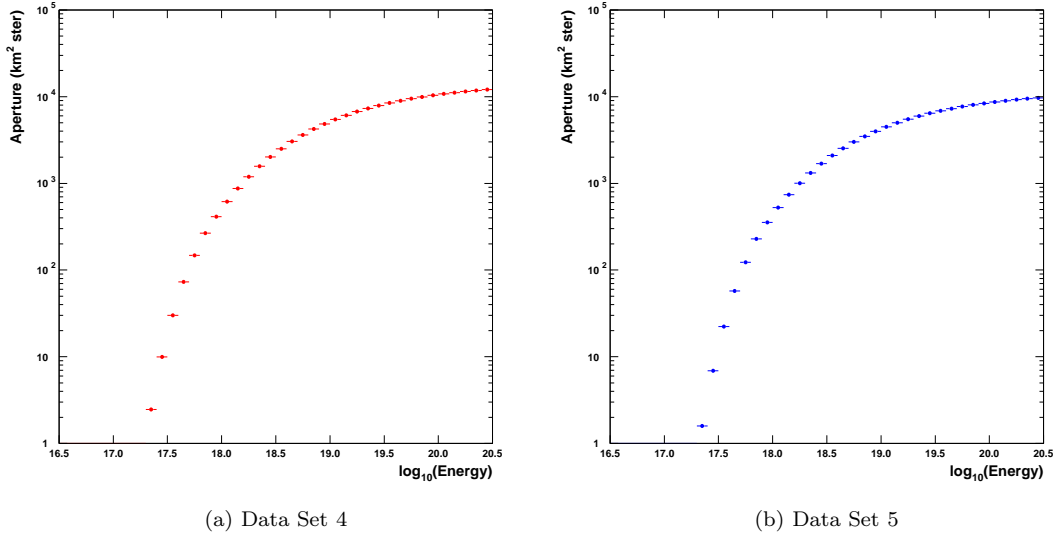


Figure 5.13: HiRes-II Aperture.

5.4 Aperture and Exposure

Once we are happy that the Monte Carlo describes the data well we can calculate the aperture, which is taking the ratio of the events that pass the detector triggering, reconstruction and quality cuts to the overall number of thrown events and multiplying by the geometrical factor A , as seen in equation 5.4. Figure 5.13 shows the apertures for data sets 4 and 5 in units of $\text{km}^2 \text{ ster}$. We see the aperture initially increases rapidly as a function of energy from $10^{17.0} \text{ eV}$.

$$Aperture = \frac{\nu_i^{MC}}{\mu_i^{MC}} A \quad (5.4)$$

The exposure is now simply the aperture multiplied by the live time of the experiment. In order to smooth the exposure we fit to 5.5 shown in figure 5.14 where A , B and C are fit parameters.

$$Exposure = e^{(A(1 - e^{-B(\text{Energy} - C)})} \quad (5.5)$$

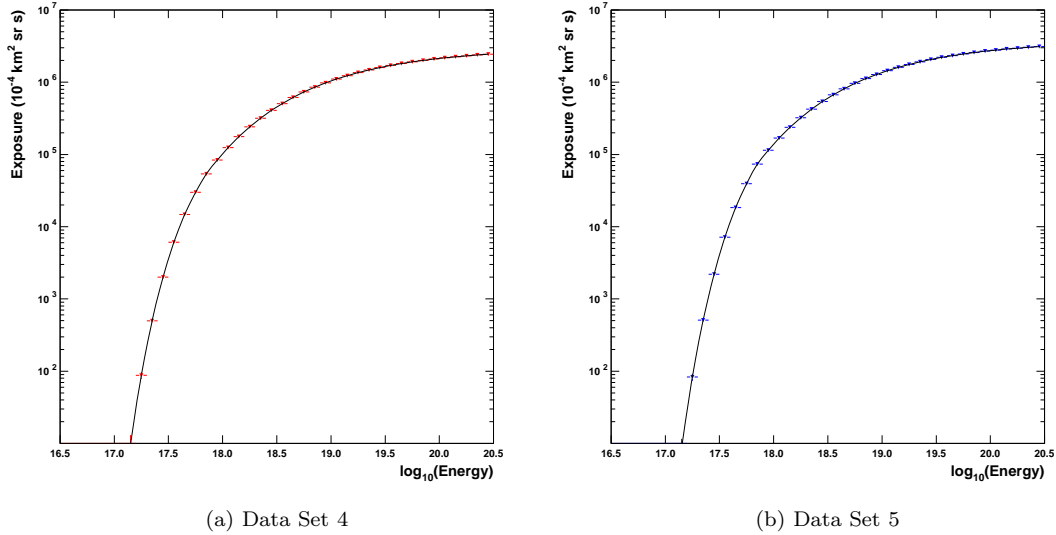


Figure 5.14: HiRes-II Exposure

5.5 Spectrum

Using equation 5.1 we calculate the spectrum. Figure 5.15 shows the differential flux for cosmic rays in units of $E^3/10^{24}eV^2m^{-3}s^{-1}ster^{-1}$. Spectra from both HiRes-I and II are shown. The HiRes-II spectrum extends lower in energy thanks to the 2 rings of mirrors giving coverage up to 31^0 . (Lower energy cosmic rays do not penetrate as deep into the atmosphere.) This work involved only the HiRes-II spectrum, the HiRes-I spectrum was calculated independently by a group at the University of Utah.

The flux has been multiplied by energy cubed in order to emphasize the features. Most striking of these is the cutoff or end of the spectra seen at $\sim 10^{19.8}eV$ caused by pion production on CMB photons as described in section 1.7. At $10^{18.6}eV$ there is a dip identified as the ankle which is a result of e^+e^- -production off the CMB. In figure 5.16 shows the same result plotted with the AGASA result [52]. The AGASA experiment, which was a ground array, appeared not to show a cutoff.

Figure 5.17 shows the original spectra for data sets 1 to 3 and the new spectra for data sets 1 to 5. The final bin at $10^{19.8}eV$ has dropped. The aperture increased but there were no more

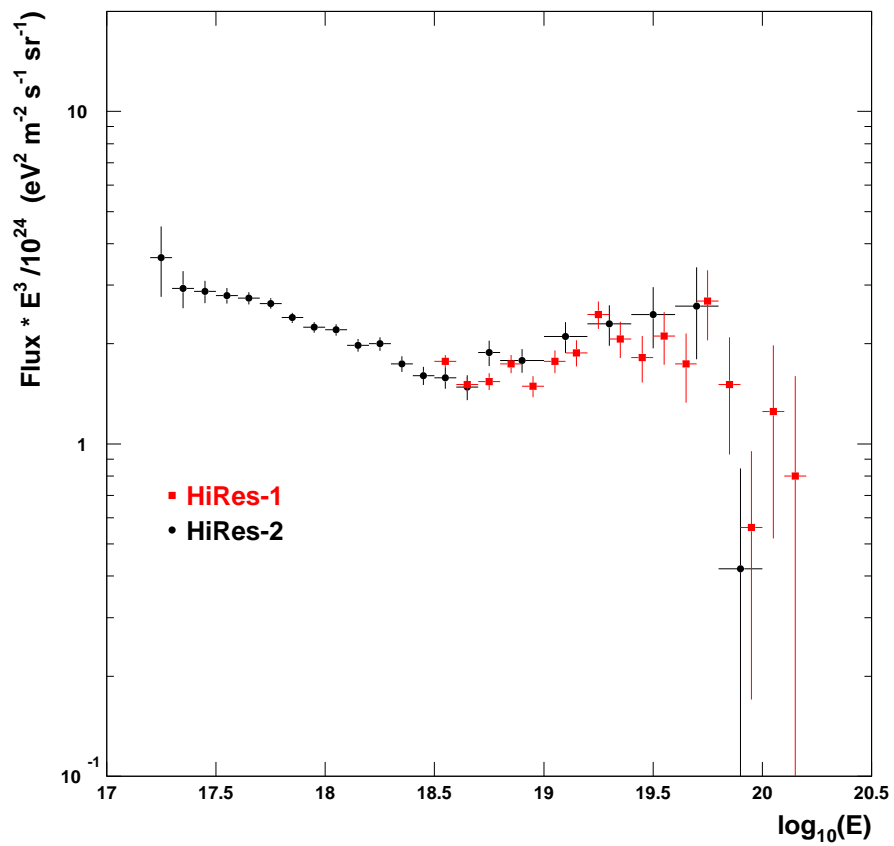


Figure 5.15: Cosmic Rays Spectra for HiRes-I and HiRes-II.

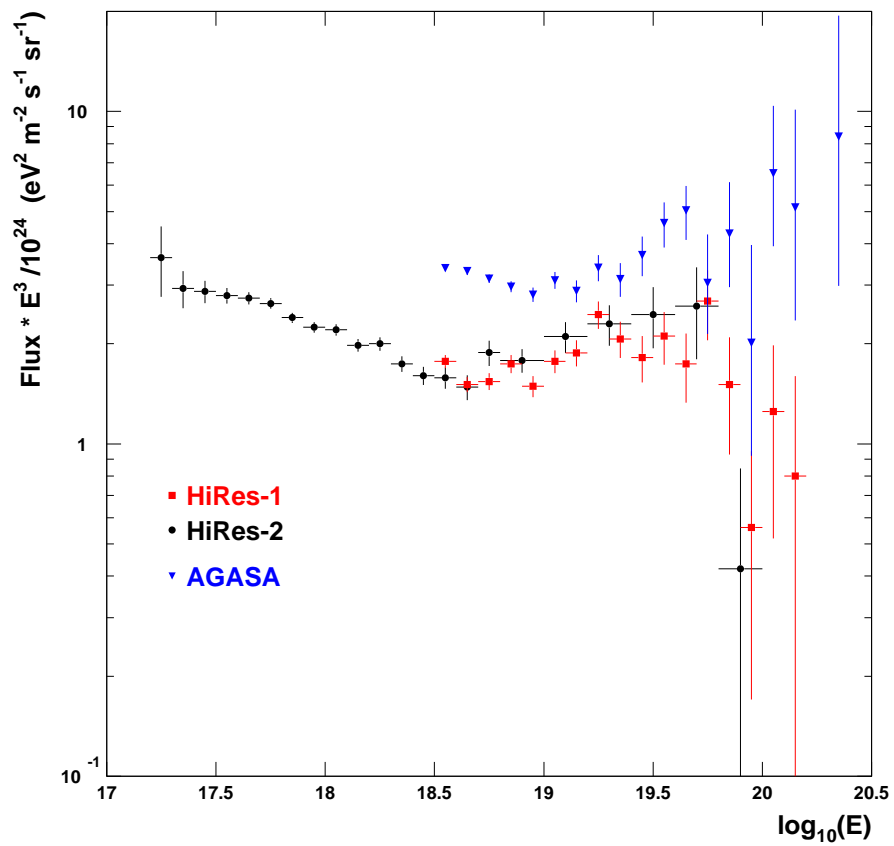


Figure 5.16: Cosmic Rays Spectra for HiRes-I, HiRes-II and AGASA.

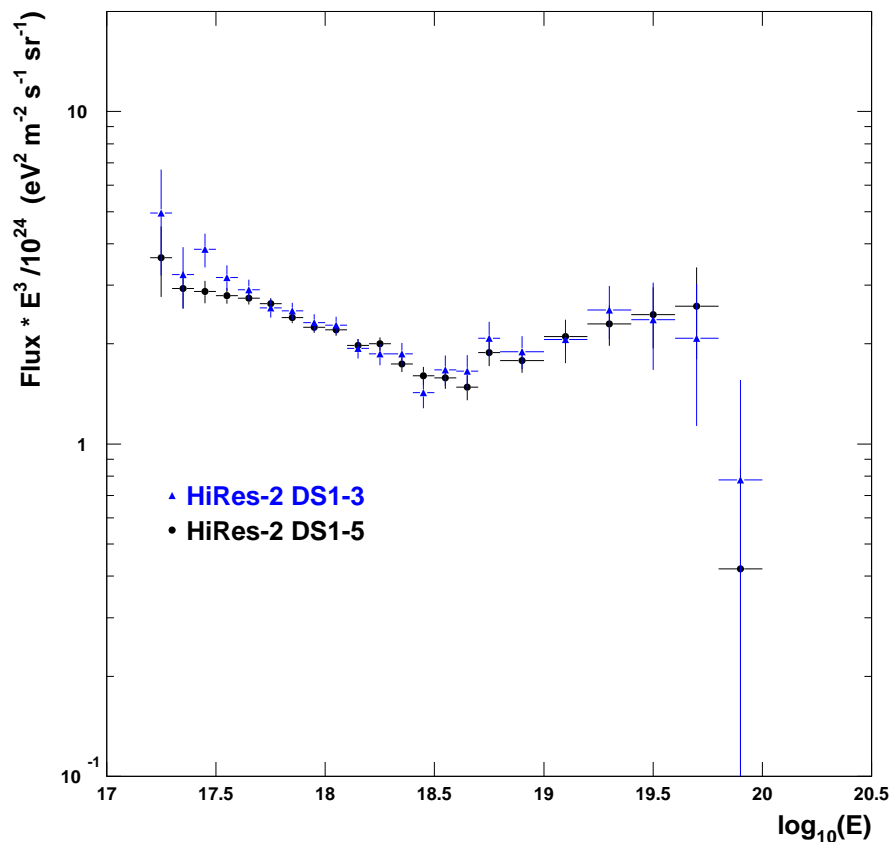


Figure 5.17: Cosmic Rays Spectra for HiRes-II for data sets 1-3 and 1-5.

data events recorded in that energy bin.

The following plots compare the spectra to other experiments. Figure 5.18 shows the HiRes prototype-MIA result. Due to the large view in elevation, up to 70° , it was able to probe lower in energy. However the small aperture and short run time meant it could not reach above $10^{18.5}\text{eV}$. Figure 5.19 compares HiRes-II to the Fly's Eye Stereo result. It agrees well, also showing the ankle, however the aperture was not large enough to see the G.Z.K. cutoff. The final two plots show the Auger SD and Hybrid results [53, 54]. Auger SD also shows a cutoff but at a lower energy than HiRes. The hybrid result appears to show an ankle but because fluorescence operates for only 10% of the surface detector has low statistics at higher energies.

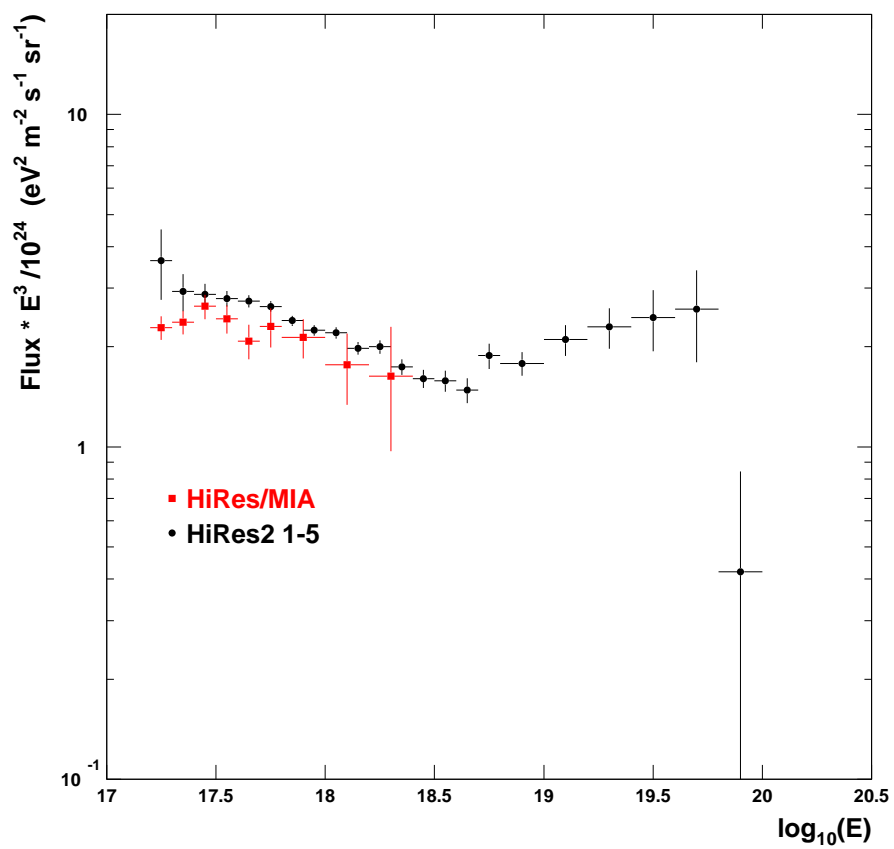


Figure 5.18: Cosmic Rays Spectra for HiRes-II and the HiRes Prototype-MIA experiment.

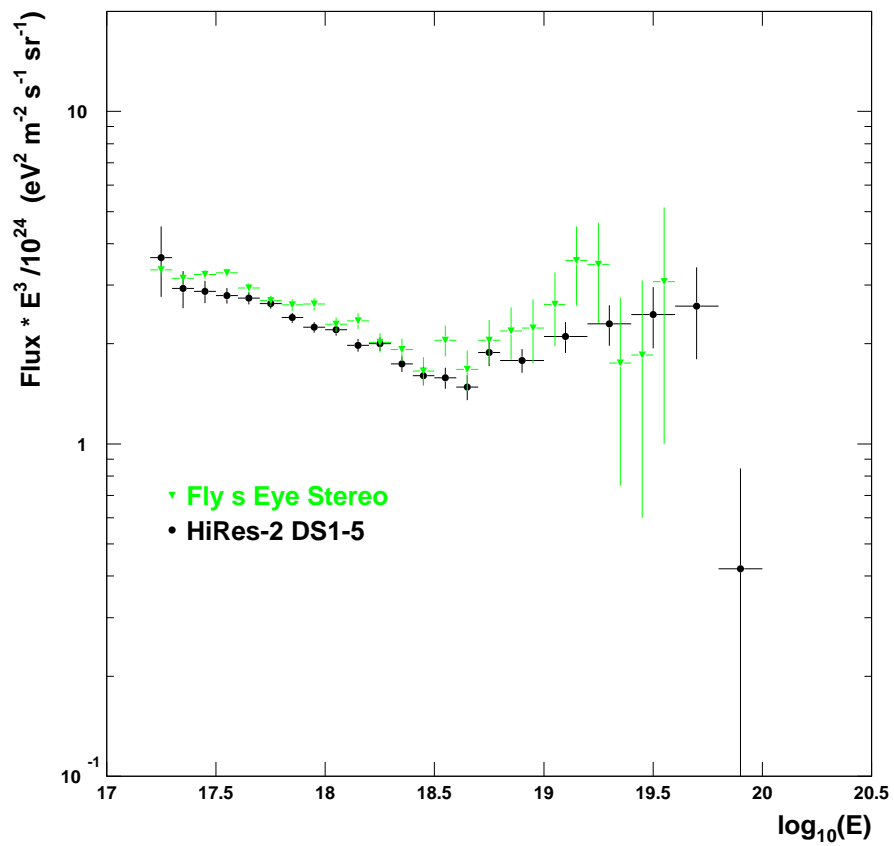


Figure 5.19: Cosmic Rays Spectra for HiRes-II and Fly's Eye Experiment.

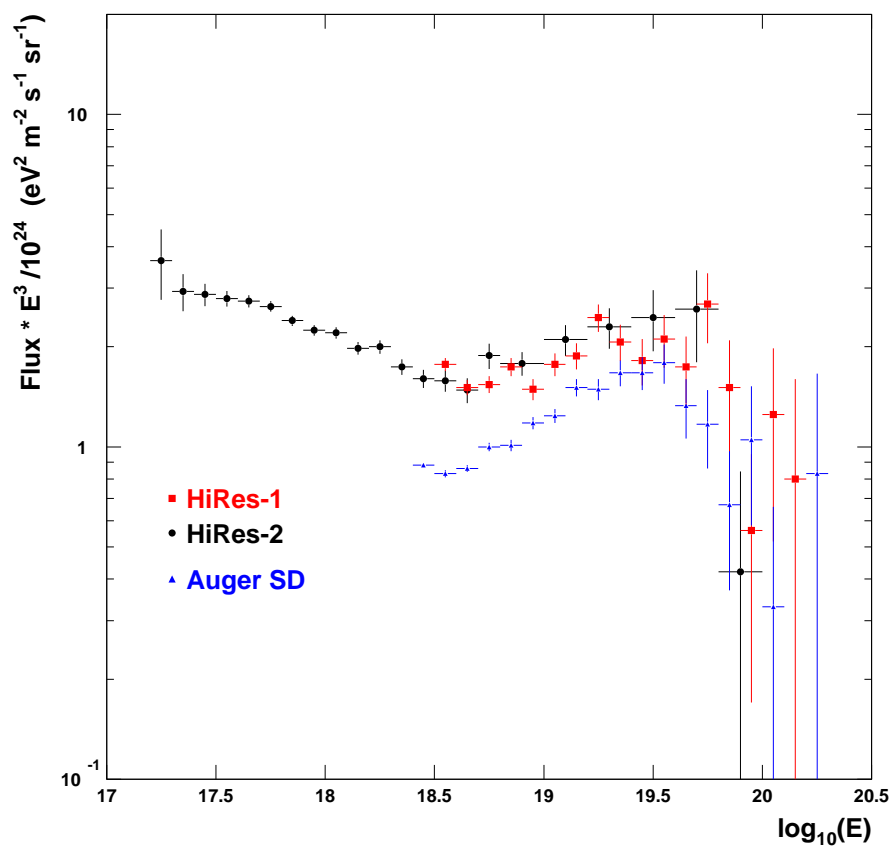


Figure 5.20: Cosmic Rays Spectra for HiRes-I, II and Auger Ground Array.

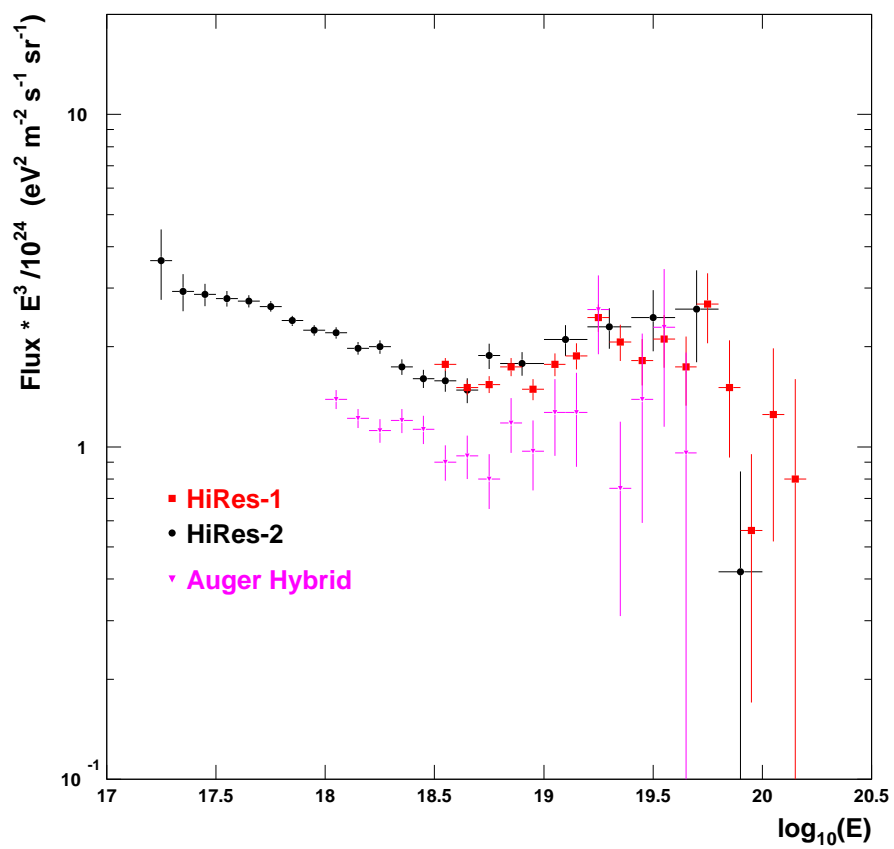


Figure 5.21: Cosmic Rays Spectra for HiRes-I, II and Auger Hybrid Result.

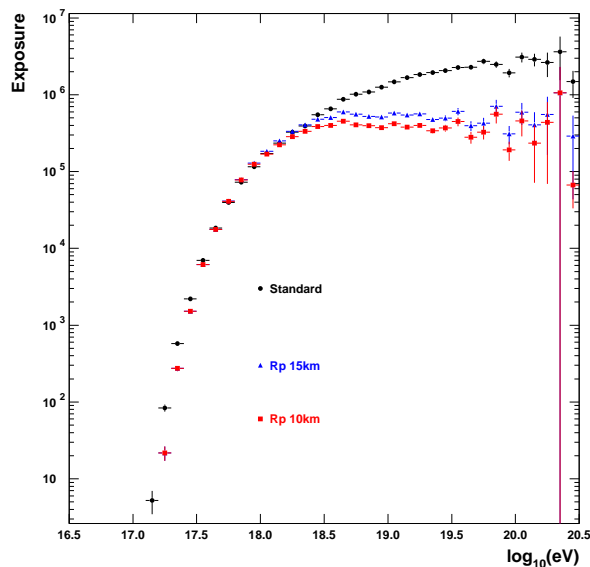


Figure 5.22: Exposure for Datasets 1 to 5 with R_P cuts.

5.6 Constant Aperture Check

By making cuts on R_P we can change the shape of the aperture so that it will be flat as a function energy. If the same cuts are applied to the data the structure of the spectrum will be visible in the raw energy distribution. Figure 5.22 shows the exposure for HiRes-II cut in three different ways. Black represents the standard cuts, blue has an added cut of $R_P < 15\text{km}$ and red $< 10\text{km}$. From about 10^{18}eV the aperture now becomes flat. By taking the energy histogram for the same set of cuts and multiplying by energy squared we see the structure of the spectrum, as shown in figure 5.23. At $10^{18.5}\text{eV}$ there is evidence for the ankle in the 10km cut data.

5.7 Fits to the Spectrum

In order to characterize the spectrum, fits are made to the combined HiRes-I and II flux. Douglas Bergman made fits with multiple break points where the break is allowed to float. Figure 5.24 shows the spectrum with no breaks. The fit gives a spectral index of $3.13(1)$, defined as γ in

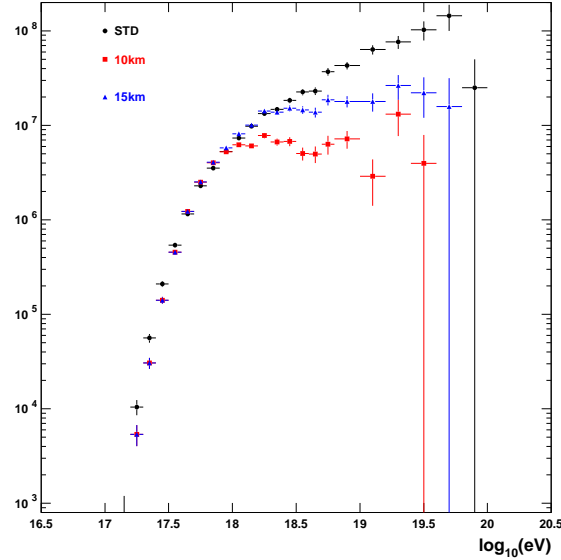


Figure 5.23: Primary Energy Distribution of Cosmic rays $\times Energy^2$

equation 5.6 and a χ^2 of 162 for 39 degrees of freedom.

$$Flux \propto Energy^{-\gamma} \quad (5.6)$$

The effect adding of one break point is seen in figure 5.25. The break at 4.3(5)EeV finds the Ankle and reduces the χ^2 to 63 for 37 degrees of freedom. The index's is 3.24(2) below the break and 2.89(3) above. Adding a second break, the fit chooses the energies 4.5EeV and 56EeV which is where we expect to find the GZK cutoff. The χ^2 is now 34.7 for 35 degrees of freedom. The indices's are now 3.24(1), 2.81(2) and 5.4(7). This information is summarized in table 5.3. Adding a further break point does not significantly reduce the χ^2 .

By continuing the fit from the Ankle beyond the cutoff (red line figure 5.26) we can calculate the expected number of events in the event the break did not exist. This is found to be 51.1 while the actual number seen is 15, corresponding to a chance probability of 3.9×10^{-9} . However HiRes-I and II have many events in common. By reducing the statistical weight of the HiRes-I points by the number of events in common the chance probability becomes 7.0×10^{-8} , a

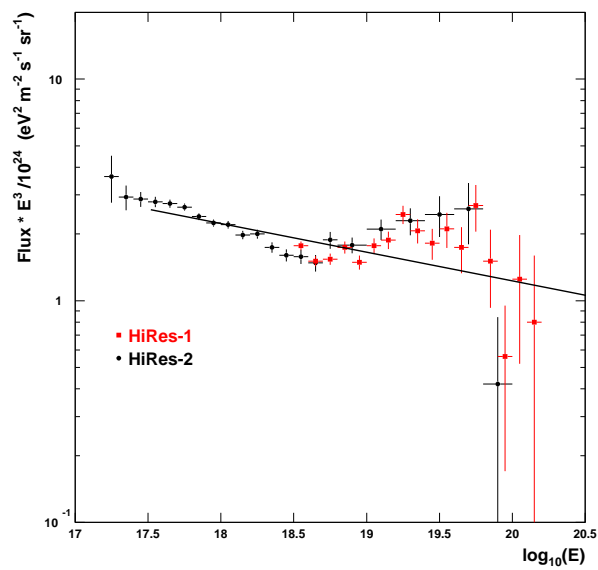


Figure 5.24: HiRes-I and II Spectrum with single γ fit.

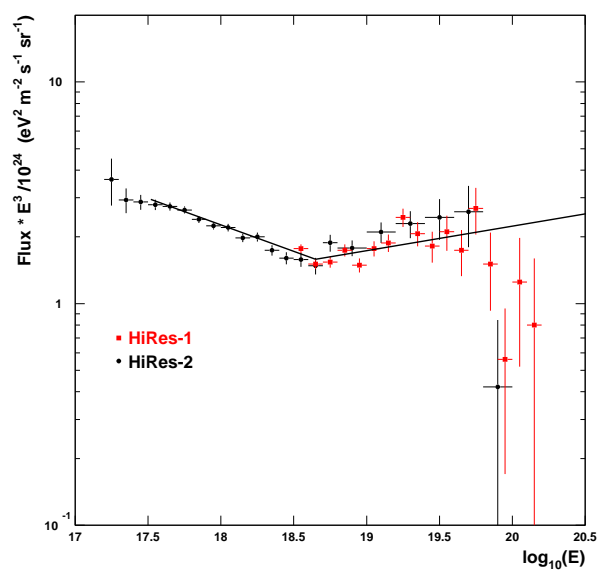


Figure 5.25: HiRes-I and II Spectrum with 1 break point fit.

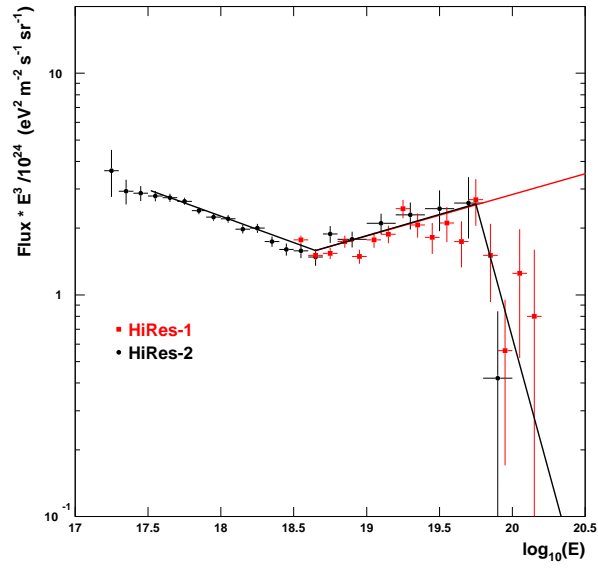


Figure 5.26: HiRes-I and II Spectrum with 2 break point fit.

Number of Breaks	χ^2/DoF	γ	Energy (EeV)
0	132/39	3.13(1)	-
1	63/37	3.24(2) 2.89(2)	4.3
2	34.7/35	3.24(2) 2.81(3) 5.4(7)	4.5 56

Table 5.3: Summary of Spectrum Fit Information.

significance of 5.3σ .

logE	Bin	Events	Exposure \times dE/ 10^{30}	Flux $\times 10^{30}$	Flux $\times E^3/10^{24}$
17.25	0.1	22	0.03	646.7	3.64
17.35	0.1	69	0.26	261.6	2.93
17.45	0.1	184	1.43	128.3	2.87
17.55	0.1	366	5.86	62.5	2.79
17.65	0.1	585	19	30.79	2.74
17.75	0.1	762	51.24	14.87	2.64
17.85	0.1	812	120.2	6.75	2.4
17.95	0.1	742	234.4	3.17	2.24
18.05	0.1	679	435.4	1.56	2.2
18.15	0.1	544	774.2	0.7	1.98
18.25	0.1	471	1325	0.36	2
18.35	0.1	340	2191	0.16	1.74
18.45	0.1	252	3514	0.07	1.61
18.55	0.1	194	5487	0.04	1.58
18.65	0.1	139	8364	0.02	1.48
18.75	0.1	132	12480	0.01	1.88
18.85	0.1	81	18270	0	1.57
18.95	0.1	74	26310	0	1.99
19.1	0.2	91	89550	0	2.03
19.3	0.2	53	171100	0	2.46
19.5	0.2	24	314400	0	2.41
19.7	0.2	11	560100	0	2.47
19.9	0.2	1	973500	0	0.51
20.1	0.2	0	1659000	0	0
20.3	0.2	0	2786000	0	0

Table 5.4: Summary of HiRes-II Events and Spectrum

Chapter 6

Systematics of the HiRes-II Spectrum

6.1 Introduction

The HiRes experiment finished taking data in April 2006. We have observed the G.Z.K cutoff at the 5σ level and the results have been published in Physics Review Letters [55]. The analysis used standard inputs in the reconstruction and Monte Carlo. However during the lifetime of experiment new measurements of inputs including fluorescence yield and mirror reflectivity were made and new techniques for applying particle energy loss, $\frac{dE}{dX}$, were developed. In the following section I will describe several of these improvements and the effect they have on the HiRes energy scale.

6.2 Atmospheric Database

Laser shots were made across the detector volume during the detector operation. From this data it is possible to determine the properties of the atmosphere on an hourly basis. These are the Horizontal Aerosol Extinction Length, the Aerosol Scale Height and Vertical Aerosol atmospheric depth. A depiction of the atmospheric model and how it is applied in the Monte Carlo is described in section 3.4. By running a set of Monte Carlo with the hourly database and the standard atmospheric conditions we can measure the effect of the aperture on the spectrum. Figure 6.1 shows the ratio of acceptances with and without databases. Over all energy ranges there is no change due to this effect.

We can also use the same database on the data and compare the energy change on an event by event basis. This is especial important at the higher energies where there are fewer events

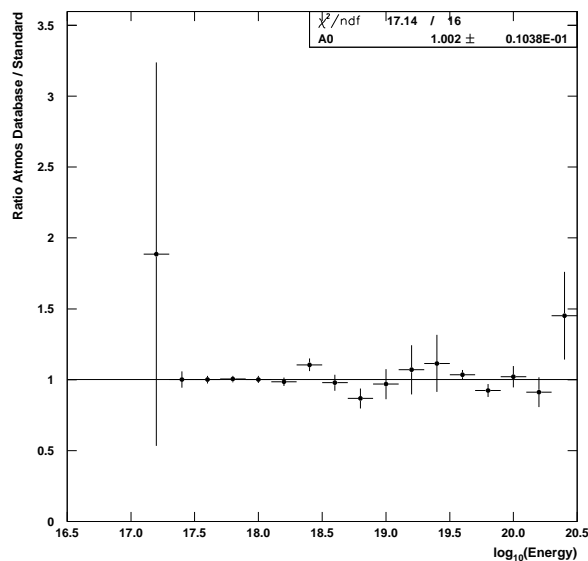


Figure 6.1: Ratio of apertures with the Atmospherics database to the Standards HiRes-II aperture

and any large shift due to changing weather can effect the spectrum disproportionately. Figure 6.2 shows a -3% shift in energy with a 7% width.

6.3 Fluorescence Yield

For a fluorescence detector the atmosphere is the calorimeter as well as the medium through which we observe. The largest systematic uncertainty in this method is the fluorescence yield of Nitrogen excited by the secondary electrons passing though the air. As the mean electron energy is relatively low compared to the primary cosmic ray the fluorescence yield can be measured in the laboratory. Recent measurements have been made with control of systematics uncertainties in mind [47, 56]. As previously described, when a high energy cosmic ray hits the atmosphere it creates a cascade of secondary particles. The energy deposited in the atmosphere is called the calorimetric energy. Some energy is carried away by particles hitting the ground and some by particles such as neutrinos and muons which do not interact. Approximately 90% of the charged particles in the shower are electrons and positrons. The electrons are able to excite

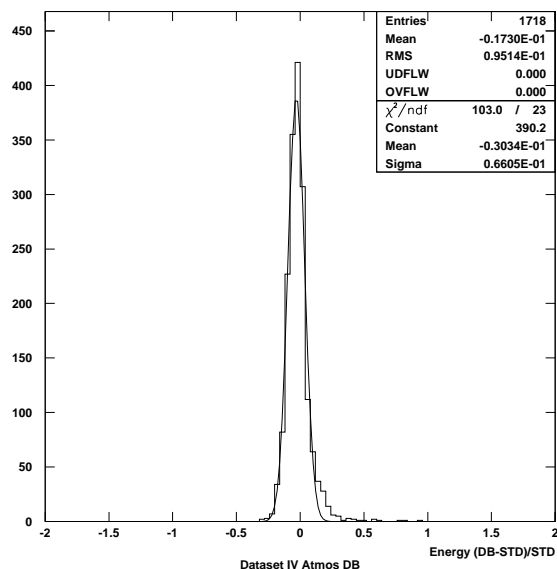


Figure 6.2: Shift in Energy by applying Atmospheric Database.

molecular Nitrogen which then relax to their ground state by isotropically emitting fluorescence photons. The transition are such that the light is in the UV region (300nm-400nm) and the number of photons is proportional to the number of particles.

Nitrogen Fluorescence theory

The complex molecular energy schemes of N_2 and N_2^+ can be seen in figure 6.3. From the transitions shown we obtain the spectrum given in table 6.1 ranging from 290nm to 430nm. The spectrum is dominated by the 337nm line or the $2P(0,0)$ transitions.

An important mechanism in the deexcitation of the the molecules is Quenching. This occurs due to collision of molecules and is therefore pressure dependent and shortens the lifetime of the excited state. Measurements of this effect have been made in the laboratory and the effect has been taken into account in the detector simulation and reconstruction. It is however small and contributes less than 10% for and atmospheric depth greater than $200g/cm^2$ [56].

The total number of fluorescence photons generated per unit path length of the electron ϵ_λ

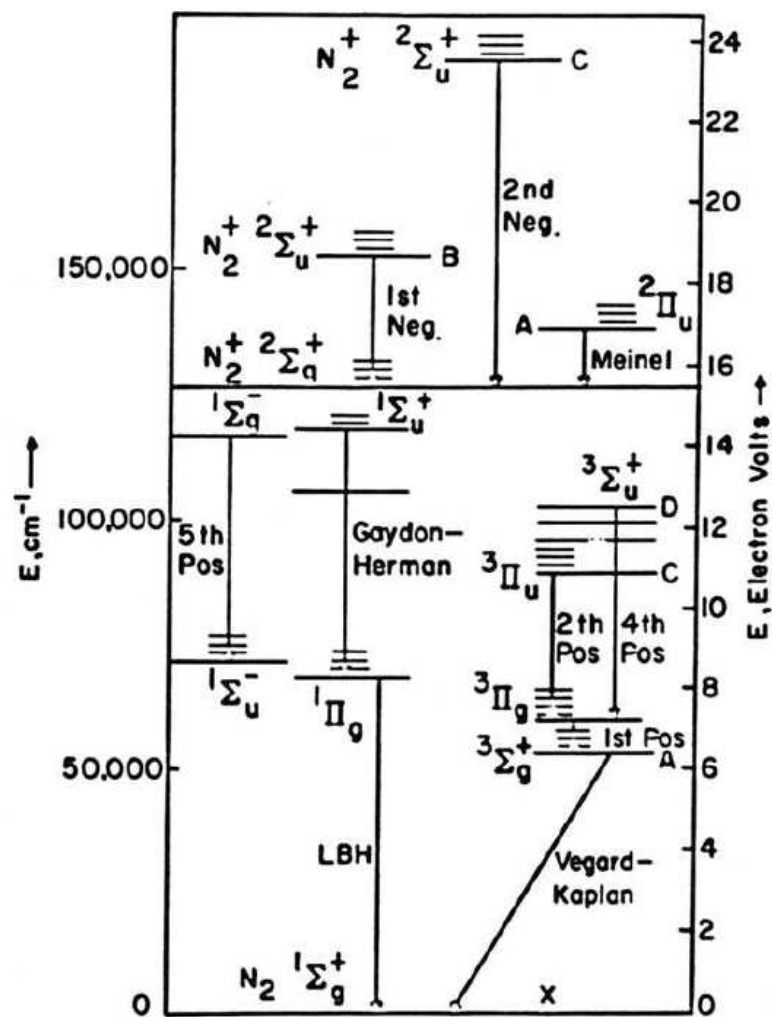


Figure 6.3: Electronic bands of the Nitrogen Molecule [7].

Transition	$\lambda(nm)$	Transition	$\lambda(nm)$
2P(3,1)	296.2	GH(0,5)	366.1
2P(2,0)	297.7	2P(3,5)	367.2
GH(6,2)	302.0	2P(2,4)	371.1
GH(5,2)	308.0	2P(1,3)	375.6
2P(3,2)	311.7	2P(0,2)	380.5
2P(2,1)	313.6	2P(4,7)	385.8
2P(1,0)	315.9	GH(0,6)	387.7
GH(6,3)	317.6	1N(1,1)	388.5
2P(4,4)	326.8	1N(0,0)	391.4
2P(3,3)	328.5	2P(2,5)	394.3
2P(2,2)	330.9	2P(1,4)	399.8
2P(1,1)	333.9	2P(0,3)	405.0
2P(0,0)	337.1	2P(3,7)	414.1
GH(0,4)	346.3	2P(2,6)	420.0
2P(2,3)	350.0	1N(1,2)	423,6
2P(1,2)	353.7	2P(1,5)	427.0
2P(0,1)	357.7	1N(0,1)	427.8

Table 6.1: Nitrogen Fluorescence Yield Transitions and Wavelengths.

is a function of pressure, P and optical cross section, σ_λ .

$$\epsilon_\lambda = N \frac{\sigma_\lambda}{1 + P/P'_\lambda} \quad (6.1)$$

where N is the density of nitrogen molecules and P'_λ is the characteristic pressure for quenching. The fluorescence yield, Y_λ , and efficiency, Φ_λ , follows the same pressure dependence as in equation 6.1.

$$Y_\lambda = Y_\lambda^0 \frac{1}{1 + P/P'_\lambda} \quad (6.2)$$

$$\Phi_\lambda = \Phi_\lambda^0 \frac{1}{1 + P/P'_\lambda} \quad (6.3)$$

where the efficiency at zero pressure is

$$\Phi_\lambda^0 = \frac{\rho A_\lambda h\nu}{(dE/dX)_{dep}} \quad (6.4)$$

where ρ is the density, $h\nu$ the photon energy and A_λ a transmission constant. From equations 6.3 and 6.4 we can write

$$Y_\lambda = \frac{1}{(dE/dX)_{dep}} \frac{\rho A_\lambda}{1 + \rho B_\lambda \sqrt{T}} \quad (6.5)$$

This is the parametrization used in our software packages. Figure 6.4 shows the most important of these measurements. Although all are made at different energies there are some common ideas to the methods used. A source of relativistic electrons is made to pass through a target of air and the intensity of FY photons is measured. A good description of the experimental techniques used can be found in [56]. To find a world average a fit is made to the data in figure 6.4 to the $\frac{dE}{dX}(1cm)$ line. HiRes standard analysis used the Kakimoto normalization [46]. When all the experiments shown except T-461 and airfly are fit we find the total yield increases by 2%. Airfly cannot be used as it only a preliminary result.

The current HiRes-II Monte Carlo and analysis uses the Bunner spectrum normalized to Kakimoto absolute yield [46]. Figure 6.5 shows the normalized spectra for several experiments. All the spectra are binned in the same format in our program. In the analysis the input spectrum seen in figure 6.5, ϕ_i , are used in equation 6.6 and the constants A, B and C are set to get the condition in equation 6.7 which is the Kakimoto result.

The spectra from 6.5 are applied to equation 6.6 to correct for temperature and pressure as a function of wavelength. The constants A, B and C are set to satisfy the condition in equation 6.7 which is the Kakimoto result.

$$\Phi_i = \phi_i \frac{A\rho}{B(1 + \sqrt{T}\rho C)} \quad (6.6)$$

$$\sum_{i=1}^{16} \Phi_i = 3.25\gamma/m/e \quad (6.7)$$

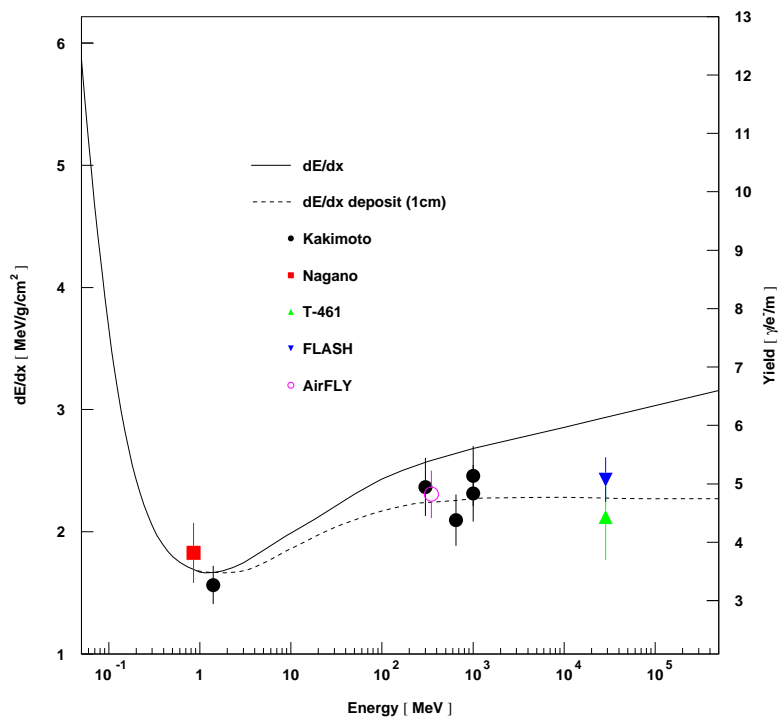


Figure 6.4: Measurements of Fluorescence Yield as a function of energy as compared to $\frac{dE}{dX}$. Solid line is $\frac{dE}{dX}$ of air. Dashed line $\frac{dE}{dX}$ for a thin air target with no knock on electrons - as used in the experiments.

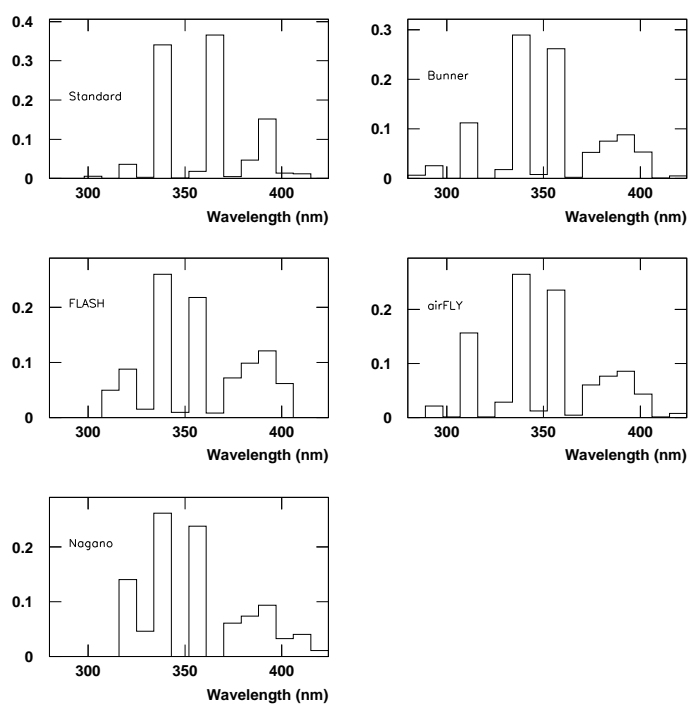


Figure 6.5: Normalized Fluorescence Yield Spectra

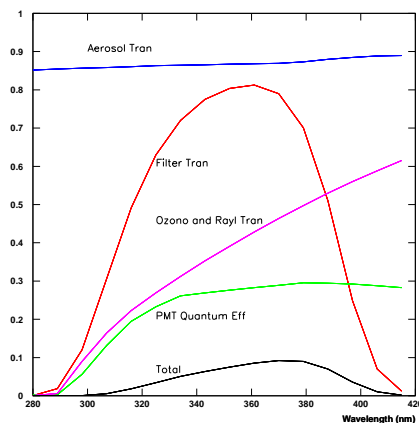


Figure 6.6: Wavelength dependent Transmission Factors.

Applying a new FLY Spectrum

The HiRes filter transmission and the quantum efficiency of the photo-tubes are wavelength dependent. Figure 6.6 shows the values for the transmissions, quantum efficiency and the atmospheric attenuation for the center of a shower 20km away. Applied to Φ and convolved with the mirror reflectivity you get the number of photons arriving at the PMT.

By changing the spectra, ϕ_i , and keeping temperature and pressure dependence constant we change the amount of light seen for the same shower. The total attenuation effectively re-weights the input spectra. The results in table 6.2 show this for the standard and FLASH spectra. Applying the results from figure 6.6 gives the results seen in table 6.3. The totals from this part of the calculation are also seen. The FLASH spectra yields 10% less light than that seen for Standard spectra.

A more detailed calculation that includes mirror reflectivity and the opening angle to the shower gives the information seen in figure 6.7. The estimate of 90% for FLASH is accurate. It turns out to be worse for other spectra, including an 80% shift for the airFLY spectra. From this we can expect a shower analyzed by FLASH spectra will have 10% more energy than standard. Figure 6.8 shows the shift in energy from applying the FLASH spectra compared to that standard.

i	nm	$\phi_{Standard}$	ϕ_{FLASH}	$\Phi_{Standard}$	Φ_{FLASH}
1	280	0.000	0.000	0.000	0.000
2	289	0.000	0.000	0.000	0.000
3	298	0.017	0.000	0.017	0.000
4	307	0.000	0.051	0.000	0.156
5	316	0.118	0.090	0.118	0.276
6	325	0.010	0.015	0.010	0.047
7	334	1.109	0.268	1.112	0.818
8	343	0.004	0.009	0.005	0.029
9	352	0.058	0.224	0.058	0.685
10	361	1.190	0.009	1.193	0.026
11	370	0.017	0.074	0.017	0.225
12	379	0.152	0.102	0.153	0.310
13	388	0.495	0.124	0.496	0.496
14	397	0.045	0.063	0.045	0.194
15	406	0.038	0.000	0.038	0.000
16	415	0.000	0.000	0.000	0.000
Total		3.25	1.02	3.25	3.25

Table 6.2: Normalized Spectra and Total FLY for ground level

i	nm	Standard	FLASH
1	280	0.00000	0.00000
2	289	0.00000	0.00000
3	298	0.00001	0.00000
4	307	0.00000	0.00089
5	316	0.00216	0.00506
6	325	0.00033	0.00160
7	334	0.05645	0.04154
8	343	0.00029	0.00185
9	352	0.00440	0.05149
10	361	0.10178	0.00222
11	370	0.00156	0.02073
12	379	0.01373	0.02793
13	388	0.03468	0.03468
14	397	0.00161	0.00696
15	406	0.00041	0.00000
16	415	0.00000	0.00000
Total		0.220	0.190

Table 6.3: Spectra after attenuation from Figure 6.6

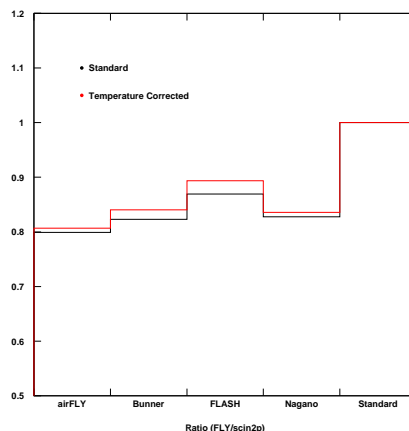


Figure 6.7: Amount of light compared to Standard HiRes.

Due to the wavelength dependent parameters in the experiment changing the FLY spectra, while keeping the overall yield constant, can have dramatic effects in the amount of light expected from a shower. This yields a shift in the reconstructed energy in the data of +5%.

6.4 YAG calibration

Section 2.3.2 describes the HiRes YAG calibration system. On each night the relative gain of every photo tube was measured using the system. Light was distributed from the LASER to each mirror fiber optic cables and diffused onto the surface of each camera. Using this information the analysis and Monte Carlo routines are able to characterize each photo-tube on a night by night basis. Subroutines were added to both programs and the effect of changing from an average or standard to the database can be seen in figure 6.10. It shows a mean shift in the energy of 0.5% with a 7% width. The asymmetry of the distribution comes from the database itself.

6.5 Radiosonde Database

As part of their normal business, airports in the U.S launch radiosonde balloons to measure pressure and temperature at regular heights from 1 to 30km. This information is free and

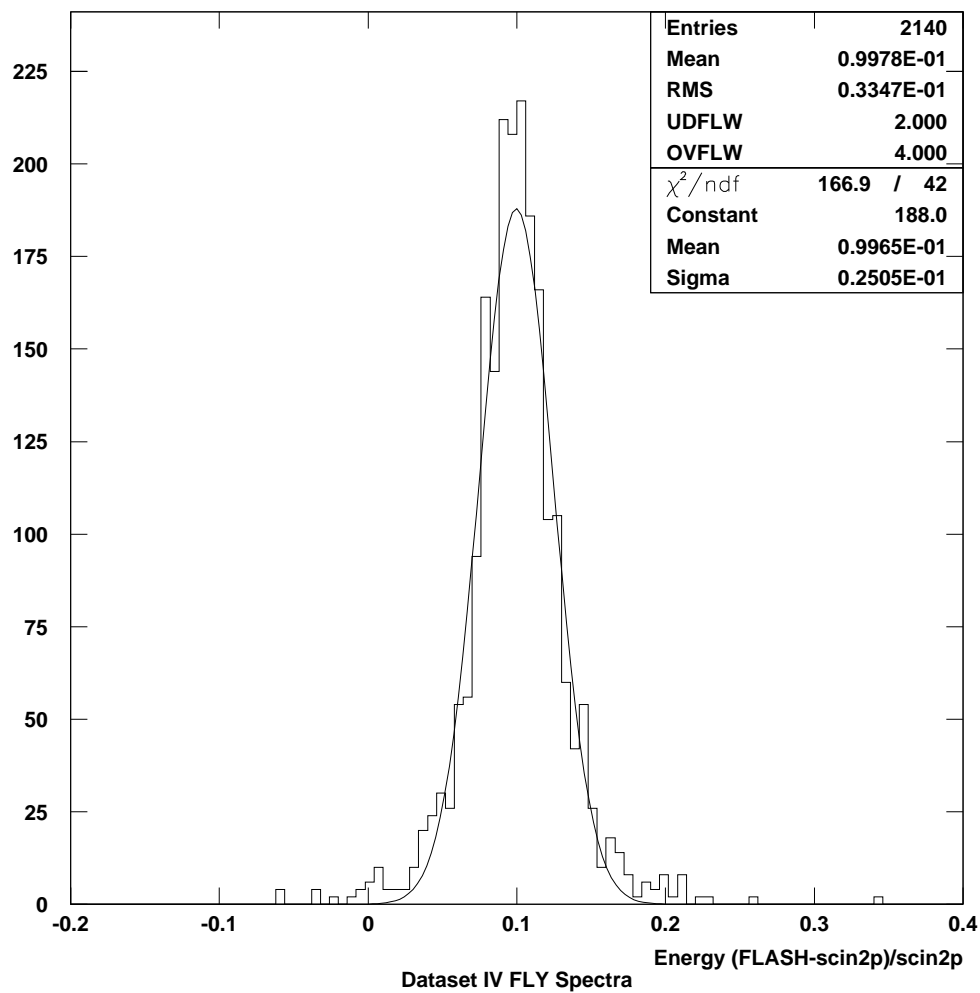


Figure 6.8: Shift in Energy by applying FLASH spectra

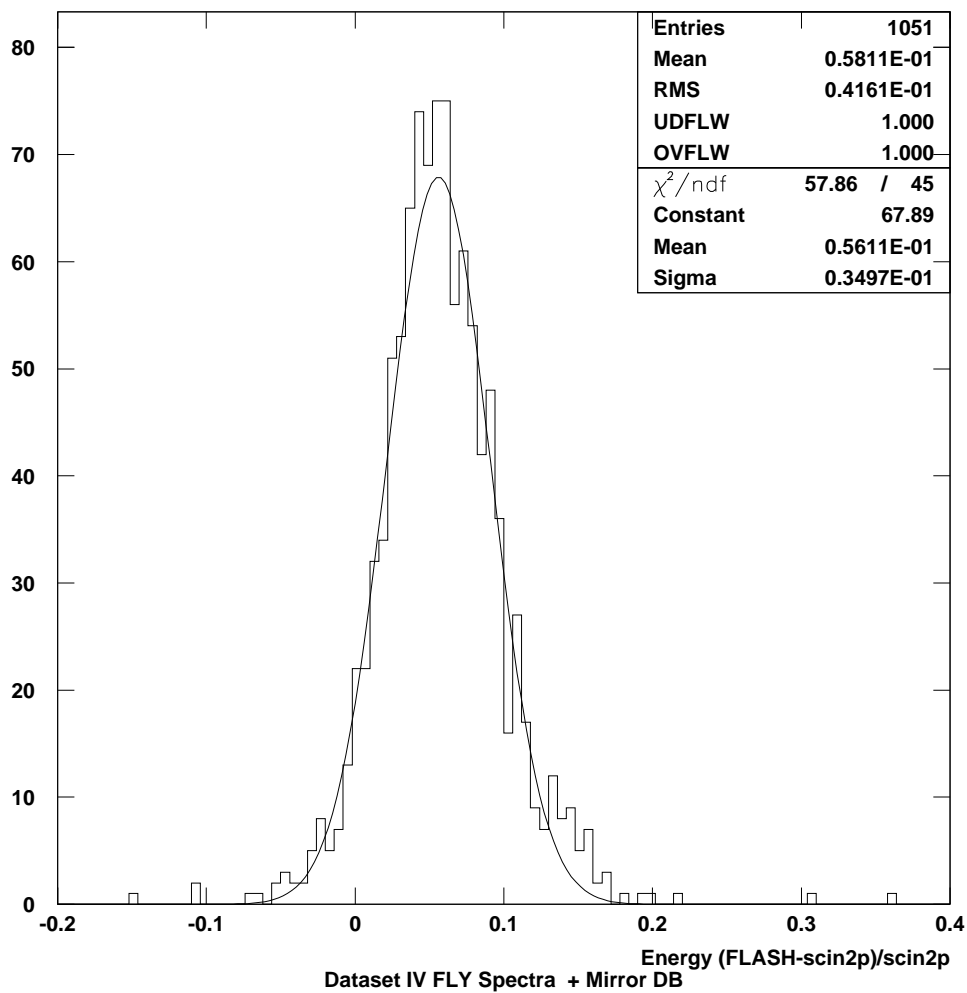


Figure 6.9: Shift in Energy by applying FLASH spectra and mirror wavelength dependence.

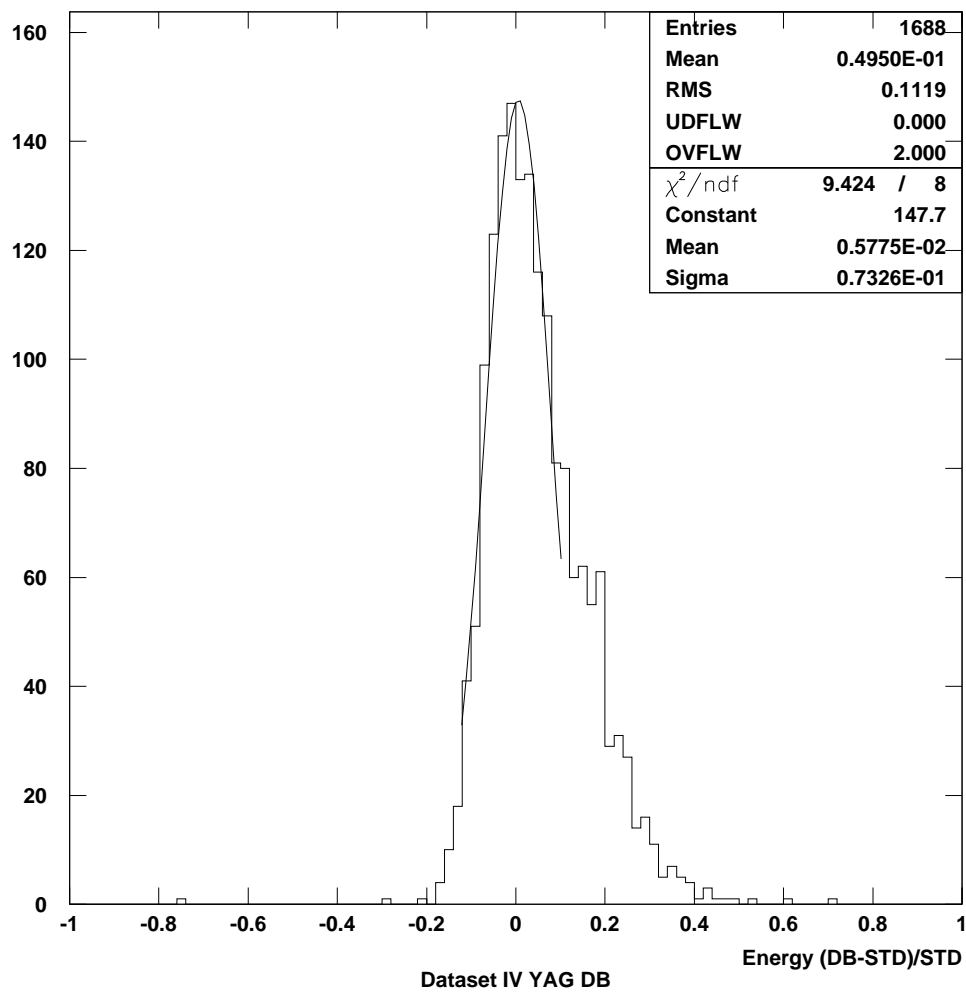


Figure 6.10: Shift in Energy by applying YAG database

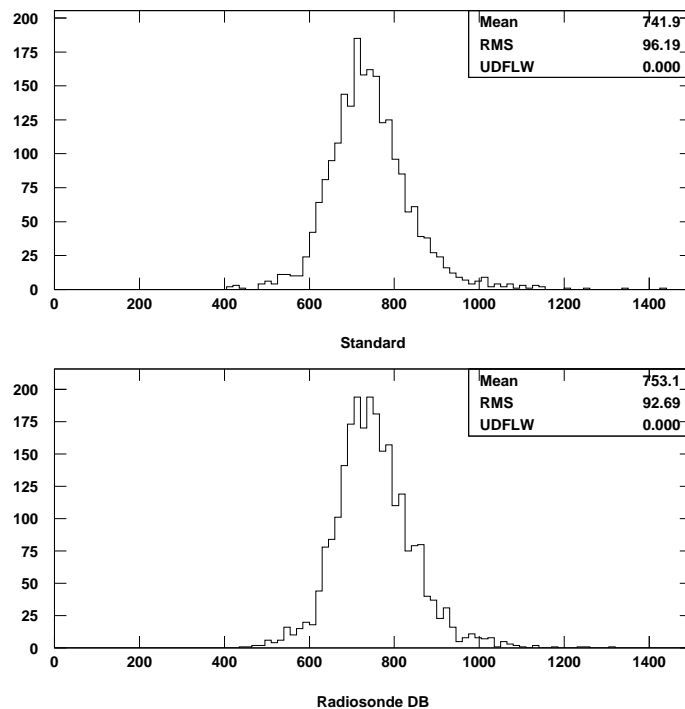


Figure 6.11: Shift in X_{max} by applying Radiosonde Database.

readily available to the general public and has been added to our analysis. Instead of using an average atmospheric model [40] we are able to know the atmospheric conditions at several heights in the surrounding area. This does not significantly effect the energy measurement but does show a systematic $10g/cm^2$ shift in the depth of X_{max} seen in figure 6.11. Figure 6.12 shows the result of applying this database to the data. A -1% shift in energy with a 2% wifth is seen.

6.6 Mirror Reflectivity

The current spectrum uses an average mirror reflectivity measurement. The reflectivity is in fact time and wavelength dependent and varies from mirror to mirror. Using data collected by Stan Thomas at Utah, using a custom built reflectometer, Professor Thomson calculated averages for each mirror and a wavelength dependence [57]. This has been added to the Monte

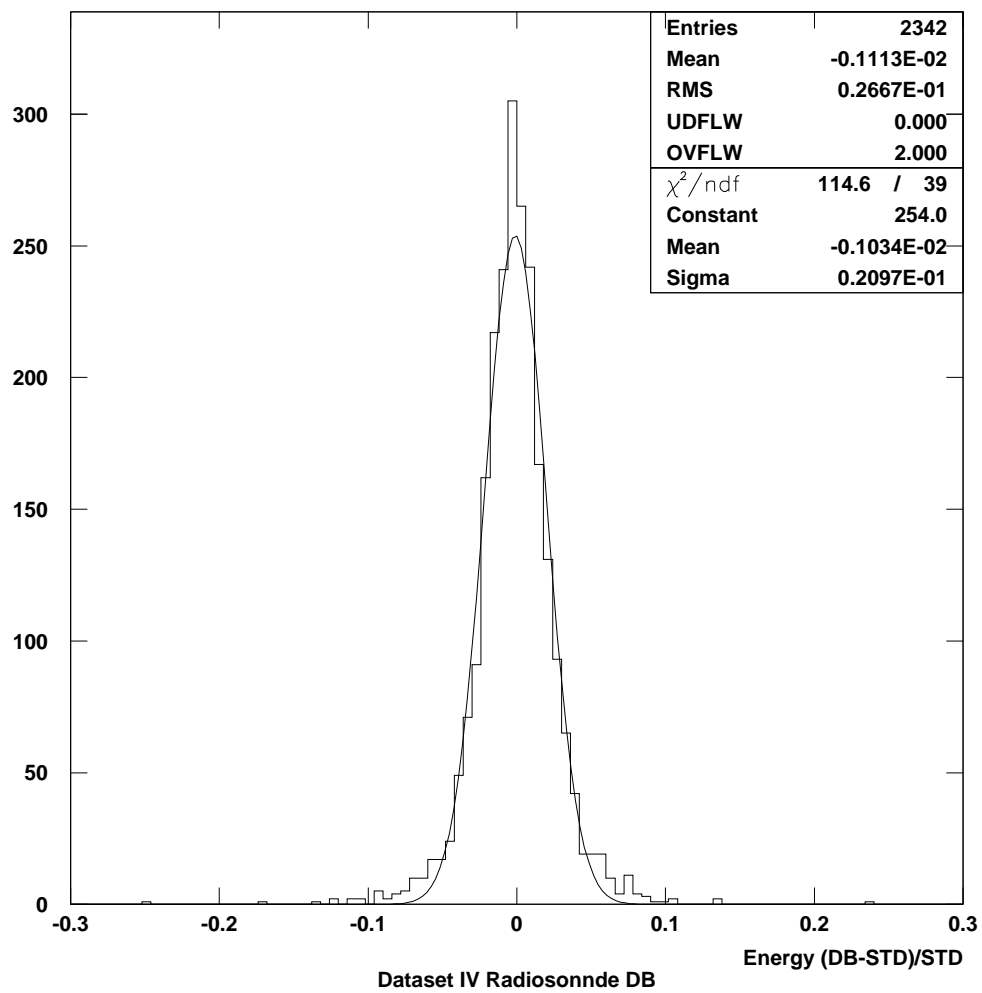


Figure 6.12: Shift in Energy by applying Radiosonde Database.

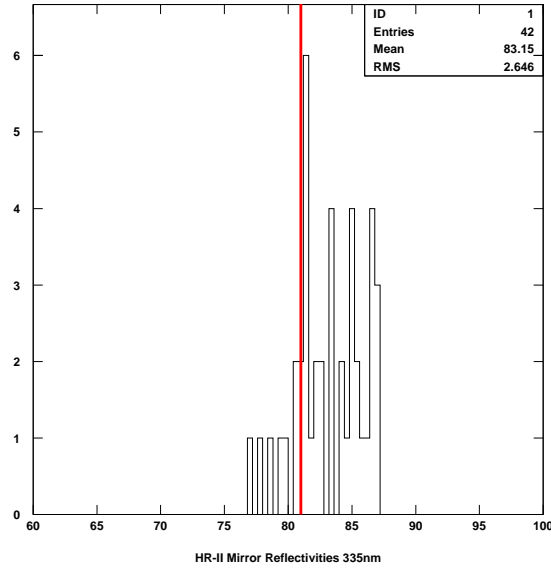


Figure 6.13: Average reflectivity of the HiRes-II Mirrors

Carlo and the reconstruction software. Figure 6.13 shows the average measurement for all 42 mirrors where the red line represents the standard analysis value of 81%. The average is 83.15%, 2% higher than the mean used previously. We therefore expect the reconstructed energy to fall by the same amount. In figure 6.14 we see the wavelength dependence of the reflectivity. When this is also added the 2% is canceled out and the overall change is found to be 0.3% with a width of 2%. This can be seen in figure 6.15.

6.7 Shower Energy Loss

The Calorimetric Energy (E_{cal}) of an Extended Air Shower (EAS) can be calculated using equation 6.8

$$\begin{aligned}
 E_{cal} &= \int_0^3 \left[\int_0^{E_{max}} N(E, s) \frac{dE}{dX}(E, s) dE \right] ds \\
 &= \int_0^3 \left[\int_0^{E_{th}} N(E, s) \frac{dE}{dX}(E, s) dE + \int_{E_{th}}^{E_{max}} N(E, s) \frac{dE}{dX}(E, s) dE \right] ds \quad (6.8)
 \end{aligned}$$

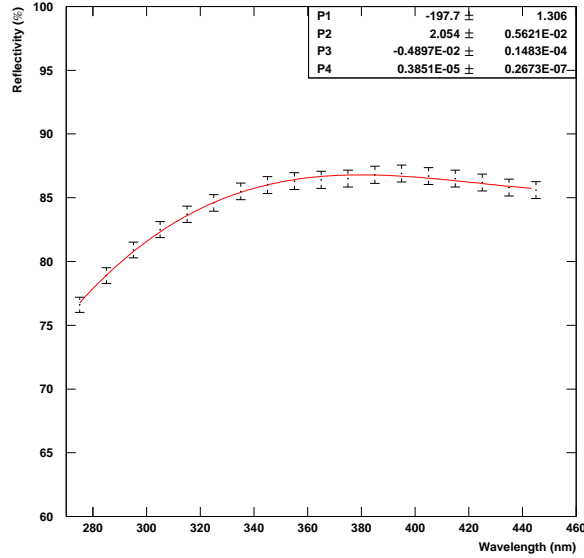


Figure 6.14: Wavelength dependence of a HiRes-II mirror

where $N(E,s)$ is the number of electrons at a shower age s with and energy E . $\frac{dE}{dX}(E, s)$ the energy loss of an electron in air at energy E per gram.

The average energy lost by a shower at a given at an age s is calculated by Song et al. [50] using equation 6.9. Note that the integrals range from E_{th} to E_{max} , where E_{th} is the energy threshold set when generating a shower in CORSIKA. It was later calculated by Andreas Zech that the energy below this threshold was 10% of the total for $E_{th} = 500\text{KeV}$. To compensated for this the HiRes-II shower library N_{max} is boosted by 10%, generating the extra fluorescence light required.

$$\frac{dE}{dX}(s) = \frac{\int_{E_{th}}^{E_{max}} N(E, s) \frac{dE}{dX}(E) dE}{\int_{E_{th}}^{E_{max}} N(E, s) dE} \quad (6.9)$$

Applying $\frac{dE}{dX}$ in the Analysis

In our detector Monte Carlo simulations the FADC signal from a shower segment of length dX at a density ρ containing N particles is calculated from equation 6.10. Where A_R and A_{mie}

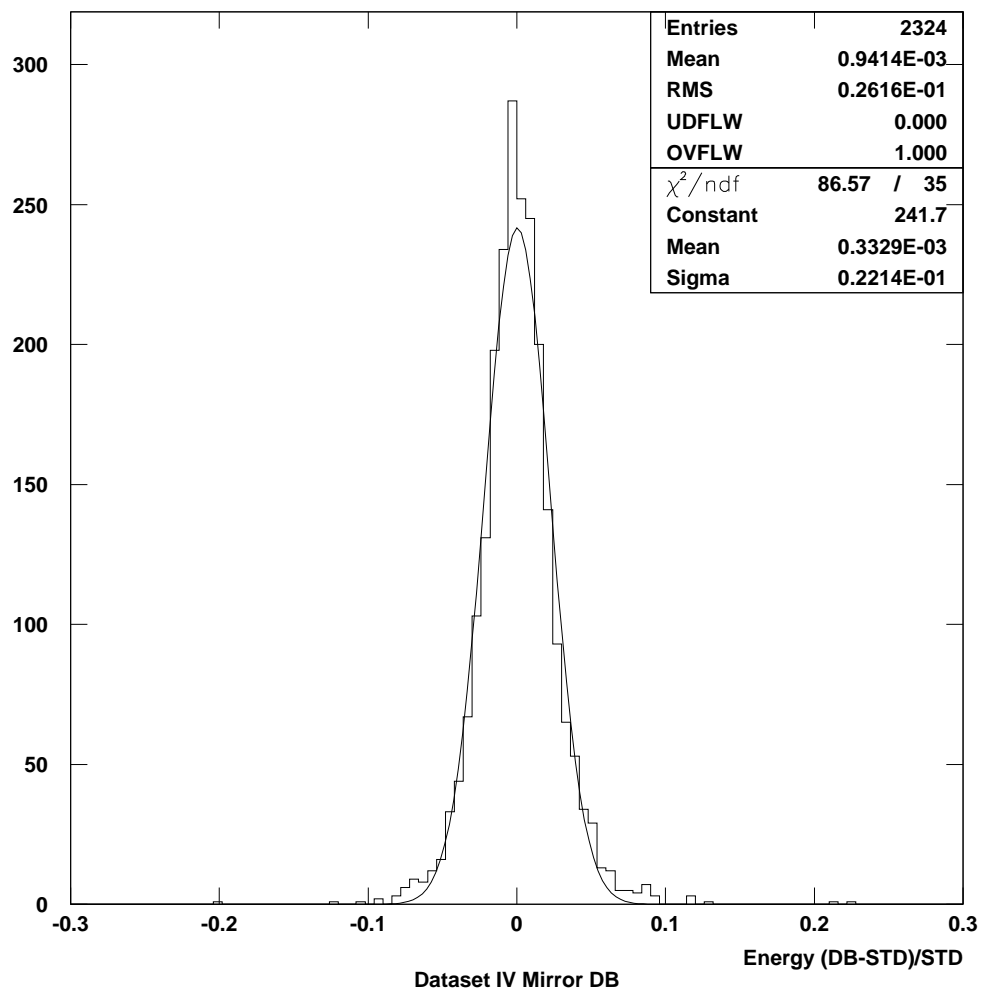


Figure 6.15: Shift in Energy by applying Mirror Database and Wavelength Dependence.

are the transmission fraction from Rayleigh and Mie scattering and Q and G are the quantum efficiency and Gain. Ω is the the opening angle to the tube.

$$FADC = N \frac{dE}{dX}(s) \frac{FLY}{\frac{dE}{dX}} \frac{dX}{\rho} \Omega A_{mie} A_R QG = N \frac{dE}{dX}(s) \Theta \quad (6.10)$$

While in the analysis we use the FADC information to calculate a number of charged particles, N.

$$N = \frac{FADC}{\left[\frac{dE}{dX}(s)\Theta\right]} \quad (6.11)$$

By integrating along the shower profile and multiplying by mean energy loss, $\langle \frac{dE}{dX} \rangle$, we find the calometric energy.

$$E_{cal} = \langle \frac{dE}{dX} \rangle \int N(X) dX \quad (6.12)$$

$$\langle \frac{dE}{dX} \rangle |_{Song} = 2.2 MeV/g/cm^2 \quad (6.13)$$

Nerling and $\alpha_{eff}(s)$

In the paper by Nerling et al. [58] an alternate method of calculating $\frac{dE}{dX}(s)$ is proposed. Using CORSIKA the number of charged particles as a function of depth and the energy loss at each step are found. From this the function $\alpha_{eff}(s)$ is found using equation 6.14. In order to speed up CORSIKA simulation a minimum threshold for particles may be specified, E_{th} . Below this energy CORSIKA stops following the particles. Changing E_{th} alters the shape of $\alpha_{eff}(s)$. The ideal of course is not to have any threshold cut. Nerling provides a way of translating an $\alpha_{eff}(s)$ calculated from a shower library, generated with an E_{th} , to one with none.

$$\alpha_{eff}(X, E > E_{th}) = \frac{1}{N_{ch}(E > E_{th})} \frac{dE}{dX}(X) \quad (6.14)$$

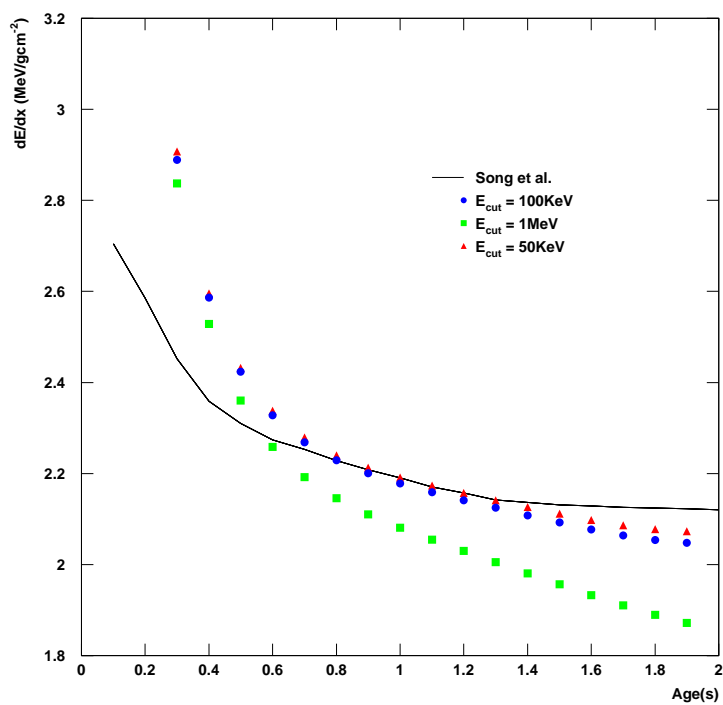
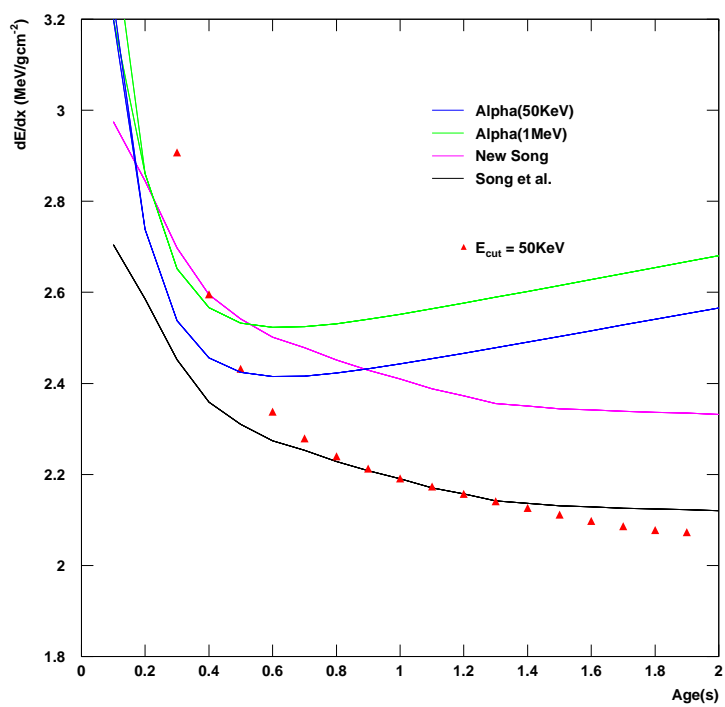


Figure 6.16: $\frac{dE}{dx}(s)$ for a given age, s. Points are calculated using f_e from Nerling et al. The line comes from Song et al.

Figure 6.17: Comparison of Nerling's α and Song et al.

Calculating α_{eff} from CORSIKA

To use the Nerling method we needed to determine $\alpha_{eff}(s)$ for our current shower library, as running large CORSIKA jobs to create a shower library are time consuming. A 10^{20} eV shower can take weeks to generate. The HiRes showers were generated using 100KeV electron, positron and gamma thresholds and 300MeV hadron 700MeV muon thresholds. The large hadron and muon threshold are a problem and required correcting for, as too much energy was being deposited at the top of the shower as the simulation stop following these particles. To do this ten showers were generated at 10^{16} eV using hadron and muon threshold cuts of 300MeV and 700MeV and 10 with 50MeV 50MeV. All other input were held constant including the random seeds. Table 6.4 shows the input card for the CORSIKA runs. The hadronic interaction model used was QGSJET01 with a thinning of 10^{-5} , the step size is $20g/cm^2$ and the $E_{th}^{e/\gamma}$ was set to 0.1MeV.

The results of the runs can be seen in figure 6.18. If the thresholds are higher the energy is deposited earlier in the shower. Therefore α_{eff} is higher at low Age. The lower threshold showers match Nerling in their shape but not normalization, which is 2% higher. When throwing the Monte Carlo we have to apply the α_{eff} derived from the showerlibrary used. In the reconstruction of the data and the Monte Carlo we should use the α_{eff} that best approximates true showers. This corresponds to the lower threshold cuts.

$$N_{ch}^{(50,50)} \approx N_{ch}^{(300,700)} \frac{\alpha_{eff}^{(300,700)}}{\alpha_{eff}^{(50,50)}} \quad (6.15)$$

From figure 6.7 we see the $\langle \frac{dE}{dX} \rangle$ is $2.52MeV/g/cm^{-2}$, 10% higher than the current HiRes standard. We therefore expect the energy to change by -10%. This is seen in figure 6.20.

6.8 Input Spectrum and the G.Z.K. Cutoff

When our detector Monte Carlo is thrown we do not include the GZK cutoff. The unfolded real spectrum approaches reality if the inputs to our simulations are as accurate as possible.

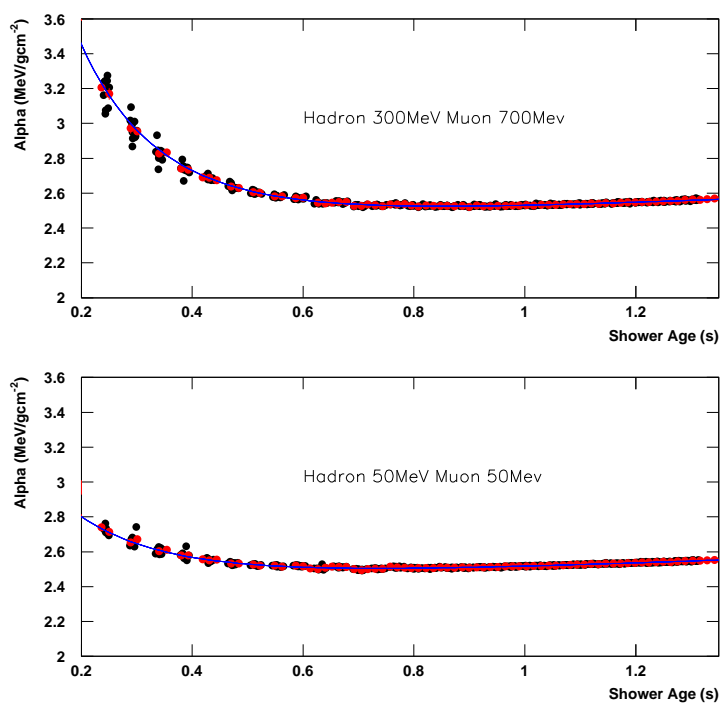


Figure 6.18: α_{eff} *black*: Individual showers. *Red*: Average. *Blue*: Fit using Nerling parametrization

RUNNR	63840	run number
EVTNR	1	number of first shower event
NSHOW	1	number of showers to generate
PRMPAR	14	particle type of prim. particle
ESLOPE	0.0	slope of primary energy spectrum
ERANGE	1.E7 1.E7	energy range of primary particle
THETAP	38.0 38.0	range of zenith angle (degree)
PHIP	0. 360.	range of azimuth angle (degree)
SEED	7 0 0	seed for 1. random number sequence
SEED	0 0 0	seed for 2. random number sequence
OBSLEV	1500.E2	observation level (in cm)
FIXHEI	0. 0	first interaction height and target
FIXCHI	0.	starting altitude (g/cm^2)
MAGNET	21.93 48.26	magnetic field: Dugway
HADFLG	0 0 0 0 2	flags hadr.interact.and fragmentation
ECUTS	XXXX XXXX 0.0001 0.0001	energy cuts for particles
MUADDI	T	additional info for muons
MUMULT	T	muon multiple scattering angle
ELMFLG	T T	em. interaction flags (NKG,EGS)
STEPFC	1.0	mult. scattering step length fact.
RADNKG	200.E2	outer radius for NKG lat.dens.distr.
ARRANG	0.	rotation of array to north
LONGI	T 20.0 T T	longit.distr. and step size and fit and out
ECTMAP	1.E3	cut on gamma factor for printout
MAXPRT	100	max. number of printed events
DIRECT	/cosmic8/gahughes/showerlib/	output directory
DATBAS	F	write .dbase file
USER	GH	user
DEBUG	F 6 F 1000000	debug flag and log.unit for out
THIN	1.E-5 1.E1 0.	thinig parameters
EXIT		terminates input

Table 6.4: CORSIKA Input card for this analysis

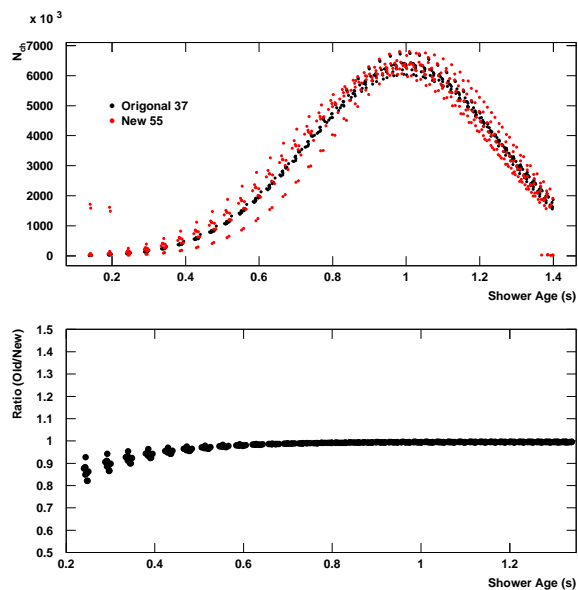


Figure 6.19: Shows the original shower(red) thrown with (300,700) and the calculated shower(black) using equation 6.15

Therefore we are introducing a bias by not including a cutoff. It is however necessary to do this in order prove the existence of the cutoff.

Throwing Monte Carlo with such a hard cutoff to obtain a large statistics sample is extremely time consuming. To avoid this I took the existing Monte Carlo and re weighted it using the spectrum with a cutoff. Figure 6.21 shows the aperture determined with and without the cutoff. The ratio of the two is seen in the lower panel. At $10^{19.75}$ eV we see a break in the ratio. This represents the amount by which the flux should be suppressed in our spectrum above the cutoff. By including this effect the break in spectrum would have a more significant cutoff.

6.9 Total Systematic Shift

By combining all the effects described we find a total systematic shift of -11.8% with a width of 8%. Several of the effects have shift that interact with each other and so the final shift is not a linear addition of the described effects.

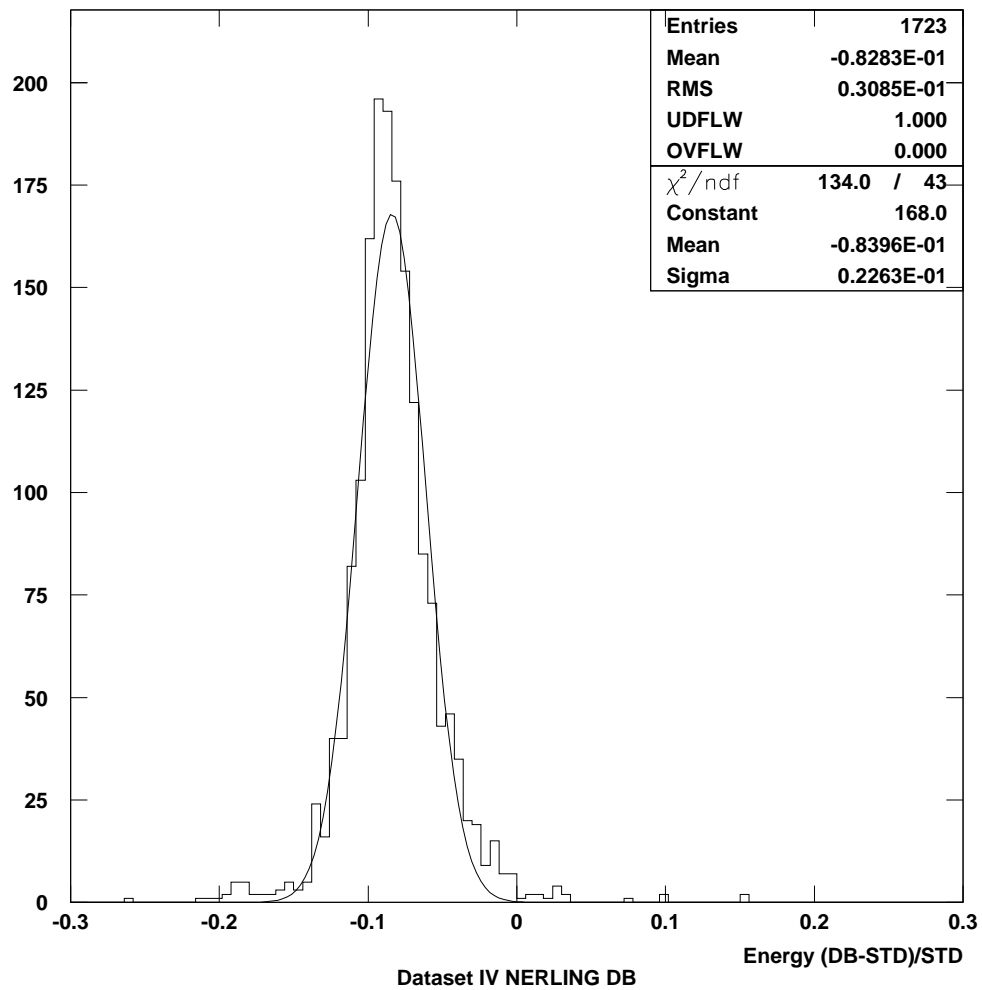


Figure 6.20: Shift in Energy by applying Nerling $\frac{dE}{dX}$

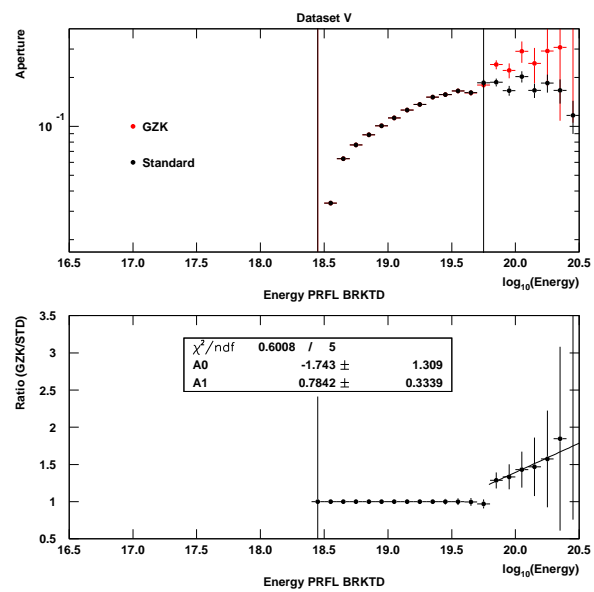


Figure 6.21: Effect of adding cutoff to the Input Spectrum.

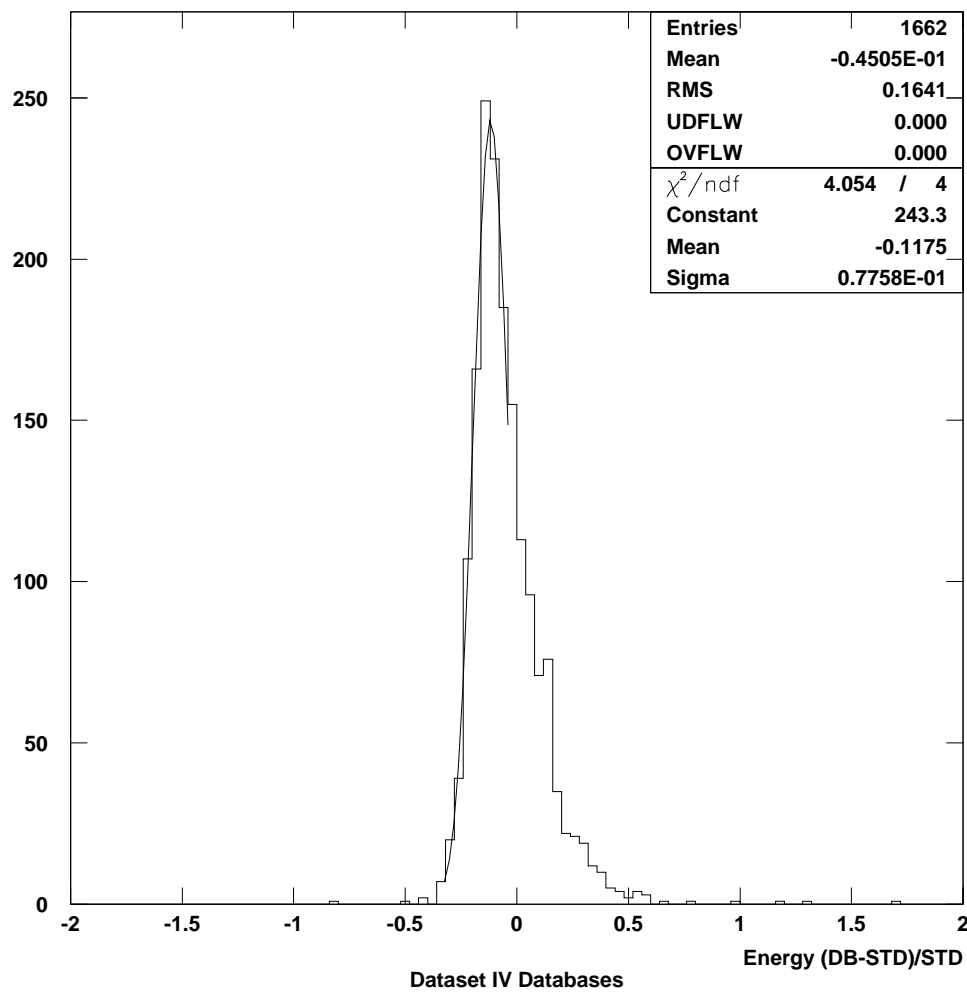


Figure 6.22: Shift in Energy by Applying All Effects.

Chapter 7

Average Longitudinal Shower Profile

7.1 Gaisser-Hillas Profile

In 1941 Rossi and Greisen published a review paper on Cosmic Ray theory [59]. In it they give mathematical descriptions of the number of charged particles as a function of shower age. These showers are purely electromagnetic and are derived by considering bremsstrahlung and pair-production processes. This however does not reflect the reality of hadron initiated CR showers. They are initiated by charged particles or nuclei and have a core hadronic component that feeds the rest of the shower. In 1977 Gaisser and Hillas used the Greisen formula as a basis to derive the Gaisser-Hillas Equation [60] which is shown below.

$$N(X) = N_{max} \left(\frac{X - X_0}{X_{max} - X_0} \right)^{\frac{(X_{max} - X_0)}{\lambda}} e^{-\frac{(X_{max} - X)}{\lambda}} \quad (7.1)$$

It describes the number of charged particles as a function of slant depth $X(g/cm^2)$ with four free parameters. X_0 is the depth of first interaction, N_{max} the number of charged particles at X_{max} which is the depth at which the shower reaches it's maximum. λ is the elongation parameter and controls the width of the shower. Figure 7.1 shows a typical shower fit to equation 7.1. This result has only been checked once by the HiRes prototype detector and in Monte Carlo studies [61, 62]. Using the full HiRes-II detector we are able to reach 100 orders of magnitude higher in energy and with greater statistics. Showers at these energies are rare and should be studied extensively.

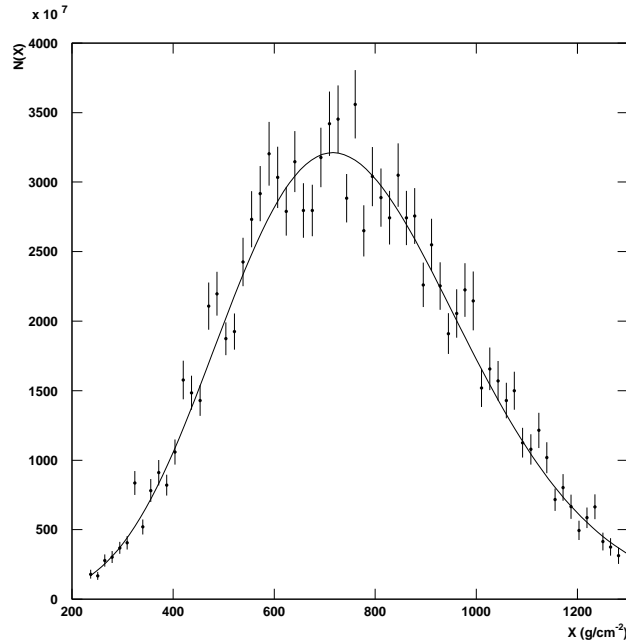


Figure 7.1: Typical Air Shower as measured by HiRes-II. Fit to equation 7.1

7.2 Normalization of Air Shower Profiles

Our data sample varies over 3 orders of magnitude in energy and therefore the parameters change greatly. N_{max} has a range of 10^3 and X_{max} can be found anywhere from $300g/cm^2$ to $1200g/cm^2$. For all the showers to be averaged we must find a suitable way to scale them.

The profiles are read from the RUPRFL Bank, which stores the number of charged particles as a function of slant depth. Each profile is locally fitted around its peak to a Gaussian function in order to determine N_{max} and X_{max} . The showers are normalized by their respective shower maximum to get $n(s)$, as shown in figure 7.2. All showers are set equal to unity at their shower maximum. The position of shower maximum is proportional to the $\log(E_o)$, where E_o is the primary particle energy. Longitudinal development of showers can be standardized using “shower age”, defined in equation 7.3.

$$n(s) = \frac{N(s)}{N_{max}} \quad (7.2)$$

$$s = \frac{3X}{X + 2X_{max}} \quad (7.3)$$

The development phase of the shower lies between $s = 0$ and 1. X_{max} is found at $s = 1$ and the decay phase is in the range 1 to 3. Experimentally a shower has a range of 0 to 2. Applying this to a single shower gives the result seen in figure 7.2. The results from many showers can be averaged in bins of age giving the Average Longitudinal Shower Profile. Great care was taken in this process, where each bin in age was fit to a Gaussian to find the mean and error. This same technique is applied to Monte Carlo.

As shown in [61] the Gaisser-Hillas equation 7.1 can be written as follows

$$n(s) = \left(1 - \frac{(1-s)}{(3-s)} \frac{3T_{max}}{(T_{max} - T_o)}\right)^{T_{max}-T_o} e^{(3T_{max} \frac{1-s}{3-s})} \quad (7.4)$$

where $T_{max} = X_{max}/\lambda$ and $T_o = X_o/\lambda$ are the two remaining parameters. T_o is constrained to be less than $\frac{2s_{min}}{2-s_{min}}T_{max}$, where s_{min} is the lower limit of the data points, approximately 0.4. Another parametrization, with only one free parameter (σ), is the Gaussian in age

$$f(s) = \exp\left(\frac{-1}{2\sigma^2}(s-1)^2\right) \quad (7.5)$$

As these showers have been fully reconstructed the energy is known. We split the data into energy bins and study their properties as a function of these bins. We can also apply the hourly atmospheric database instead of average atmospheric conditions, as this will have an effect on the shower shape. Monte Carlo can also be generated using the database and reconstructed in the same way. In order to study potential reconstruction biases we can analyze the Monte Carlo using the exact thrown geometry. Pure proton and Iron samples can also be generated. This is interesting as we know that shower shapes are effected by the mass of the primary cosmic ray.

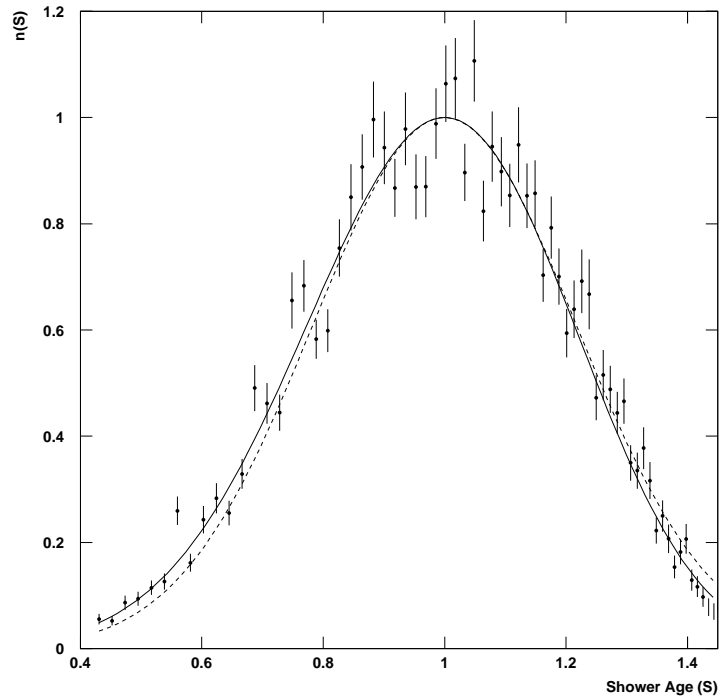


Figure 7.2: Typical Normalized Air Shower as measured by HiRes-II. Fit to equation 7.4 - *solid line* and equation 7.5 - *Dashed line*

7.3 Experiment and Data Set

Work presented comes from data taken in the period from 2002 to 2006 measured by the HiRes-II in monocular mode. To ensure that the events selected were of good quality each was required to have a track length greater than $500g/cm^2$. X_{max} must be visible $50g/cm^2$ after the beginning of the observed part of the shower and $50g/cm^2$ before its end. To minimize the amount of possible Cerenkov light ψ cannot be more than 110° . These cuts are summarized in table 7.1. A total of 11655 data events and 35966 Monte Carlo events were selected.

7.4 Average Showers

When fitting the average showers care was taken to avoid biased data at extremes in age. Using the Monte Carlo we can reconstruct simulated data with no error in ψ . Reconstruction of the shower in monocular mode can be effected by ψ resolution. When standard Monte Carlo

Cuts	
Selected tubes	≥ 6
Photo-electrons/degree	$> 25.$
Track length	$> 7^\circ$
Zenith angle	$< 80^\circ$
Average Cerenkov Correction	< 0.70
Geometry fit $\chi^2/\text{d.o.f.}$	$< 10.$
Profile fit $\chi^2/\text{d.o.f.}$	$< 10.$
X_{max}	$\pm 50g/cm^2$ of seen shower
Tracklength	$> 500g/cm^2$

Table 7.1: Cuts Used in this analysis.

is compared with Monte Carlo reconstructed using the thrown ψ we found a deviation in the average showers at low (~ 0.7) and high (~ 1.3) age. These areas were avoided when making fits to the average shower. Figure 7.3 shows the Monte Carlo average shower in the energy range $10^{17.50}\text{eV}$ to $10^{18.0}\text{eV}$. Black data points are using the standard reconstruction and blue correspond to showers reconstructed using the thrown value of ψ . The lower panel is the ratio of the two. This is done in all energy ranges giving the age range for which any fit is valid.

We also have a composition bias at low age and energy due to the tops of the HiRes mirrors at 31° . No similar bias is seen at high age and energy.

Figure 7.4 and 7.5 show fits to the average shower to the normalized Gaisser-Hillas and Gaussian equations 7.4 and 7.5. They are both for the energy ranges $10^{19.0}$ to $10^{19.5}\text{eV}$. The blue dots are the individual measurement from the showers. Black points show the averages and the line the respective fits. The lower panel shows the residuals.

In order to parametrize the average shower as a function of energy we chose the Gaussian as it only has one degree of freedom. Fitting the average shower to find it's width in half decade energy bins from the standard HiRes Monte Carlo and a pure Iron and Proton sample we find the results seen in figure 7.6. Standard Monte Carlo is thrown with an average 80% proton fraction. The first bin shows the average shower for all energies. The Monte Carlo lies 80% of the way between the pure Proton and Iron points and follows this trend in all the energy bins.

To find an estimate of the errors I used a bootstrap method. Taking the set of individual

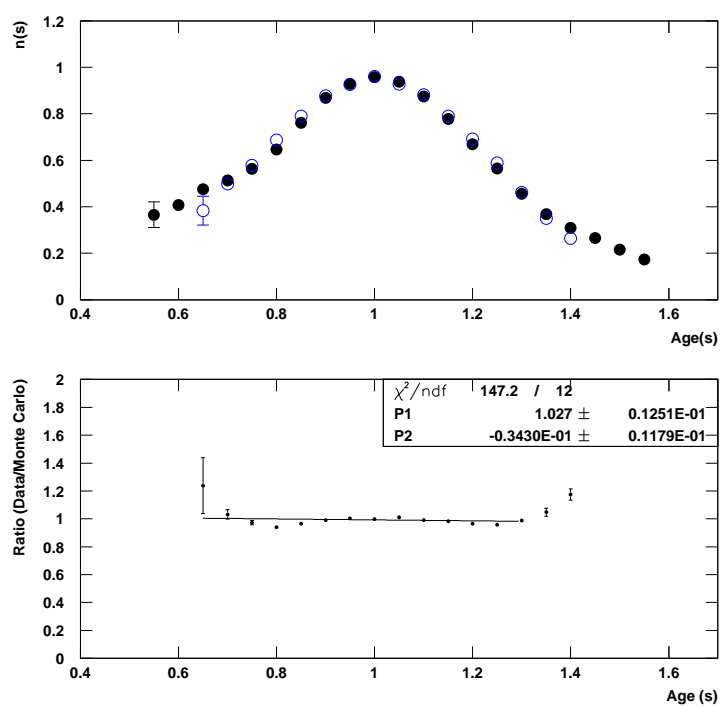


Figure 7.3: Comparison of the same Monte Carlo set analyzed using reconstructed and true values of ψ . Black reconstructed ψ and blue thrown ψ

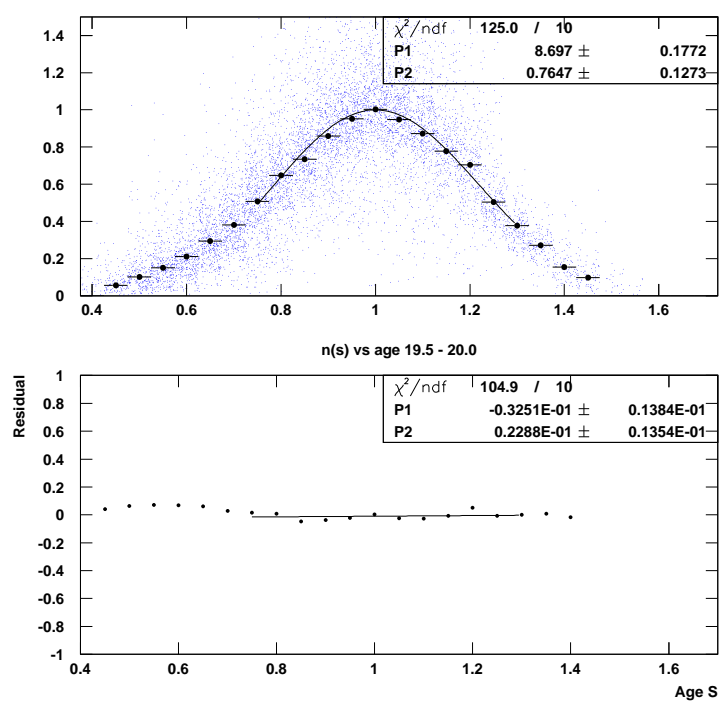


Figure 7.4: Average Shower from the data in the energy range $10^{19.0}$ to $10^{19.5}$ eV. Blue marks are the original showers. Black marks the average. The line is a fit to equation 7.4. Lower panel shows the residuals.

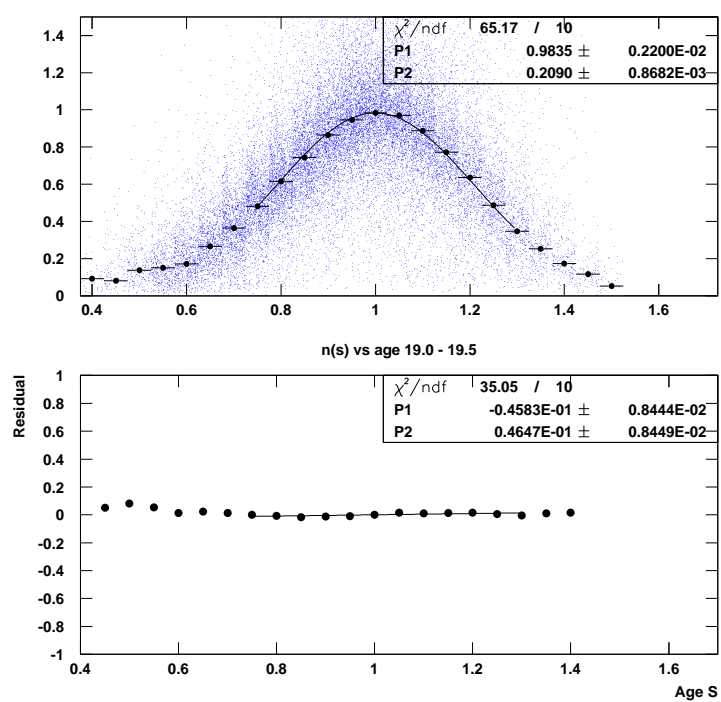


Figure 7.5: Average Shower from the data in the energy range $10^{19.0}$ to $10^{19.5}$ eV. Blue marks are the original showers. Black marks the average. The line is a fit to equation 7.5. Lower panel shows the residuals.

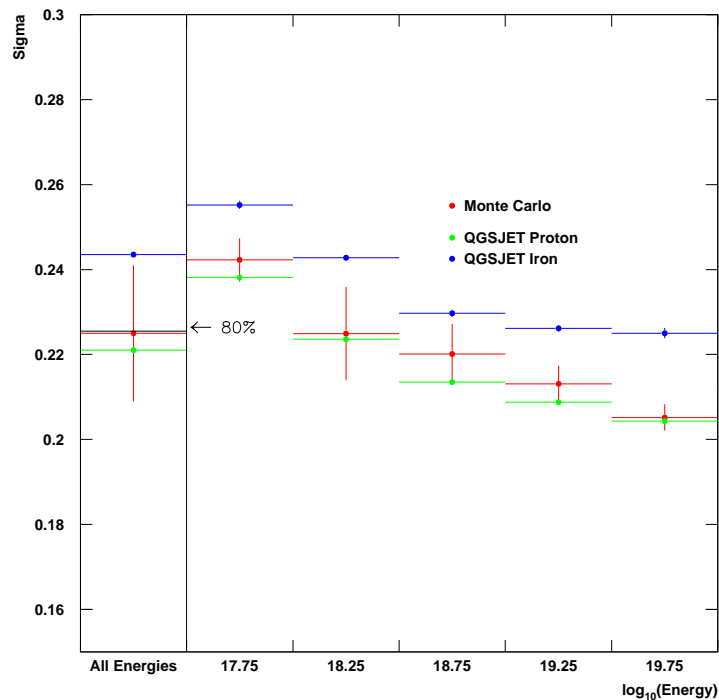


Figure 7.6: Average Shower width as a function of energy. Red: Standard Monte Carlo, Blue: Pure Iron Monte Carlo and Green: Pure Proton Monte Carlo.

showers 100 further sets were created using replacement. These were then re-averaged and fit again to find a distribution of σ 's. The width of this distribution is the new error.

A comparison with the widths of the data and Monte Carlo can be seen in figure 7.7. It shows good agreement across all energies except the final half decade. Here we see a 2.5σ difference. The Monte Carlo is thrown using the CORSIKA shower library described in chapter 3. These showers are fit to the Gaisser-Hillas function. Figure 7.7 suggests that the showers agree well with the Gaisser-Hillas. When we analyze the data and Monte Carlo with the atmospheric database we see a similar result, shown in figure 7.8. Finally we can look at the effect of analyzing the Monte Carlo using the reconstructed and true value of ψ . Figure 7.9 shows how the resolution in due to ψ increases the average width by a constant amount of approximately 0.01σ .

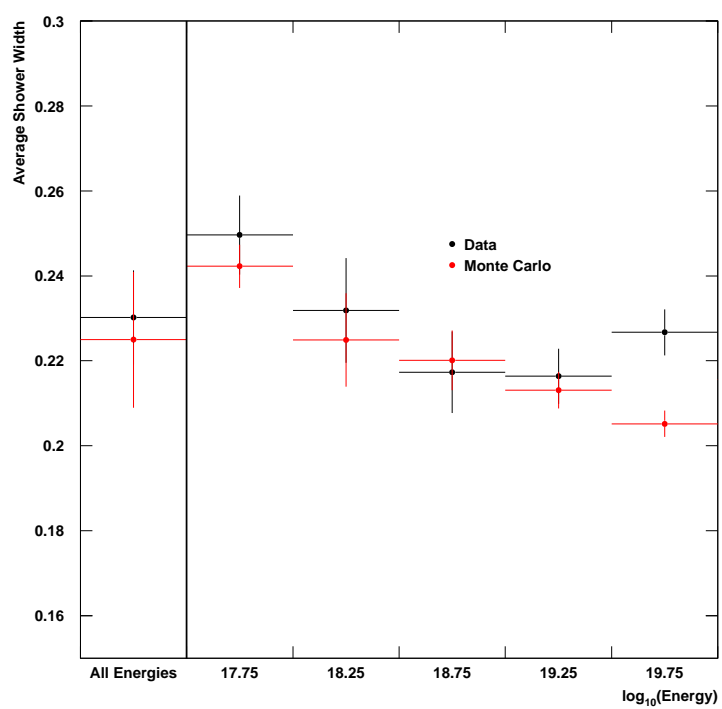


Figure 7.7: Average Shower width as a function of energy. Red: Standard Monte Carlo and Black: Data.

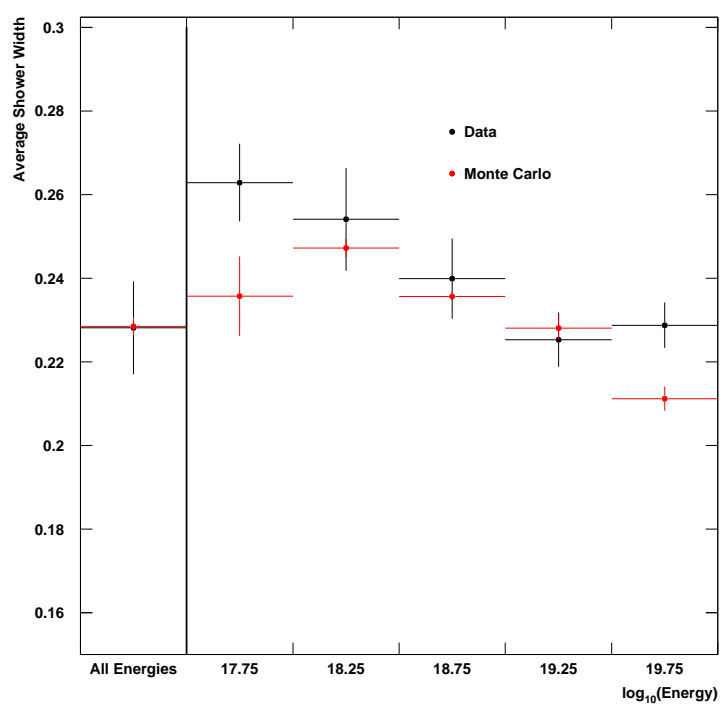


Figure 7.8: Average Shower width as a function of energy using the atmospheric database.

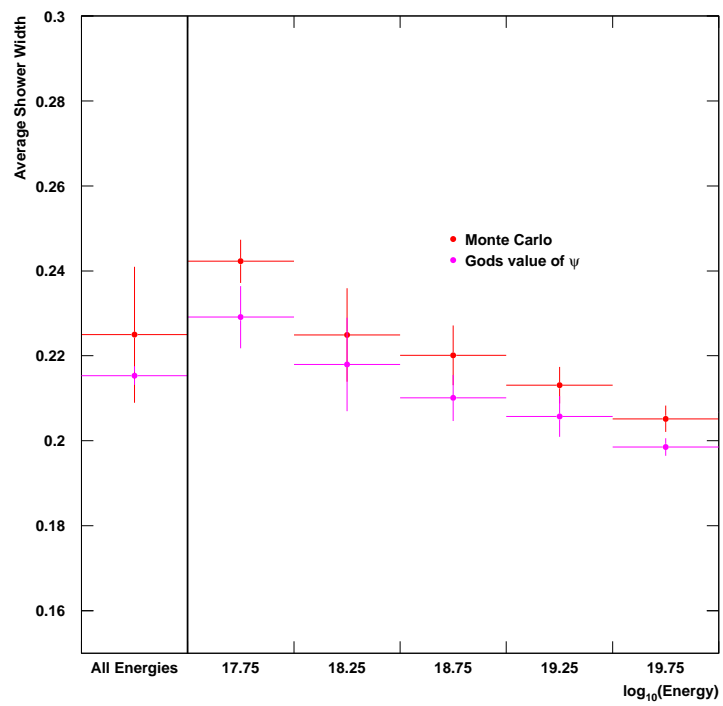
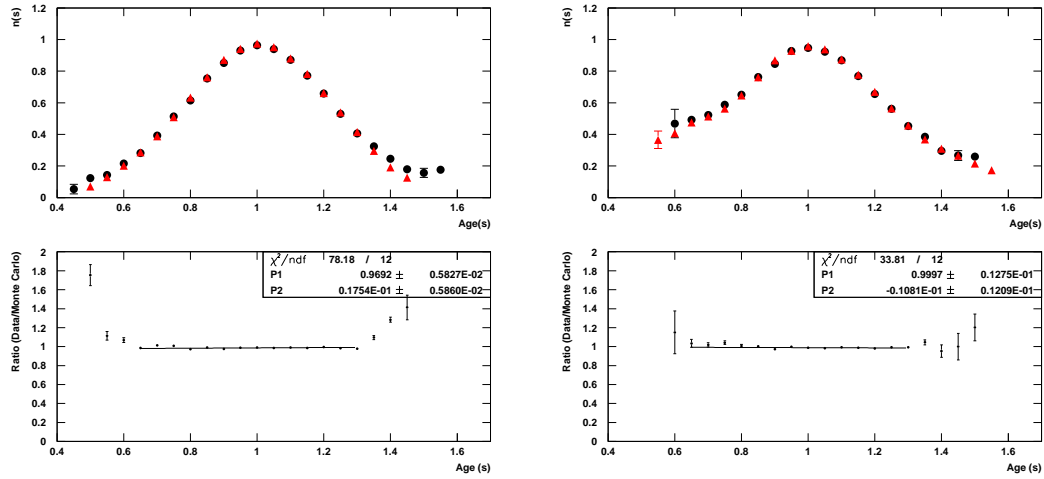


Figure 7.9: Average Shower width as a function of energy. Red: Standard Monte Carlo and Purple: Monte Carlo using reconstructed using thrown ψ .



(a) Data - Monte Carlo Comparison. Black: Data, Red: Monte Carlo. In the energy range $10^{17.5}$ to $0^{20.0}$. (b) Data - Monte Carlo Comparison. Black: Data, Red: Monte Carlo. In the energy range $10^{17.5}$ to $0^{18.0}$.

Figure 7.10

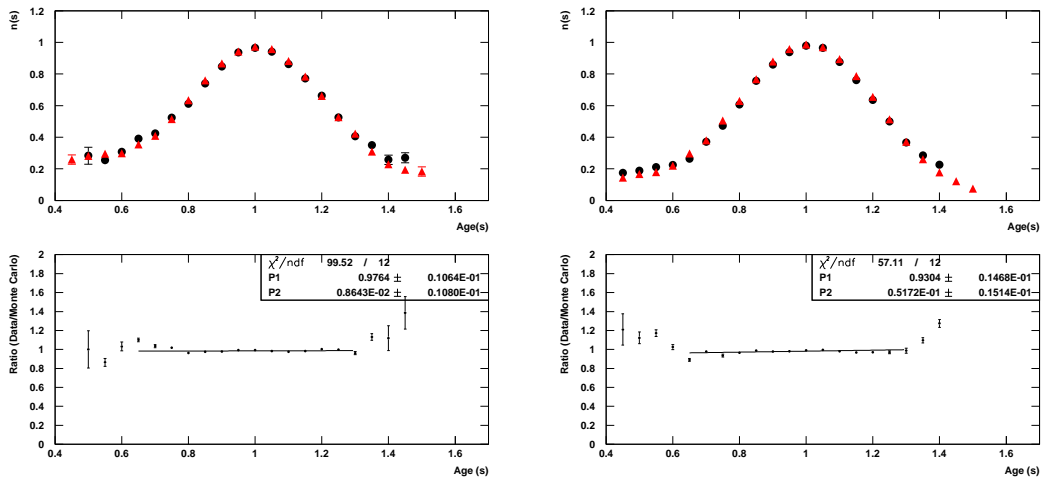
7.5 Data - Monte Carlo Comparisons

Data and Monte Carlo are split into the same half-decade bins ranging from $10^{17.5}$ to $10^{20.0}$ eV. An average profile was created for each energy bin. Figures 7.10 to 7.12 show the comparisons across all energy ranges. In the lower panel a straight line fit is made between 0.65 and 1.30 in age to the ratio of data and Monte Carlo. By using the full detector simulation we fold in all the possible biases in the data thus making the comparisons as accurate as possible. These plots show good agreement between the data and Monte Carlo.

7.6 A Reality Check

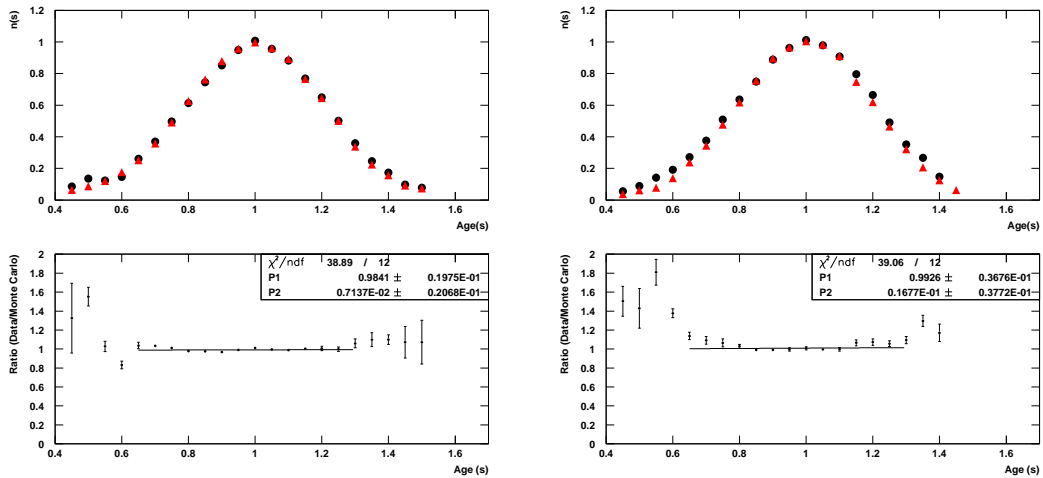
As a check to see if we understand the results I developed a separate program which generates showers with any shape to be analyzed by the same programs.

Showers were thrown with the HiRes spectrum and the showers were positioned in the sky using the known distributions from the data. Gaisser-Hillas and Gaussian showers were thrown. For each segment the number of charged particles were distributed randomly using



(a) Data - Monte Carlo Comparison. Black: Data, Red: Monte Carlo. In the energy range $10^{18.0}$ to $0^{18.5}$. (b) Data - Monte Carlo Comparison. Black: Data, Red: Monte Carlo. In the energy range $10^{18.5}$ to $0^{19.0}$.

Figure 7.11



(a) Data - Monte Carlo Comparison. Black: Data, Red: Monte Carlo. In the energy range $10^{19.0}$ to $0^{19.5}$. (b) Data - Monte Carlo Comparison. Black: Data, Red: Monte Carlo. In the energy range $10^{19.5}$ to $0^{20.0}$.

Figure 7.12

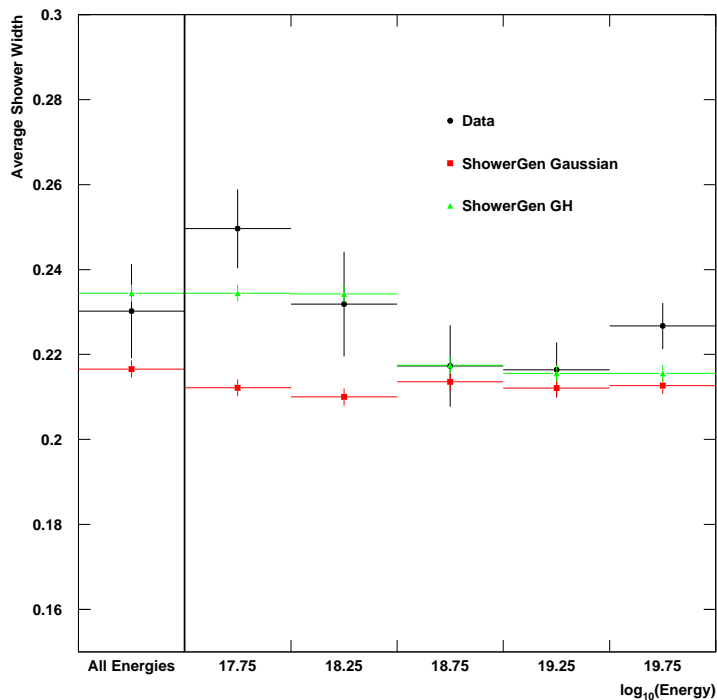


Figure 7.13: Average Shower width as a function. Black: Data, Green: Gaisser-Hillas shaped showers and Red: Gaussian shaped showers.

Poisson statistics. A similar number of showers to the data sample are generated and then ran through the same software to find the average shower. Figure 7.13 shows the result. The width of the thrown Gaussian showers was a constant 0.2σ . They are reconstructed at a constant width of $\sim 0.215\sigma$. This increase is due to resolution. The data shows better agreement with the Gaisser-Hillas generated showers.

7.7 Conclusion

Several methods were developed to find and test the properties of cosmic ray air showers. By comparing the data to theoretically predicted shapes and Monte Carlo using two different methods we find the data is well described by the Gaisser-Hillas parametrization.

Chapter 8

Telescope Array

8.1 Introduction

The Telescope Array (TA) is a collaboration including groups from Japan, the United States, Russia and Korea. Located in Millard County, Utah it is the only hybrid Ultra High Energy Cosmic Ray detector in the Northern Hemisphere [63]. Hybrid refers to the combination of Air Fluorescence and Ground Array detection methods. While having a near 100% duty cycle a ground array only samples the shower at one level. Fluorescence detectors are able to see most of the shower, giving better energy resolution, but have only a 10% duty cycle. By combining these techniques it will be possible to have a continuous energy range over 4 orders in magnitude, from $10^{17.5}$ to $10^{20.5}$ eV. Cross-calibration will be possible across the entire range helping to control systematic effects. The ground array will be 100% efficient above $10^{19.0}$ eV and the aperture is calculated to be 1500km^2 ster. Figure 8.1 shows the layout of the detector.

8.2 Ground Array

507 counters with 1.2km spacing in a square grid array were deployed in 2007. They each contain 2 layers of scintillator and two photo tubes for the detection of coincidence signals. A trigger is defined as 3 adjacent counters with 3 or more MIPS. They are solar powered where the charge is stored in a 12Volt battery. Signals from each Surface Detector (SD) are sent to one of three communication towers and then onto a central computer via microwave transmitters.

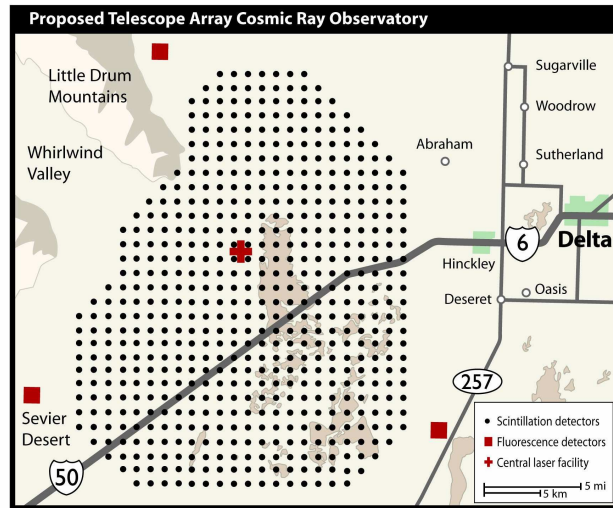


Figure 8.1: Map showing layout of Telescope Array.

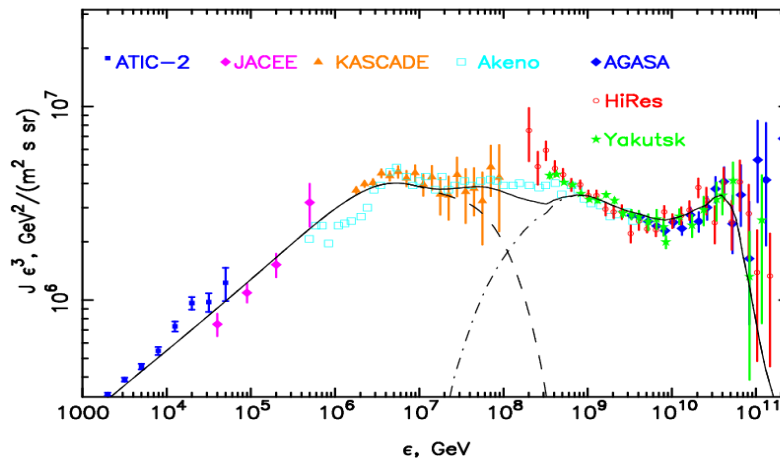


Figure 8.2: Spectrum of Cosmic Rays $\times E^3$ as a function of Energy for the Experiments Shown. [8]

8.3 Fluorescence Detectors

Telescope Array is surrounded by 3 fluorescence detectors. Two are Flash ADC detectors constructed by the Japanese side of the collaboration, sited at Black Rock Mesa and Long Ridge. The third, Middle Drum, has been constructed by the US contingent (Utah and Rutgers). Black Rock Mesa and Long Ridge consists of 12 cameras while Middle has 14 all of the sites have a 120 degree wide field of view. Two rings of mirrors see from 3 to 32 degrees in elevation. Much of the Middle Drum FD, including mirrors and electronics, were taken from the HiRes experiment.

8.4 Telescope Array Low Energy Extension (TALE)

A major part of Telescope Array will be its Low Energy Extension. The aim will be to measure the flux and composition of the primary Cosmic Rays from $10^{16.5}$ to $10^{19.0}$ eV using a variety of techniques. An extra fluorescence detector will be placed 6km from the Long Ridge FD looking across an infill array of scintillation counters and muon detectors. The FD will have an aperture $10\times$ that of HiRes. A key instrument will be the Tower Detector. It will be a fluorescence detector with mirrors 3 times the area of HiRes mirrors looking up to 72 degrees in elevation. Larger mirrors will be able to collect more light lowering the threshold of the experiment, while a higher elevation will increase the aperture for lower energy CRs that do not penetrate as deeply into the atmosphere.

During the summer of 2007 a prototype tower detector was constructed and tested at HiRes-I. A single mirror, $12.2m^2$ in area, was place such that it looked over the original HiRes ring 1. This new mirror had an elevation view of 44° to 53° (ring 4). The detector was run over a 2 week period and several events were found in coincidence with ring 1.

8.5 Physics of TA and TALE

Figure 8.2 shows the spectrum of Cosmic Rays from 10^3GeV to 10^{11}GeV . At $3 \times 10^6\text{GeV}$ there is a break in the spectrum called the “Knee”. Cosmic Rays up to and just beyond this energy can be explained by Super Nova Remnants (SNR). The KASCADE experiment has not only measured the flux in this energy range but also the mass of the primary particle [11]. Results suggest that the primary particle mass increases through this region. As the acceleration of the primary is dependent on charge, Z , it implies the sources are reaching their maximum energy. The dotted line falling from this point shows the predicted flux from SNR sources [64]. Rising at the same point is a prediction for extra-galactic cosmic rays. Here we see the “Ankle” and G.Z.K. cutoff, caused by e^+e^- production and pion production via interaction with the CMB. At $5 \times 10^9\text{GeV}$ there is another break - the Second Knee, which is the least well understood part of the high energy spectrum. A few experiments have measured the cosmic ray flux near the Second Knee. The left panel of figure 8.4 shows some of these experiments and the right shows the same results with their energies adjusted as shown.

Several possibilities exist to explain the break. One possibility is the existence of another galactic component. Or it could be due to the change in evolution of extra galactic sources, that may effect the spectral shape. Both QSO’s and AGN’s show a break in their luminosity densities at a red shift of 1.6 [64]. This result predicts the correct energy dependence below the knee, suggesting they could be the source of UHECRs. Other possibilities rely on our lack of information regarding the strength of galactic magnetic fields. For a given field strength and energy, particles propagate either by diffusion or rectilinearly. Where the transition lies effects the shape and composition of the spectrum.

Figure 8.3 shows the elongation rate for several experiments and pure Monte Carlo simulations. Mean X_{max} is proportional to the log of the primary cosmic ray mass. For a pure compositions, shown as solid lines in the plot, we see a near constant gradient. A break in the slope of the data implies a change in composition. TA and TALE will be able to measure X_{max} continuously from the end of the galactic spectrum until the end of the extra-galactic.

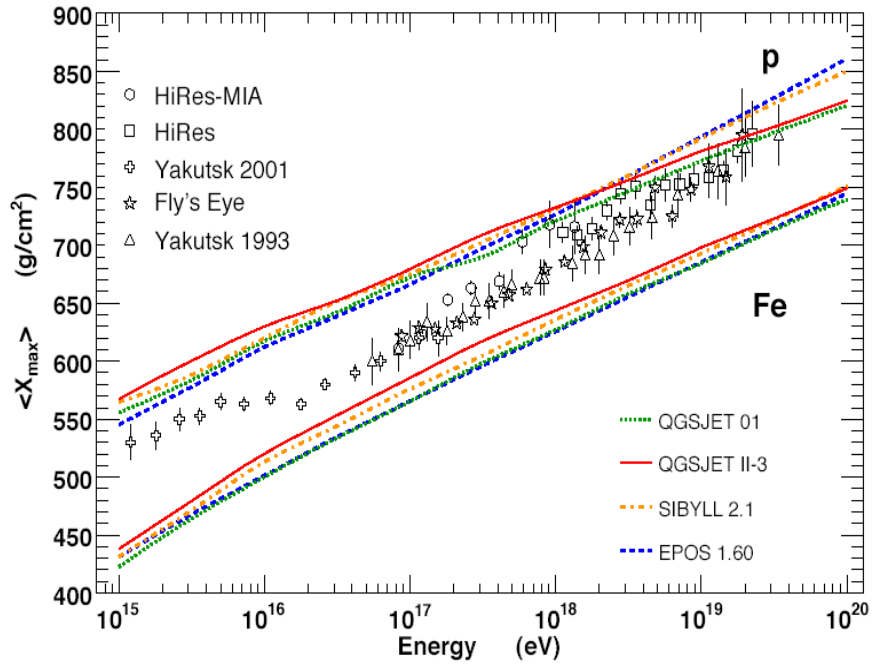


Figure 8.3: Elongation Rate, Mean X_{max} for the Experiments Shown and Pure Composition Simulations Proton and Iron for various Hadronic Interactions.

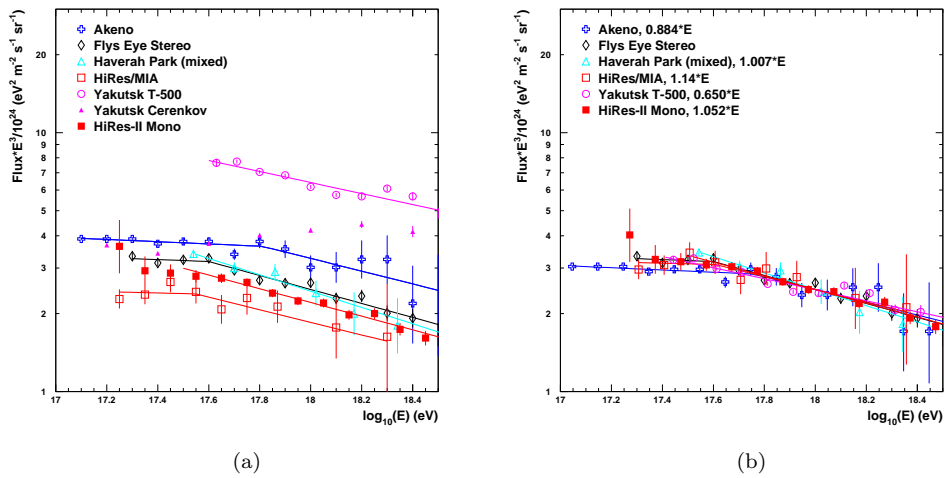


Figure 8.4: Cosmic Ray Flux for several experiments near $10^{17.5}$ eV [4]

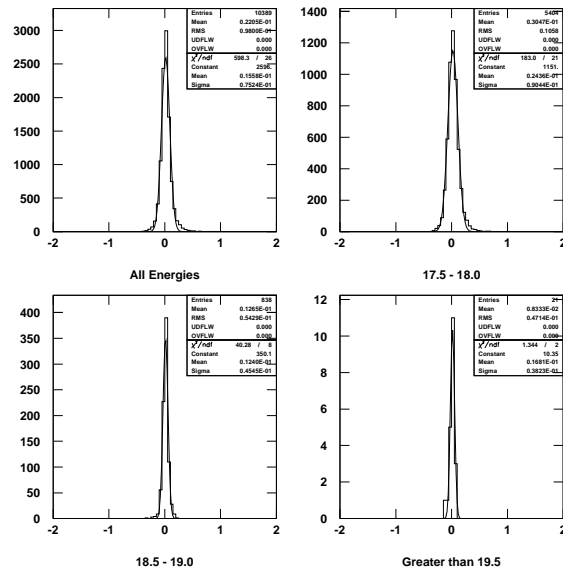


Figure 8.5: ψ resolution (degrees) for the HiRes-II detector. Labels denote $\log_{10}(\text{Energy})$

Another method of measuring composition is to measure the ratio of electron to muon density at the ground, which is employed by KASCADE. Higher mass cosmic rays give rise to more muons in the resulting shower. These are deeply penetrating and reach the ground. TALE will include an infill array of scintillators and buried scintillator, the later acting as muon detectors. By measuring the break in the spectrum and the composition simultaneously it will be possible to explain this feature.

8.6 Simulating the TALE Detector Electronics.

In monocular mode it is important to have a good reconstruction of ψ , see section 4. Figure 8.5 shows the ψ resolution (degrees) for the HiRes-II detector. As we probe lower energy showers our resolution in ψ worsens. The tracks seen by the detector are therefore dimmer, meaning fewer good tubes, reducing our ability to reconstruct them. In order for the Extension to work at low energies it must not only be able to see showers down to $10^{16.5}\text{eV}$ but also correctly determine the geometry giving a good resolution in energy and X_{max} . This is important for

identifying features in the spectrum and the composition using the elongation rate.

The monocular analysis of geometry is based on timing. So to improve the resolution the system could be improved by making the FADC faster. The HiRes-2 FADC electronics ran on a 100ns integration time and the signal was shaped by a 35ns four-pole filter. Our initial idea was to simply make the integration time 25ns. Before building any electronics this must be simulated.

A version of the HiRes-II Monte Carlo created by Sean Stratton was developed to simulate some parts of the TALE detector and Tower prototype. It was used to investigate the effect of increasing the mirror size to 3 times that of HiRes mirrors and adding 3 extra rings reaching an elevation of 70° . Using this program an set of mono-energetic cosmic rays showers were thrown. 5000 events were generated at half decade energies from $10^{16.0}\text{eV}$ to $10^{18.0}\text{eV}$. The standard inputs to the Monte Carlo were used. This includes HiRes Stereo/MIA composition, the HiRes cosmic ray flux and the measured U.S. desert atmosphere. The geometric parameters were allowed to vary randomly as in the standard Monte Carlo and showers were thrown from 0 to 10km. The output was of the number of photons and arrival times in 5ns bins.

A new set of programs were developed to processes this output. Initially reading in the raw photon information for each tube, the signal is then shaped by a four-pole filter and a trace is created for each tube. In the i^{th} time bin of the FADC trace can be calculated from the following summation.

$$S_i = \sum_{j=0}^i \frac{N_{pe}^j dt_j^3 e^{-dt_j/\tau}}{3!\tau^4} \quad (8.1)$$

Where S_i is the signal in the i^{th} bin, dt is the time difference between the i^{th} and j^{th} bin, N_{pe}^j is the number of photons in the j^{th} bin and τ is the electronics time constant.

Tubes with a significant greater than 3σ above background are found using a triangle filter which also finds the time of the signal. From the timing information and the positions of the tubes along the track the geometry of the event can be fit, using the method described in section

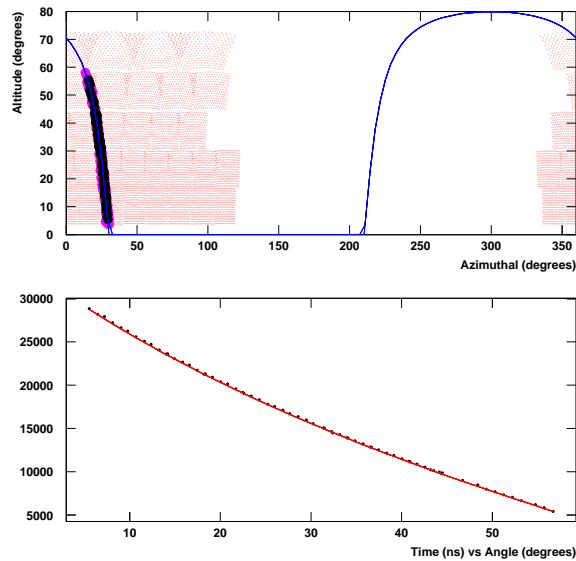


Figure 8.6: Event display for one event using 25ns FADC integration time. See text for details.

4. Subroutines from the new TA analysis software developed by Lauren Scott were used in some of the proceeding steps. Figure 8.6 shows an example of an event. The top panel shows the tubes in altitude and azimuth. Red dots represent all mirror tubes, pink tubes that were hit by light in the Monte Carlo and black the tubes were found by the reconstruction program. The blue line is the shower-detector-plane fit. The gap in tubes is due the to tower design and orientation. In the lower panel we see the time vs angle plot. Black points are the good tubes found by the program and the red line a fit using equation 4.1.

Once the geometry has been reconstructed it can be compared to the thrown values. Figure 8.7 shows the ψ and R_p resolution distributions for 100 and 25ns for the $10^{17.5}$ energy bin. The information as a function of energy is summarized in figure 8.8. The resolution in ψ and R_p are much improved below $10^{17.5}$ eV. However the number of reconstructed events above $10^{17.5}$ eV is reduced. This was due to my initial guess for the time constant τ in the four pole filter. As the HiRes-II τ is almost a third of the integration time I set the 25ns τ to be 9ns. According to Nyquist's theorem [65] the best theoretical shaping time for your signal is twice the sampling rate. Re-running the data using a τ of 50ns we were able to reconstruct with a similar aperture

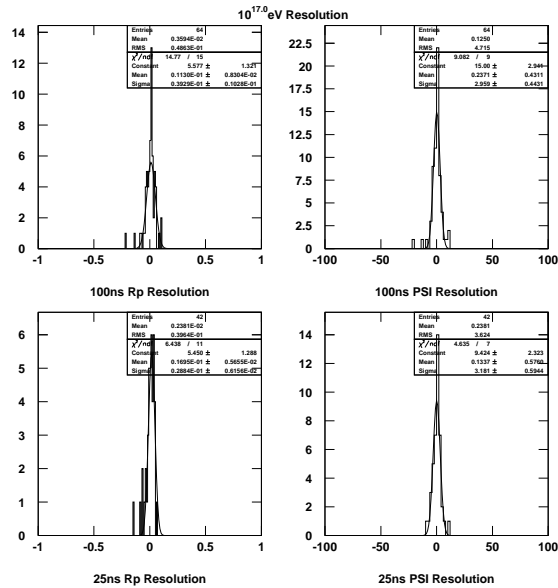


Figure 8.7: ψ and R_P resolution for 100ns and 25ns FADC times.

to that as the original electronics. This information can also be seen in figure 8.8. The difference comes from the number of tubes that are above 3σ . As τ increases the FADC trace is spread out and the noise reduced. Figure 8.9 shows the same FADC trace for different values of τ . Each bin contains more information from the last and therefore the signal above background goes up. We can also see from figure 8.8 that there is little change in in the ψ or R_p resolution. It was decided that the faster electronic system, 25ns with a 50ns τ , should be implemented in the TALE electronics.

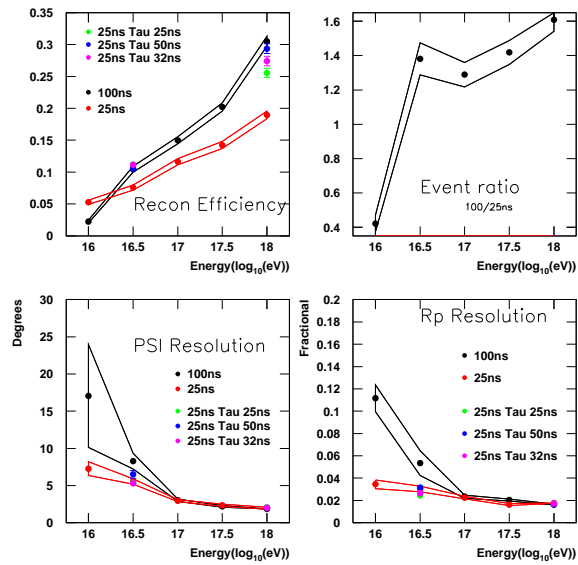


Figure 8.8: Upper panels: Acceptance of events and ratio of 100ns acceptance to 25ns. Lower panels: Resolution of ψ and R_P as a function of energy. Red corresponds to 25ns. Black to 100ns.

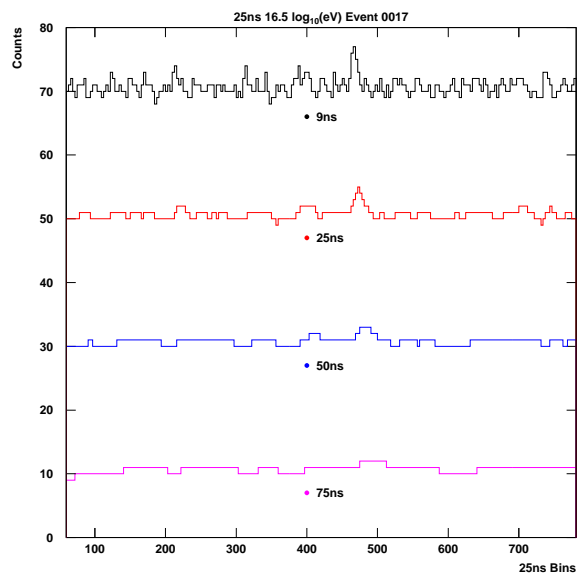


Figure 8.9: A single FADC trace for various τ s.

Chapter 9

Conclusion

9.1 Average Profile

Using the HiRes-II FADC detector the average cosmic ray air shower longitudinal profile was measured. A method was developed to take individual shower profiles, that vary greatly, and average them. The same method was used on the Monte Carlo showers which were generated using the Gaisser-Hillas parametrization. The average showers were found to agree well with the simulated sets from $10^{17.5}\text{eV}$ to $10^{20.0}\text{eV}$. Using a Gaussian in age the average shower widths were parametrized as a function of energy. The data was found to agree well with the a Monte Carlo composed of a mixed but overall light composition.

The Gaisser-Hillas has been the predicted longitudinal shape for 30 years. It simply describes the shower in four physically identifiable terms (N_{max} , X_{max} , X_0 and λ). It is also describes well the output from airshower simulations such as CORSIKA and is widely used in all areas of cosmic ray physics. In the HiRes analysis we integrate across the whole shower to find the primary energy. As we do not see the whole shower we assume it has a Gaisser-Hillas shape. Therefore this is an important results not just for HiRes but for the entire community. It is the first time showers at this energy have have been checked to agree with the predication.

9.2 Telescope Array and the Low Energy Extension

A new cosmic ray detector has been built in Millard County, Utah. Using both FD and SD techniques it aims to identify the source of UHECRs by measuring the flux and composition across many orders of magnitude in energy. A Low Energy Extension will be added to study the

entire extra-galactic component and the end of the galactic spectrum. By combining a variety of techniques systematics will be controlled at an unprecedented level. An explanation for the Second Knee should be found.

In order to accurately measure the geometry and therefore the energy of showers I have simulated a faster electronics system. Proving that by making the FADC integration $4\times$ faster we improve the resolution of geometrical parameters below $10^{17.0}\text{eV}$. However it was also found that to keep the same number of events after reconstruction the time constant, τ , needs to be increased to 50ns.

9.3 HiRes, G.Z.K. Cutoff and Systematics

Forty years after the prediction by Griesen, Katsepin and Kuzmin, HiRes has observed the GZK cutoff with a 5.3σ significance. The aperture is shown to be well understood by Data Monte Carlo comparisons. The position of the break in the spectrum is at the predicted energy, 56EeV. From this we conclude the highest energy cosmic rays are mainly protons traveling a distance of more than 50Mpc, interacting with the CMB to produce pions. Another break was found in the spectrum. The presence of the Ankle at 4.5EeV, a result of pair-production, supports this conclusion.

By implementing new measurements and techniques in the HiRes reconstruction and Monte Carlo it was shown that the HiRes-II energy scale will change by $\sim 12\%$.

Bibliography

- [1] K.-H. Kampert. Ultra high-energy cosmic ray observations. *Journal of Physics Conference Series*, 120(6):062002–+, July 2008.
- [2] J. W. Cronin, T. K. Gaisser, and S. P. Swordy. Cosmic rays at the energy frontier. *Scientific American*, 276:32–37, January 1997.
- [3] D. R. Bergman and The High Resolution Fly’s Eye Collaboration. Observation of the GZK Cutoff Using the HiRes Detector. *Nuclear Physics B Proceedings Supplements*, 165:19–26, March 2007.
- [4] D. R. Bergman and J. W. Belz. TOPICAL REVIEW: Cosmic rays: the Second Knee and beyond. *Journal of Physics G Nuclear Physics*, 34:359–+, October 2007.
- [5] H. Ulrich, W. D. Apel, J. C. Arteaga, A. F. Badea, K. Bekk, A. Bercuci, M. Bertaina, J. Blümer, H. Bozdog, I. M. Brancus, M. Brüggemann, P. Buchholz, A. Chiavassa, F. Cossavella, K. Daumiller, V. de Souza, F. di Pierro, P. Doll, R. Engel, J. Engler, M. Finger, D. Fuhrmann, P. Ghia, H. J. Gils, R. Glasstetter, C. Grupen, A. Haungs, D. Heck, J. R. Hörandel, T. Huege, K.-H. Kampert, D. Kachelbick, H. O. Klages, Y. Kolotaev, P. Luczak, H. J. Mathes, H. J. Mayer, C. Meurer, J. Milke, B. Mitrica, C. Morello, G. Navarra, S. Nehls, J. Oehlschläger, S. Ostapchenko, S. Over, M. Petcu, T. Pierog, S. Plewnia, H. Rebel, A. Risse, M. Roth, H. Schieler, O. Sima, M. Stümpert, G. Toma, G. C. Trinchero, J. van Buren, W. Walkowiak, A. Weindl, J. Wochele, and J. Zabierowski. The knee of cosmic rays - news from KASCADE. In M. Tripathi and R. E. Breedon, editors, *Collicers to Cosmic Rays*, volume 928 of *American Institute of Physics Conference Series*, pages 31–38, August 2007.
- [6] P. Sokolsky and G. B. Thomson. TOPICAL REVIEW: Highest energy cosmic-rays and results from the HiRes experiment. *Journal of Physics G Nuclear Physics*, 34:401–+, November 2007.
- [7] A. N. Bunner. *Cosmic Ray Detection by Atmospheric Fluorescence*. PhD thesis, CORNELL UNIVERSITY., 1967.
- [8] M. Nagano and A. A. Watson. Observations and implications of the ultrahigh-energy cosmic rays. *Reviews of Modern Physics*, 72:689–732, July 2000.
- [9] V. F. Hess. ber Beobachtungen der durchdringenden Strahlung bei siebenFreiballonfahrten. *Physikalische Zeitschrift*, 13:1084–1091, November 1912.
- [10] Pierre Auger, P. Ehrenfest, R. Maze, J. Daudin, and Robley A. Fréon. Extensive cosmic-ray showers. *Rev. Mod. Phys.*, 11(3-4):288–291, Jul 1939.
- [11] W. D. Apel, J. C. Arteaga, A. F. Badea, K. Bekk, J. Blümer, H. Bozdog, I. M. Brancus, M. Brüggemann, P. Buchholz, F. Cossavella, K. Daumiller, V. de Souza, P. Doll, R. Engel, J. Engler, M. Finger, D. Fuhrmann, H. J. Gils, R. Glasstetter, C. Grupen, A. Haungs, D. Heck, J. R. Hörandel, T. Huege, P. G. Isar, K.-H. Kampert, D. Kang, D. Kachelbick, H. O. Klages, Y. Kolotaev, P. Luczak, H. J. Mathes, H. J. Mayer, J. Milke, B. Mitrica, S. Nehls, J. Oehlschläger, S. Ostapchenko, S. Over, M. Petcu, T. Pierog, H. Rebel, M. Roth, G. Schatz, H. Schieler, F. Schröder, O. Sima, M. Stümpert, G. Toma, H. Ulrich, J. van Buren, W. Walkowiak, A. Weindl, J. Wochele, M. Wommer, and J. Zabierowski. Energy spectra of elemental groups of cosmic rays: Update on the KASCADE unfolding analysis. *Astroparticle Physics*, 31:86–91, March 2009.
- [12] M. A. Lawrence, R. J. O. Reid, and A. A. Watson. The cosmic ray energy spectrum above $4 \times 10^{17} eV$ as measured by the Haverah Park array. *Journal of Physics G Nuclear Physics*, 17:733–757, May 1991.

- [13] S. Yoshida and H. Dai. The extremely high energy cosmic rays. *Journal of Physics G Nuclear Physics*, 24:905–938, May 1998.
- [14] T. Abu-Zayyad, M. Al-Seady, K. Belov, D. J. Bird, J. Boyer, G. Chen, R. W. Clay, H. Y. Dai, B. R. Dawson, Y. Ho, M. A. Huang, C. C. H. Jui, M. J. Kidd, D. B. Kieda, B. C. Knapp, W. Lee, E. C. Loh, E. J. Mannel, J. N. Matthews, T. A. O’Halloran, A. Salman, K. M. Simpson, J. D. Smith, P. Sokolsky, P. Sommers, S. B. Thomas, L. R. Wiencke, C. R. Wilkinson, and N. R. Wild. The prototype high-resolution Fly’s Eye cosmic ray detector. *Nuclear Instruments and Methods in Physics Research A*, 450:253–269, August 2000.
- [15] M. I. Pravdin. Energy spectrum of cosmic rays at E_0 greater than $10^{17}eV$ by the Yakutsk eas array data. In *International Cosmic Ray Conference*, volume 3 of *International Cosmic Ray Conference*, pages 292–+, August 1999.
- [16] M. M. Winn, J. Ulrichs, L. S. Peak, C. B. A. McCusker, and L. Horton. The cosmic-ray energy spectrum above $10^{17}eV$. *Journal of Physics G Nuclear Physics*, 12:653–674, 1986.
- [17] M. Nagano, M. Teshima, N. Hayashida, M. Honda, H. Ohoka, Y. Matsubara, S. Yoshida, H. Y. Dai, and T. Hara. Energy spectrum of primary cosmic rays above $10^{17.0}eV$ determined from extensive air shower experiments at Akeno. *Journal of Physics G Nuclear Physics*, 18:423–442, February 1992.
- [18] H. Ohoka, M. Takeda, N. Hayashida, K. Honda, M. Honda, N. Inoue, K. Kadota, F. Kaki-moto, K. Kamata, S. Kawaguchi, N. Kawasumi, Y. Matsubara, K. Murakami, M. Nagano, M. Teshima, I. Tsushima, Y. Uchihori, S. Yoshida, and H. Yoshii. Further development of data acquisition system of the Akeno giant air shower array. *Nuclear Instruments and Methods in Physics Research A*, 385:268–276, January 1997.
- [19] The Pierre AUGER Collaboration. The Surface Detectors of the Pierre Auger Observatory. *Nuclear Physics B Proceedings Supplements*, 136:393–398, November 2004.
- [20] The Pierre AUGER Collaboration. The Fluorescence Detector of the Pierre Auger Observa-tory and Hybrid Performances. *Nuclear Physics B Proceedings Supplements*, 136:399–406, November 2004.
- [21] ENRICO Fermi. On the origin of the cosmic radiation. *Phys. Rev.*, 75(8):1169–1174, Apr 1949.
- [22] T. K. Gaisser. *Cosmic rays and particle physics*. Cambridge and New York, Cambridge University Press, 1990, 292 p., 1990.
- [23] M. Ostrowski. Mechanisms and sites of ultra high energy cosmic ray origin. *Astroparticle Physics*, 18:229–236, December 2002.
- [24] A. G. Lemaître. Contributions to a British Association Discussion on the Evolution of the Universe. *Nature*, 128:704–706, October 1931.
- [25] P. L. Biermann. The origin of the highest energy cosmic rays. *Journal of Physics G Nuclear Physics*, 23:1–27, January 1997.
- [26] K. Greisen. End to the Cosmic-Ray Spectrum? *Physical Review Letters*, 16:748–750, April 1966.
- [27] G. T. Zatsepin and V. A. Kuz’min. Upper Limit of the Spectrum of Cosmic Rays. *Soviet Journal of Experimental and Theoretical Physics Letters*, 4:78–+, August 1966.
- [28] N. N. Kalmykov, S. S. Ostapchenko, and A. I. Pavlov. Quark-Gluon-String Model and EAS Simulation Problems at Ultra-High Energies. *Nuclear Physics B Proceedings Supplements*, 52:17–28, February 1997.
- [29] J. Engel, T. K. Gaisser, P. Lipari, and T. Stanev. Nucleus-nucleus collisions and interpre-tation of cosmic-ray cascades. *Physical Review D*, 46:5013–5025, December 1992.
- [30] J. Holder, V. A. Acciari, E. Aliu, T. Arlen, M. Beilicke, W. Benbow, S. M. Bradbury, J. H. Buckley, V. Bugaev, Y. Butt, K. L. Byrum, A. Cannon, O. Celik, A. Cesarini, L. Ciupik, Y. C. K. Chow, P. Cogan, P. Colin, W. Cui, M. K. Daniel, T. Ergin, A. D. Falcone, S. J. Fegan, J. P. Finley, G. Finnegan, P. Fortin, L. F. Fortson, A. Furniss, G. H. Gillanders, J. Grube, R. Guenette, G. Gyuk, D. Hanna, E. Hays, D. Horan, C. M.

- Hui, T. B. Humensky, A. Imran, P. Kaaret, N. Karlsson, M. Kertzman, D. B. Kieda, J. Kildea, A. Konopelko, H. Krawczynski, F. Krennrich, M. J. Lang, S. Lebohec, G. Maier, A. McCann, M. McCutcheon, P. Moriarty, R. Mukherjee, T. Nagai, J. Niemiec, R. A. Ong, D. Pandel, J. S. Perkins, M. Pohl, J. Quinn, K. Ragan, L. C. Reyes, P. T. Reynolds, H. J. Rose, M. Schroedter, G. H. Sembroski, A. W. Smith, D. Steele, S. P. Swordy, J. A. Toner, L. Valcarcel, V. V. Vassiliev, R. Wagner, S. P. Wakely, J. E. Ward, T. C. Weekes, A. Weinstein, R. J. White, D. A. Williams, S. A. Wissel, M. Wood, and B. Zitzer. Status of the VERITAS Observatory. In *American Institute of Physics Conference Series*, volume 1085 of *American Institute of Physics Conference Series*, pages 657–660, December 2008.
- [31] B. Giebels and the Hess collaboration. Study of extragalactic sources with H.E.S.S. *Journal of Physics Conference Series*, 60:127–130, March 2007.
- [32] G. B. Thomson and D Ivanov. Search for Intermediate-Scale Anisotropy by the HiRes Experiment. In *Proceedings of the 30th International Cosmic Ray Conference*, volume 4, pages 445–448, 2008.
- [33] The Pierre Auger Collaboration. Correlation of the Highest-Energy Cosmic Rays with Nearby Extragalactic Objects. *Science*, 318:938–, November 2007.
- [34] R. U. Abbasi et al. Search for Correlations between HiRes Stereo Events and Active Galactic Nuclei. *Astropart. Phys.*, 30:175–179, 2008.
- [35] J. H. Boyer, B. C. Knapp, E. J. Mannel, and M. Seman. FADC-based DAQ for HiRes Fly’s Eye. *Nuclear Instruments and Methods in Physics Research A*, 482:457–474, April 2002.
- [36] J. N. Matthews and HIREs Collaboration. The Absolute Calibration of the HiRes Detectors. In *International Cosmic Ray Conference*, volume 2 of *International Cosmic Ray Conference*, pages 911–+, July 2003.
- [37] L. R. Wiencke, T. Abu-Zayyad, M. Al-Seady, K. Belov, D. J. Bird, J. Boyer, G. F. Chen, R. W. Clay, H. Y. Dai, B. R. Dawson, P. Denholm, J. Gloyne, D. He, Y. Ho, M. A. Huang, C. C. H. Jui, M. J. Kidd, D. B. Kieda, B. Knapp, S. Ko, K. Larson, E. C. Loh, E. J. Mannel, J. N. Matthews, J. R. Meyer, A. Salman, K. M. Simpson, J. D. Smith, P. Sokolsky, D. Steenblik, J. K. K. Tang, S. Taylor, S. B. Thomas, and C. R. Wilkinson. Radio-controlled xenon flashers for atmospheric monitoring at the HiRes cosmic ray observatory. *Nuclear Instruments and Methods in Physics Research A*, 428:593–607, June 1999.
- [38] J. H. V. Girard, L. R. Wiencke, G. C. Archbold, J. A. Bellido, K. Belov, J. H. Boyer, A. A. Everett, R. C. Gray, C. C. H. Jui, B. C. Knapp, E. J. Mannel, J. N. Matthews, S. A. Moore, J. R. Mumford, M. D. Roberts, P. Shen, P. V. Sokolsky, R. W. Springer, and S. B. Thomas. A fiber-optic-based calibration system for the High Resolution Fly’s Eye cosmic ray observatory. *Nuclear Instruments and Methods in Physics Research A*, 460:278–288, March 2001.
- [39] G. Archbold, T. Abu-Zayyad, J. Albretsen, K. Belov, Z. Cao, M. Dalton, A. Everett, J. Girard, R. Gray, B. F. Jones, C. C. H. Jui, D. B. Kieda, K. Kim, E. C. Loh, K. Martens, J. N. Matthews, S. A. Moore, A. N. Moosman, P. Morrison, J. R. Mumford, K. Reil, R. Riehle, P. Shen, J. D. Smith, P. V. Sokolsky, R. W. Springer, B. Stokes, S. B. Thomas, L. Wiencke, J. Bellido, R. Clay, B. Dawson, K. Simpson, J. H. Boyer, Y. Ho, B. Knapp, W. Lee, E. J. Mannel, M. Seman, C. Song, S. Westerhoff, Z. Zhang, J. W. Belz, B. Dieterle, D. Loomba, G. Martin, J. A. J. Matthews, M. Roberts, D. Bergman, W. Hanlon, L. Perera, G. B. Thomson, A. Zech, N. Manago, M. Sasaki, M. Sasano, and M. Teshima. Night-to-Night Calibration Checks at the High Resolution Fly’s Eye Cosmic Ray Observatory. *APS Meeting Abstracts*, pages 14008–+, April 2001.
- [40] U.S. standard atmosphere, 1976. Technical report, October 1976.
- [41] R. Abbasi, T. Abu-Zayyad, J. F. Amann, G. C. Archbold, K. Belov, S. Benzvi, J. W. Belz, D. R. Bergman, J. Boyer, C. T. Cannon, Z. Cao, B. M. Connolly, J. Fedorova, C. B. Finley, J. H. V. Girard, R. C. Gray, W. P. Hanlon, C. M. Hoffman, M. H. Holzschneider, G. A. Hughes, P. Hüntemeyer, C. C. H. Jui, K. Kim, M. A. Kirn, B. Knapp, E. C. Loh, K. Martens, N. Manago, E. J. Mannel, J. A. J. Matthews, J. N. Matthews, J. R. Mumford, A. O’Neill, R. Riehle, K. Reil, M. D. Roberts, M. Seman, S. R. Schnetzer, P. Shen, G. Sinnis, J. D. Smith, P. Sokolsky, C. Song, R. W. Springer, B. T. Stokes, S. B. Thomas, G. B. Thomson, D. Tupa, S. Westerhoff, L. R. Wiencke, and A. Zech. Techniques for measuring atmospheric aerosols at the high resolution fly’s eye experiment. *Astroparticle Physics*, 25:74–83, February 2006.

- [42] A. Zech. *A measurement of the ultra-high energy cosmic ray flux with the HiRes FADC detector*. PhD thesis, Rutgers The State University of New Jersey - New Brunswick, United States – New Jersey, 2004.
- [43] G. C. Archbold. *A study of the composition of ultra-high-energy cosmic rays using the High-Resolution Fly's Eye*. PhD thesis, AA(THE UNIVERSITY OF UTAH), 2002.
- [44] D. Heck, J. Knapp, J. N. Capdevielle, G. Schatz, and T. Thouw. *CORSIKA: a Monte Carlo code to simulate extensive air showers*. CORSIKA: a Monte Carlo code to simulate extensive air showers., by Heck, D.; Knapp, J.; Capdevielle, J. N.; Schatz, G.; Thouw, T.. Forschungszentrum Karlsruhe GmbH, Karlsruhe (Germany)., Feb 1998, V + 90 p., TIB Hannover, D-30167 Hannover (Germany)., February 1998.
- [45] M. Nagano, K. Kobayakawa, N. Sakaki, and K. Ando. Photon yields from nitrogen gas and dry air excited by electrons. *Astroparticle Physics*, 20:293–309, December 2003.
- [46] F. Kakimoto, E. C. Loh, M. Nagano, H. Okuno, M. Teshima, and S. Ueno. A measurement of the air fluorescence yield. *Nuclear Instruments and Methods in Physics Research A*, 372:527–533, February 1996.
- [47] M. Ave and for the AIRFLY Collaboration. Temperature and Humidity Dependence of Air Fluorescence Yield measured by AIRFLY. *ArXiv e-prints*, November 2007.
- [48] A. M. Hillas. Angular and energy distributions of charged particles in electron-photon cascades in air. *Journal of Physics G Nuclear Physics*, 8:1461–1473, October 1982.
- [49] K. Kamata and J. Nishimura. The Lateral and the Angular Structure Functions of Electron Showers. *Progress of Theoretical Physics Supplement*, 6:93–155, 1958.
- [50] C. Song, Z. Cao, B. R. Dawson, B. E. Fick, P. Sokolsky, and X. Zhang. Energy estimation of UHE cosmic rays using the atmospheric fluorescence technique. *Astroparticle Physics*, 14:7–13, August 2000.
- [51] G. Cowan. *Statistical data analysis*. Statistical data analysis. Publisher: Oxford: Clarendon Press, 1998 Series: Oxford science publications. ISBN: 0198501560, 1997.
- [52] M. Takeda, N. Sakaki, K. Honda, M. Chikawa, M. Fukushima, N. Hayashida, N. Inoue, K. Kadota, F. Kakimoto, K. Kamata, S. Kawaguchi, S. Kawakami, Y. Kawasaki, N. Kawasumi, A. M. Mahrous, K. Mase, S. Mizobuchi, Y. Morizane, M. Nagano, H. Ohoka, S. Osone, M. Sasaki, M. Sasano, H. M. Shimizu, K. Shinozaki, M. Teshima, R. Torii, I. Tsushima, Y. Uchihori, T. Yamamoto, S. Yoshida, and H. Yoshii. Energy determination in the akeno giant air shower array experiment. *Astroparticle Physics*, 19:447, 2003.
- [53] M. Roth and for the Auger Collaboration. Measurement of the UHECR energy spectrum using data from the Surface Detector of the Pierre Auger Observatory. *ArXiv e-prints*, June 2007.
- [54] J. R. T. de Mello Neto and for the Pierre Auger Collaboration. Status and recent results from the Pierre Auger Observatory. *ArXiv e-prints*, December 2007.
- [55] R. U. Abbasi, T. Abu-Zayyad, M. Allen, J. F. Amman, G. Archbold, K. Belov, J. W. Belz, S. Y. Ben Zvi, D. R. Bergman, S. A. Blake, O. A. Brusova, G. W. Burt, C. Cannon, Z. Cao, B. C. Connolly, W. Deng, Y. Fedorova, C. B. Finley, R. C. Gray, W. F. Hanlon, C. M. Hoffman, M. H. Holzschneider, G. Hughes, P. Hütemeyer, B. F. Jones, C. C. H. Jui, K. Kim, M. A. Kirn, E. C. Loh, M. M. Maestas, N. Manago, L. J. Marek, K. Martens, J. A. J. Matthews, J. N. Matthews, S. A. Moore, A. O'Neill, C. A. Painter, L. Perera, K. Reil, R. Riehle, M. Roberts, D. Rodriguez, N. Sasaki, S. R. Schnetzer, L. M. Scott, G. Sinnis, J. D. Smith, P. Sokolsky, C. Song, R. W. Springer, B. T. Stokes, S. B. Thomas, J. R. Thomas, G. B. Thomson, D. Tupa, S. Westerhoff, L. R. Wiencke, X. Zhang, and A. Zech. First Observation of the Greisen-Zatsepin-Kuzmin Suppression. *Physical Review Letters*, 100(10):101101–+, March 2008.
- [56] Flash Collaboration, R. Abbasi, T. Abu-Zayyad, K. Belov, J. Belz, D. R. Bergman, Z. Cao, F. Y. Chang, C.-C. Chen, C. W. Chen, P. Chen, M. Dalton, Y. Fedorova, C. Field, C. Hast, M. A. Huang, P. Hütemeyer, W.-Y. P. Hwang, R. Iverson, B. F. Jones, C. C. H. Jui, G.-L. Lin, E. C. Loh, N. Manago, K. Martens, J. N. Matthews, M. Maestas, J. S. T. Ng, A. Odian, K. Reil, D. Rodriguez, J. Smith, P. Sokolsky, R. W. Springer, J. Thomas,

- S. Thomas, G. Thomson, D. Walz, A. Zech, and FLASH Collaboration. The FLASH thick-target experiment. *Nuclear Instruments and Methods in Physics Research A*, 597:37–40, November 2008.
- [57] Gordon Thomson, Private Communication.
- [58] F. Nerling, J. Blumer, R. Engel, and M. Risse. Universality of electron distributions in high-energy air showers-Description of Cherenkov light production. *Astroparticle Physics*, 24:421–437, January 2006.
- [59] B. Rossi and K. Greisen. Cosmic-Ray Theory. *Reviews of Modern Physics*, 13:240–309, October 1941.
- [60] T. K. Gaisser and A. M. Hillas. Reliability of the Method of Constant Intensity Cuts for Reconstructing the Average Development of Vertical Showers. In *International Cosmic Ray Conference*, volume 8 of *International Cosmic Ray Conference*, pages 353–+, 1977.
- [61] T. Abu-Zayyad, K. Belov, D. J. Bird, J. Boyer, Z. Cao, M. Catanese, G. F. Chen, R. W. Clay, C. E. Covault, H. Y. Dai, B. R. Dawson, J. W. Elbert, B. E. Fick, L. F. Fortson, J. W. Fowler, K. G. Gibbs, M. A. K. Glasmacher, K. D. Green, Y. Ho, A. Huang, C. C. Jui, M. J. Kidd, D. B. Kieda, B. C. Knapp, S. Ko, C. G. Larsen, W. Lee, E. C. Loh, E. J. Mannel, J. Matthews, J. N. Matthews, B. J. Newport, D. F. Nitz, R. A. Ong, K. M. Simpson, J. D. Smith, D. Sinclair, P. Sokolsky, C. Song, J. K. K. Tang, S. B. Thomas, J. C. van der Velde, L. R. Wiencke, C. R. Wilkinson, S. Yoshida, and X. Z. Zhang. A measurement of the average longitudinal development profile of cosmic ray air showers between 10^{17} and 10^{18} eV. *Astroparticle Physics*, 16:1–11, October 2001.
- [62] C. Song. Longitudinal profile of extensive air showers. *Astroparticle Physics*, 22:151–158, November 2004.
- [63] H. Tokuno, R. U. Abbasi, T. Abu-Zayyad, R. Azuma, J. W. Belz, T. Benno, D. R. Bergman, S. A. Blake, O. Brusova, R. Cady, Z. Cao, B. G. Cheon, J. Chiba, M. Chikawa, I. S. Cho, T. Chung, F. Cohen, K. Doura, T. Doyle, A. Endo, H. Fujii, T. Fukuda, M. Fukushima, Y. Hayashi, K. Hayashi, N. Hayashida, K. Hibino, K. Hiyama, K. Honda, P. Huentemeyer, G. A. Hughes, T. Iguchi, D. Ikeda, K. Ikuta, N. Inoue, T. Ishii, C. C. H. Jui, K. Kadota, F. Kakimoto, T. Kanbe, K. Kasahara, H. Kawai, S. Kawakami, S. Kawana, E. Kido, Y. Kondo, Y. J. Kwon, S. Machida, K. Martens, T. Matsuda, T. Matsuyama, J. A. J. Matthews, J. N. Matthews, M. Minamino, K. Miyata, M. Mostafa, Y. Murano, T. Nakamura, S. Nam, T. Nonaka, S. Ogio, S. Oh, M. Ohnishi, H. Ohoka, A. Ohshima, T. Okuda, J. Ormes, S. Ozawa, I. H. Park, J. H. Park, D. Rodriguez, H. Sagawa, N. Sakurai, L. M. Scott, T. Shibata, N. Shimizu, H. Shimodaira, G. Sinnis, J. D. Smith, P. Sokolsky, R. W. Springer, S. R. Stratton, S. Suzuki, M. Takeda, A. Taketa, M. Takita, Y. Tameda, K. Tanaka, M. Tanaka, H. Tanaka, M. J. Taylor, M. Teshima, J. R. Thomas, S. B. Thomas, G. B. Thomson, T. Tomida, R. Torii, Y. Tsunesada, Y. Uchihori, S. Udo, Y. Unno, Y. Wada, V. B. Wickwar, L. R. Wiencke, T. D. Wilkerson, Y. Yamakawa, H. Yamaoka, J. Yang, S. Yoshida, H. Yoshii, and Y. H. Yun. The Telescope Array experiment: status and prospects. *Journal of Physics Conference Series*, 120(6):062027–+, July 2008.
- [64] Douglas R. Bergman et al. Can experiments studying ultrahigh energy cosmic rays measure the evolution of the sources? 2006.
- [65] Stan Thomas, Private Communication.
- [66] The High Resolution Fly’S Eye Collaboration, R. U. Abbasi, T. Abu-Zayyad, J. F. Amann, G. Archbold, R. Atkins, K. Belov, J. W. Belz, S. Benzvi, D. R. Bergman, J. H. Boyer, C. T. Cannon, Z. Cao, B. M. Connolly, Y. Fedorova, C. B. Finley, W. F. Hanlon, C. M. Hoffman, M. H. Holzscheiter, G. A. Hughes, P. Huentemeyer, C. C. H. Jui, M. A. Kirn, B. C. Knapp, E. C. Loh, N. Manago, E. J. Mannel, K. Martens, J. A. J. Matthews, J. N. Matthews, A. O’Neill, K. Reil, M. D. Roberts, S. R. Schnetzer, M. Seman, G. Sinnis, J. D. Smith, P. Sokolsky, C. Song, R. W. Springer, B. T. Stokes, S. B. Thomas, G. B. Thomson, D. Tupa, S. Westerhoff, L. R. Wiencke, and A. Zech. A measurement of time-averaged aerosol optical depth using air-showers observed in stereo by HiRes. *Astroparticle Physics*, 25:93–97, March 2006.
- [67] S. F. Taylor, T. Abu-Zayyad, K. Belov, Z. Cao, G. Chen, C. C. H. Jui, D. B. Kieda, J. N. Matthews, M. Salamon, P. V. Sokolsky, J. D. Smith, P. Sommers, R. W. Springer, B. T. Stokes, S. B. Thomas, L. R. Wiencke, J. A. J. Matthews, R. W. Clay, B. R. Dawson,

- K. Simpson, J. Bells, J. Boyer, B. Knapp, B. H. Song, X. Z. Zhang, the SDSS Collaboration, High Resolution Fly's Eye Collaboration, and Telescope Array/U. Tokyo Collaboration. Light Transmission From Extended Air Showers Produced By Cosmic-Rays and Gamma-Rays. In *Bulletin of the American Astronomical Society*, volume 31 of *Bulletin of the American Astronomical Society*, pages 842–+, May 1999.
- [68] T. K. Gaisser and A. M. Hillas. *Reliability of the method of constant intensity cuts for reconstructing the average development of vertical showers*. Proceedings of the 15th ICRC, 1977.
- [69] Z. Cao. *A Measurement of the average longitudinal development profile of cosmic ray air showers between $10^{17}eV$ and $10^{18}eV$* . Proceedings of the 27th ICRC, 2001.
- [70] HiRes Collaboration. Studies of systematic uncertainties in the estimation of the monocular aperture of the HiRes experiment. *ArXiv Astrophysics e-prints*, July 2006.

Curriculum Vita

Gareth Hughes

Education

- May 2009 Ph.D. Physics, Rutgers the State University of New Jersey, USA.
- June 2003 MPhys Physics, Manchester University, UK.
- June 1999 Yale College Wrexham, Wales, UK.

Publications

R. Abbasi *et al.* [HiRes Collaboration], “Observation of the GZK cutoff by the HiRes experiment,” *Phys. Rev. Lett.* **100**, 101101 (2008) [arXiv:astro-ph/0703099].

G. Hughes *et al.* [HiRes Collaboration], “Average Longitudinal Cosmic Ray Shower Profile” *In Progress*

R. Abbasi *et al.* [HiRes Collaboration], “HiRes Stereoscopic Measurement of the UHECR Flux” *Submitted*

R. Abbasi *et al.* [HiRes Collaboration], “Studies of systematic uncertainties in the estimation of the monocular Astropart. Phys. **27**, 370 (2007) [arXiv:astro-ph/0607094]. R. Abbasi *et al.* [HiRes Collaboration], “A Likelihood Method for Measuring the Ultrahigh Energy Cosmic Ray Composition,” *Astropart. Phys.* **26**, 28 (2006) [arXiv:astro-ph/0604558].

R. Abbasi *et al.* [High Resolution Fly’s Eye Collaboration], “A Measurement of Time-Averaged Aerosol Optical Depth using Air-Showers Observed in Stereo by HiRes,” *Astropart. Phys.* **25**, 93 (2006) [arXiv:astro-ph/0601091].

R. Abbasi *et al.* [HiRes Collaboration], “Techniques for measuring atmospheric aerosols at the High Resolution Fly’s Eye experiment,” *Astropart. Phys.* **25**, 74 (2006) [arXiv:astro-ph/0512423].

R. U. Abbasi *et al.* [HiRes Collaboration], “Search for Point-Like Sources of Cosmic Rays with Energies above $10^{18.5}$ eV in the HiRes-I Monocular Data-Set,” *Astropart. Phys.* **27**, 512 (2007) [arXiv:astro-ph/0507663].

R. U. Abbasi *et al.* [HiRes Collaboration], “Search for Cross-Correlations of Ultra-High-Energy Cosmic Rays with BL Lacertae Objects,” *Astrophys. J.* **636**, 680 (2006) [arXiv:astro-ph/0507120].

R. U. Abbasi *et al.* [The High Resolution Fly’s Eye Collaboration], “Observation of the Ankle and Evidence for a High-Energy Break in the Cosmic Ray Spectrum,” *Phys. Lett. B* **619**, 271 (2005) [arXiv:astro-ph/0501317].

R. U. Abbasi *et al.* [The High Resolution Fly’s Eye Collaboration], “Search for Point Sources of Ultra-High Energy Cosmic Rays Above 40 EeV Using a Maximum Likelihood Ratio Test,” *Astrophys. J.* **623**, 164 (2005) [arXiv:astro-ph/0412617].

R. U. Abbasi *et al.* [The High Resolution Fly’s Eye Collaboration], “A Study of the Composition of Ultra High Energy Cosmic Rays Using the High Resolution Fly’s Eye,” *Astrophys. J.* **622**, 910 (2005) [arXiv:astro-ph/0407622].

R. U. Abbasi *et al.* [The High Resolution Fly’s Eye Collaboration(HiRes)], “A Search for Arrival Direction Clustering in the HiRes-I Monocular Data above $10^{19.5}$ eV,” *Astropart. Phys.* **22**, 139 (2004) [arXiv:astro-ph/0404366].

R. U. Abbasi et al. [The High Resolution Fly's Eye Collaboration(HIRES)], "Study of Small-Scale Anisotropy of Ultrahigh Energy Cosmic Rays Observed in Stereo by HiRes," *Astrophys. J.* **610**, L73 (2004) [arXiv:astro-ph/0404137].

H. Kawai et al., "Telescope array experiment," *Nucl. Phys. Proc. Suppl.* **175-176**, 221 (2008).

R. U. Abbasi et al., "Search for Correlations between HiRes Stereo Events and Active Galactic Nuclei," *Astropart. Phys.* **30**, 175 (2008) [arXiv:0804.0382 [astro-ph]].

R. U. Abbasi et al., "An upper limit on the electron-neutrino flux from the HiRes detector," arXiv:0803.0554 [astro-ph].

D. R. Bergman et al., "Can experiments studying ultrahigh energy cosmic rays measure the evolution of the sources?," arXiv:astro-ph/0603797.

H. Tokuno et al., "The Telescope Array experiment: Status and prospects," *J. Phys. Conf. Ser.* **120**, 062027 (2008).